Incoherent effects in hot-electron quantum optics

Clarissa Jade Barratt

Thesis submitted for the degree of
Doctor of Philosophy

School of Mathematics, Statistics & Physics
Newcastle University
Newcastle upon Tyne
United Kingdom

December, 2021

Abstract

Dynamic quantum dots as sources of single electrons open up new avenues to explore fundamental issues of solid-state physics. These types of single electron source allow for injection of electrons at energies high above the Fermi level. These high energies increase the spatial separation between bulk and injected electrons, reducing electron-electron interactions which are the dominant source of decoherence for cold electrons. Unfortunately, although these high energies reduce one source of decoherence, they introduce the potential for others to become dominant.

In this thesis, we investigate two of these sources of decoherence on electrons which reduce their ability to act quantum mechanically, and explore the conditions required to mitigate these effects. First we investigate the effect of phase averaging, which is caused by the uncertainty in the injection energy of an electron. We calculate the phase contributions from beamsplitters, path lengths and the Aharonov-Bohm phase, as well as the energy dependence of the transmission and reflection coefficients of the beamsplitters. We find that optimum conditions such that visibility can be maximised are obtained not at zero path length difference as in optics, but with an offset in the length of the interferometer arms. At the higher energies in hot-electron quantum optics, longitudinal-optical (LO)-phonon emission becomes the dominant source of decoherence. In this thesis we derive a complete quantum master equation to describe the rate of emission of LO-phonons and the behaviour of electrons undergoing this emission.

The findings in this thesis are vital to the successful implementation of quantum optics-like experiments with hot electrons. These results can be used as input into both experimental architectures and dynamical simulations, and combined with previous results provide a complete quantum picture of the incoherent effects in hot electron quantum-optics.

Acknowledgements

I would first like to say a huge thank you to my supervisor, Clive Emary, for his support and guidance over the last four years and for forgiving me for spilling coffee all over his desk. I am also very thankful to the group's collaborators, Masaya Kataoka, Sungguen Ryu and Heung-Sun Sim.

A huge thank you also to the other members of the HEQO journal club, Lewis Clark and Keaghan Krog, for both their academic insights and fun tangents, in particular thank you to Lewis for proof reading this entire thesis; I am sure you will be glad to never have another Zoom meeting with me again.

Thank you to all of the support staff in the department, in particular to Michael Beaty, Helen Green, John Nicholson, and George Stagg.

In the department, I would like to thank all those I have shared an office with: Sultan Alyobi, Jordan Barnes, Francesca Caloro, Rob Cooper, Michael Ellis, Jinzhao Liu, Keith Newman, Em Rickinson and Matina Trachana. Honorable mentions from the world outside PhD 1 include: members of the department, Kate Brown, David Cushing, Liam Dobson, Ryan Doran, Francesca Fedele, Stuart Hall, Sophie Harbisher, Tom Lowe, Stephen Mason, Mae Mezgarneshad, Holly Middleton-Spencer, Sam Mutter, Christiana Radu, Joe Reid, David Robertson, Matt Robinson, David Stewart, Devika Tharakkal, Laura Wadkin, Dave Walshaw, Jack Walton and Ashley Wilkins; climbing buddies, Andrew Groszek, Rathish Ratnasingham, and Nick Waterton; for their badminton prowess, Robbie Bickerton and Joe Matthews; and for being unforgettable housemates Alex Jusupov and Anna Mitchell. My thanks also go out to to the NCL and NSU Irish Dance societies for keeping me exercised and entertained throughout my PhD.

Of course, I cannot forget those people outside the university who have been beside me all of the way. Thank you to Physics Team, without whom my undergrad years would have been a lot less entertaining and memorable. To those friends I have had for forever, and those who feel like it has been, Sophie Burton, Sarah Jowett, Tim McNulty, Hayley Moore and Rachel Pitt, thank you for being with me through thick and thin, and most importantly for giving me a safe space to rant and rave when the maths made me angry. I'd also like to say thank you to the Blands, who have made me so welcome in their family and cheered me on all the way.

I will forever be grateful to my wonderful family for their love and support throughout my seemingly never ending studies, especially my mum, Joanne, and my sister, Tammy, and with special thanks to my biggest cheerleader, my grandad, DJ, who first sparked my love of numbers with sums at the coffee table and who will be possibly even more excited than I will when I hand this in.

Finally, to Tom Bland, thank you for providing me with love, support, biscuits and the next big adventure.

Abbreviations and constants

Abbreviation	Definition
2DEG	Two-dimensional electron gas
AB	Aharonov-Bohm
ATD	Arrival time distribution
BS	Beamsplitter
LO	Longitudinal optical
MZI	Mach-Zehnder interferometer
QPC	Quantum point contact
SES	Single electron source

Symbol	Constant name	Value
$\|e\|$	Electron charge	$1.60217657 \times 10^{-19}\,\mathrm{C}$
h	Planck's constant	$6.62607015 \times 10^{-34}\,\mathrm{J.s}$
$\hbar$	Reduced Planck's constant	$1.054571726 \times 10^{-34}\,\mathrm{J.s}$
$\hbar\omega_y$	Confinement	$2.7\,\mathrm{meV}$
$\hbar\omega_{\mathrm{LO}}$	Energy of an LO-phonon	$\approx 36\,\mathrm{meV}$
m_e^*	Effective electron mass (GaAs)	$0.067 \times 9.10938291 \times 10^{-31}\,\mathrm{kg}$
X	Assumed horizontal length of MZI	$5\,\mu\mathrm{m}$
σ_E	Initial wavepacket spread in energy	$1\,\mathrm{meV}$

Dissemination of results

The results in this thesis have been partially covered in the following:

- **CJ Barratt**, S Ryu, LA Clark, H-S Sim, M Kataoka, C Emary, *Asymmetric arms maximise visibility in hot-electron interferometers*, Phys. Rev. B **104** 035436 (2021)
- Presentations: *Incoherent effects in hot-electron quantum optics*
  APS March Meeting 2020 (Cancelled due to COVID - materials online)
  Northern Quantum Meetings, 2018 and 2020
- Posters: *Incoherent effects in hot-electron quantum optics*
  Okinawa School in Physics 2018: Coherent Quantum Dynamics
  Bad Honnef Physics School on Quantum Technologies, 2018

Contents

Part I

Introduction

Chapter 1

Introduction

Leucippus and Democritus postulated the existence of atoms as far back as the 5th century BC [1]. The world today is all but unrecognisable from the one in which they lived; however, one thing that hasn't changed is the curiosity of the human race. Since ruminating on the topic of atoms with the ancient Greeks, our understanding of the universe has only grown, and with it, the potential to delve deeper into the unknown. Now, more than two millennia later, it is our turn to investigate the utility of the quantum realm.

Since Michael Faraday's invention of the electric motor in 1832 [2], almost all technology has moved to being electronics-based, from trains, to lighting, to communications. As a species, we are now very good at fabricating devices that use electricity to make our lives easier. The better we get at making new electronic devices, the more demand there is for increasing power and storage, which is achieved by making the components of the devices, such as transistors, smaller and smaller. In 1965, Gordon E. Moore observed that the number of transistors in circuits was doubling every year, and projected that this would continue in the future [3]. Unfortunately, if we want to keep making more powerful devices, with more transistors, we either need to start making the devices much bigger or the electrical components much smaller. At some point, we get to components so small that we have to start considering quantum effects.

With the recent advent of single-electron sources (SESs) [4], the creation of components on this scale is a possibility. Not only does this provide a method of creating smaller electronics, but the wave-like properties of electrons could also be exploited to bring us into the realms of quantum technology [5]. Single-electron sources are also a possibility for quantum metrology, and have been used in redefining the Ampere as the number of electrons passing a point per second [6, 7].

Electronic components with length scales on the order of the coherence lengths of electrons bring their own challenges along with the ability to create quantum technologies, as quantum effects, both wanted and unwanted, now become important. This has led to the demand for better understanding of single-electron transport, and therefore the creation of better SESs and further investigations into their behaviour.

The purpose of this thesis is to describe some of the incoherent effects of single-electrons in a high-energy regime, and to investigate the optimal build parameters and experimental conditions to mitigate these effects. It will also give a more complete quantum picture of electrons undergoing relaxation in an open quantum system.

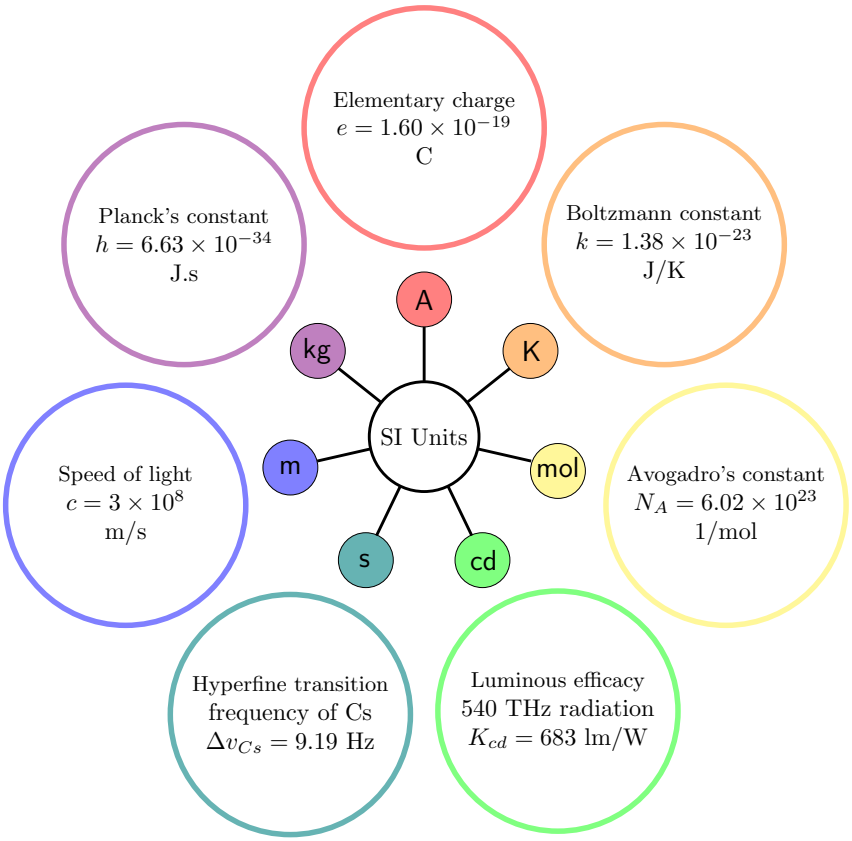

Figure 1.1: The relationship between all of the SI units and the fundamental constants.

In this chapter, I will introduce the general background concepts describing the systems that we will consider in this thesis. I will then present an overview of the structure for the rest of the work.

1.1 Single-electron sources

Single-photon sources were a revolution in the world of quantum optics [8, 9]; allowing coherent packets of light to travel independently of each other became central to techniques in quantum key distribution [10] which is central to security in quantum computing, for example. Following the success of single-photon sources, investigations began into the creation of SESs, resulting today in a wide selection of SESs to choose from [4, 11].]

Single-electron sources are of considerable interest to the physics community, due to their use in metrological applications, such as the redefinition of the SI unit system [6, 12, 7], as well as their use as tunable circuit elements [13].

Until 2019, the definition of the Ampere was the current which would produce a force equal to 2×10^{-7} N between two infinitely long, straight parallel conductors with negligible circular cross-section placed 1m apart in a vacuum, per metre of length [7]. This has since been redefined using the charge of a single electron, $e = 1.60217662 \times 10^{-19}$ C. The output current of SESs can be measured as $I = ef$, that is, the current, I, is the product of the electron charge, e and the frequency with which the electrons are released, f [14]. Defining the current based on these devices means that the current is based solely on the charge of the electron and the definition

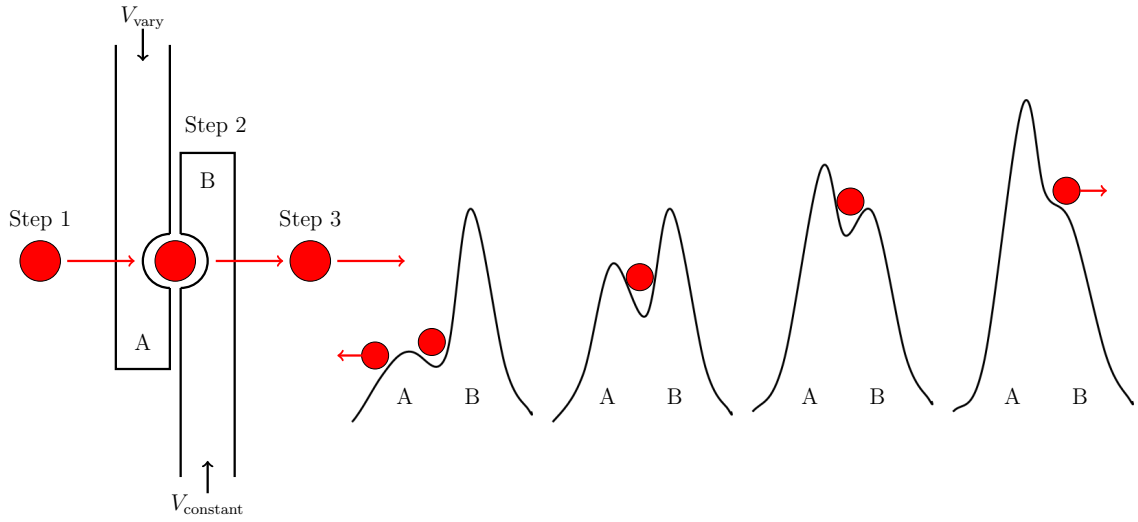

Figure 1.2: A sketch of the gates for a quantum-dot-based single-electron source. Gate B is kept at a constant voltage that will determine the injection energy of the electron, and the voltage of gate A is varied up and down, pushing an electron from the source (step one), into the dot (step two) and then out into the system (step three). Also shown is a demonstration of how the voltage gate A varies to "push" an electron out into the system.

of the second, which are themselves fundamental constants. The new definition of the Ampere is also measurable in a lab, whereas due to the unavailability of infinitely long wires, the old definition was not able to be created in reality. For this to be successful the accuracy of the SESs must be sufficiently high, such that the new definition is indeed better than the original. A sketch showing the links between the SI units and fundamental constants can be seen in Fig. 1.1.

Multiple methods of single-electron injection have been devised over the years, from the first experimental realisation of a metallic-turnstile-type SES in 1990 [15], to quantum-dot-based sources [16, 17], with many in between [18, 19]. A review of SESs can be found in Ref. [19]. In this thesis, we consider a gate-modulated, or dynamic quantum-dot SES [19–21]. Here I will give a brief overview of this type of SES, although for the rest of the thesis we will not be looking at the function of the SES itself, but on the dynamics of the injected electron.

Consider an SES created in a 2-dimensional electron gas (2DEG), which is a 2D layer of electrons between two semiconductors (these will be introduced in more detail in chapter 2). When a negative voltage is applied to metallic gates on the surface of the 2DEG, the electrons beneath are repelled, creating a potential barrier. They can be structured such that a quantum-dot appears between the two gates, as in Fig. 1.2. If the voltage on gate two is kept high, and the voltage on gate one is lowered, an electron can fall into the quantum dot. The voltage on gate one can then be raised until it is above that of gate two, which will push the electron over into the system. This can be done rapidly, at almost a billion electrons per second, and reliably at a given energy, with an accuracy better than 1.2ppm [6].

As the voltage on the gate determines the energy of the injected electrons, it can be set to any (experimentally reasonable) value, and as such the electrons can be injected at energies far above the Fermi energy. This higher energy of injection is useful, as the difference in energy translates to a spatial difference between injected electrons and those in the 2DEG; for example, an injection energy of 100 meV gives

a spatial distance from the bulk electrons in the Fermi sea of 100 nm. Electron-electron interactions are quite strong, but also very short range, so when there is a large spatial separation they are significantly suppressed, to the point that they can be ignored for the purposes of this investigation [22].

While electron-electron interactions are insignificant at these higher energies, other decay channels become relevant. Most notably, phonons become a significant source of relaxation and decoherence [23–25]. I will later consider in more detail the effect of one of these phonon processes, namely longitudinal optical (LO)-phonons, in part III. There is also an uncertainty in the energies, as every electron is not injected at exactly the same energy due to the non-instantaneous nature of the gate voltage change, which allows time for tunnelling to occur. This results in phase averaging, and is discussed further in part II. The spatial separation of these injected electrons from the bulk means that they are isolated and their movement can be controlled by building paths into the system which are comparable to optical paths.

1.2 Quantum optics

Quantum optics is the study of the interactions of matter with photons of light, which has many applications from quantum cryptography [26, 27] to quantum metrology [28] and also gives us the ability to further understand the fundamentals of quantum mechanics.

One of the main experimental techniques in quantum optics is that of interferometry, which is the technique of superimposing electromagnetic waves to observe and extract information, such as the strength of the magnetic field, from the interference patterns. There are many different types of interferometer, all of which have slightly different setups and uses, but the basic principle is the same for all. A source of electromagnetic radiation emits light which is manipulated using an array of mirrors and beamsplitters, causing it to follow a predetermined path. The light is then detected and any interference caused by differences in the paths can be observed.

The first interferometer was created for the Michelson-Morley experiment in 1887. This interferometer, now known as the Michelson interferometer, consisted of two arms and a beamsplitter that splits a beam of light and sends it down both arms, where they are reflected back, recombined at the beamsplitter and directed towards a detector, as shown in Fig. 1.3. The Michelson-Morley experiment was designed to look for evidence of the luminiferous aether, which was thought to be the material that filled the seemingly empty space through which light could travel [29].

The results of this experiment were of course negative, as we now know that light does not need a medium through which to travel and that the majority of space is in fact a vacuum; however, the technique used to make these measurements has been used ever since. In more modern times for example, we now have the Laser Interferometer Gravitational-Wave Observatory, (LIGO), a 4km-long Michelson interferometer used to detect gravitational waves [30].

Since the introduction of interferometry, several new types of interferometer have been designed, all of which are optimised for different uses. We will be concentrating specifically on the Mach-Zehnder Interferometer (MZI). A MZI is a device used to measure the phase shift between two beams of light that have been split from one (or

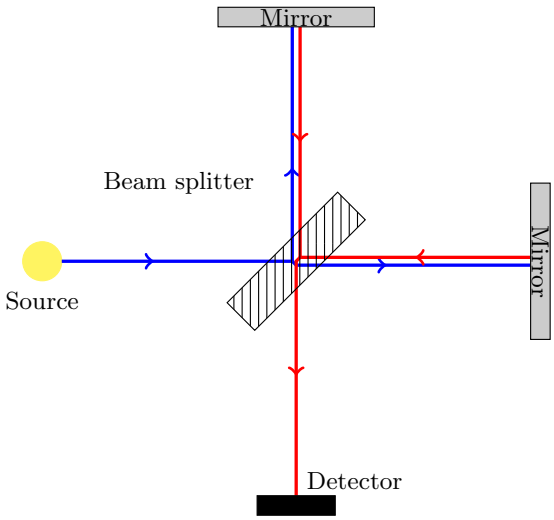

Figure 1.3: A simple diagram of a Michelson interferometer where the blue paths are the input, and the red is the return journey.

two) original emitted beam(s), which means the each beam is initially coherent. The beams of light are split and travel around the interferometer, rejoining at another beamsplitter, with the intensity then being measured in two detectors, as shown in Fig. 1.4. By placing some sort of "obstacle" (for example, something of which the properties are to be measured) in the paths, or changing the path lengths, a phase shift can be introduced between the arms, which can be measured by looking at the intensity at the detectors.

MZIs are useful for a wide range of applications, from measuring the density of supersonic air streams [31] to understanding processes in quantum cryptography [32], but their uses are no longer restricted solely to the interference of light.

1.3 Electron quantum optics

Today we are able to exploit the wave nature of electrons and apply the techniques used for quantum optics to systems of electrons as well. Obviously, the systems used to investigate the behaviour of photons would be inappropriate for investigating electrons and so to do similar experiments they have had to be redesigned. In 2003, Ji *et al.* created an electronic analogue of the MZI [33]. Systems such as the one developed by Ji *et al.* are useful because they function well at the high magnetic fields required for the quantum Hall effect, which allows for the single-electrons to be isolated from the bulk. In other types of interferometers, the high magnetic fields interfere with the symmetry of the experiment. For example, the double slit experiment is of no use in the detection of electrons under a high magnetic field as the electrons follow the edges and therefore approach the slits from the side. Consequently, they go through only the closest slit instead of both, which breaks the symmetry of the experiment and renders it useless.

The previous section explained the case for an optical MZI; however, the same principles can be seen in an electrical analogue of the MZI [33] where an electronic reservoir is at a specific voltage and the rest of the reservoirs are grounded, allowing an electron to travel around following quantum Hall edge states (see chapter 2). In

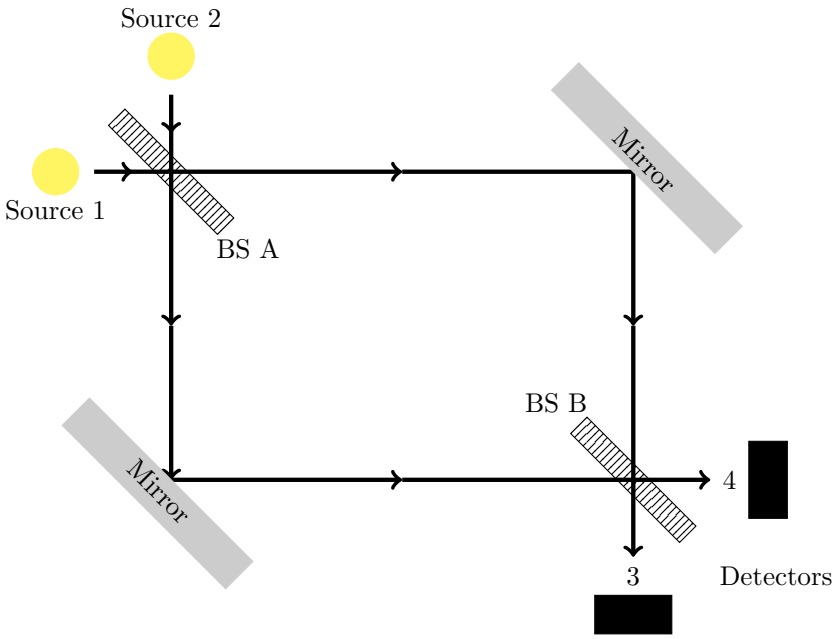

Figure 1.4: A simple diagram of a MZI. A beam of light is emitted from source 1, 2 or both, and split into two at the beamsplitter. The two beams pick up phases depending on the path they travel down, and are then rejoined at the second beamsplitter before being directed towards a detector. Light intensity is measured at detectors 3 and 4, where any phase difference between the two paths can be seen in the interference pattern.

this version, an extra phase must be taken into account due to the Aharonov-Bohm (AB) flux [34], a phase shift introduced due to the magnetic field passing through the device. This is described in more detail in section 2.5.

The MZI can actually make use of the chirality of the system, as there are two distinct paths down which the electron must travel, so a second edge can be placed in the middle of the system along which the electrons can travel, without interfering with the overall functionality of the system.

Just as an optical MZI measures the amplitude of the light wave at the detector, the electrical analogue measures the amplitude of the wavepacket; however, there are many interactions and losses that can occur throughout the system, which can affect the visibility of the wavepackets. Visibility is determined by the ratio of the amplitude of the initial signal and the amplitude of the detected signal, given by

$$\nu = \frac{I_{\max} - I_{\min}}{I_{\max} + I_{\min}}, \tag{1.1}$$

where $I_{\min/\max}$ are the minimum and maximum amplitude of the detected current. The ratio of these amplitude differences gives the visibility of the system. The visibility is maximised when difference between the maximum and minimum current is maximised. The amplitude can be reduced when the wavepacket does not arrive at the second beamsplitter at the same time from both arms, meaning there will be some deconstructive interference, which reduces the visibility. Visibility can also be reduced due to the spreading of the wavepackets, known as by phase averaging.

Of course, there must be analogues to all of the components of the MZI, as an electron will not be reflected off a mirror (or follow a waveguide or fibre optic), or interact with a normal beamsplitter in the same way light does. In the case

of an electronic MZI, mirrors are unnecessary as the electrons will follow the edge channels of the system in whatever direction they go, as mentioned above. However, analogues of the beamsplitters are less trivial. In the setups that we consider the beamsplitters now take the form of quantum point contacts (QPCs). These are metallic gates placed on the 2DEG, similar to that used for the single-electron source. A voltage is applied to the QPC that dictates whether or not an electron can pass through. If the voltage applied to the QPC is much higher than that of the electrons, then the electron will be unable to pass and will be reflected, whereas if the voltage applied is much lower, the electron can pass through with no issue and is transmitted. Electrons of a similar energy to the potential on the QPC beamsplitter will be reflected and transmitted at an approximately 50:50 ratio, with the probability of each increasing or decreasing as the electron energy moves away from that of the QPC potential. The detectors in the electron system are made of Ohmic contacts. These perfectly absorb the electrons, leading to an electronic pulse passing a current over the contact, which is the indicator that an electron has been absorbed [35, 36]. In experiments the electrons are constantly being detected and are therefore measured as a continuous current using these ohmic contacts as detectors, however the use of time-dependent detector gates allows for single electron properties to be derived [37].

1.4 Thesis overview

There are two main concepts that will be considered in this thesis, phase averaging, which will be covered in part II and LO-phonon emission, which is in part III. Here I will briefly summarise these topics before giving an overview of the structure of this thesis.

1.4.1 Phase averaging

There is an uncertainty in the energy at which electrons are injected by a SES, which we can model as Gaussian. The typical width of one of these electron wavepackets for theoretical purposes is around 1 meV [38]. The expected path of an electron is called the "guide centre". These guide centres are not exact paths followed by the electrons, but, as the name suggests, guides for the central peak of the electron wave packets of the expected injection energy. This spread in energy leads to different guide centres for the electron to travel, with higher (lower) energy electrons following a guide centre closer to (further from) the edge. These different guide centres change the path length followed by the electron by a not-insignificant amount, as we will see later in the thesis.

These differences from the guide centre change the path length of the system and therefore also the area surrounded by the upper and lower path of the MZI. There are two phases of the electron that are directly affected by these small changes: the AB phase, ϕ_{AB}, which is proportional to the area enclosed by the paths; and the dynamical phase, ϕ_{dyn}, which is proportional to the difference between the upper and lower path lengths. These are calculated in Chapter 3. There is also a contribution from the phase obtained within the QPC beamsplitter, ϕ_{BS}, which is more subtle. This is dealt with in Chapter 4, which considers the arrival time distributions for both symmetric and asymmetric beamsplitters.

We find that unlike single-photon systems, where the path lengths are optimally the same length, in single-electron systems we actually maximise the visibility of the experiments when we set the arms with an offset l_{offset}, determined by the energy and therefore velocity of the electron. The value of this offset for hot-electrons is a significant proportion of the size of the whole MZI, which means that it is important that it is taken into account when building these interferometry experiments in order to maximise visibility. Fortunately, it also means that the contribution of phase averaging to the dephasing in an electronic MZI can be completely turned off by building the interferometer with the correct dimensions for the parameters at which the experiment will be conducted.

1.4.2 LO-phonon emission

A phonon is a quantised vibration of atoms and molecules in a lattice. If these vibrations are out of phase, they are called optical phonons. These phonons have specific energies depending on the material they are in. For gallium arsenide (GaAs), which is the material that the systems we consider are made from, they have an energy of 36 meV, so when single-electrons were detected with energies that were integer multiples of 36 meV below their initial injected energy, this was experimental evidence of the presence of LO phonons in the MZI systems we have discussed [24].

The behaviour of hot electrons after LO-phonon emission has been modelled semiclassically, looking only at the diagonal population terms of the density matrix which describes their behaviour [23]. As we now want to explore more quantum behaviour of electrons, we need to look at the fully quantum picture, so we must also consider the coherence (off-diagonal) terms of the density matrix. In this thesis, I derive this full quantum master equation for a complete description of hot electron behaviour after LO-phonon emission. We see that the diagonal rates are only appropriate for very small differences in wavenumber, after which the coherence terms become important. We present numerical simulations of a moving wavepacket with these off-diagonal coherence terms included. We find that there is dissipation and dispersion related to these off-diagonal elements, and we investigate the time and energy ranges for which these values need to be considered.

1.4.3 Thesis structure

Chapter 2 introduces some of the more technical concepts in the background that have not already been discussed in Chapter 1, including details of the physical structures we consider in this thesis and the mathematical derivation of the dispersion relation and velocity of electrons used throughout this work.

In Part II, we look at the effect of phase averaging on the visibility and arrival time distribution of electrons in a MZI. In Chapter 3 we introduce the research that has been conducted previously into the different sources of dephasing and decoherence in electron quantum optics, for both thermal electrons and hot-electrons. Later in this chapter, we introduce the concept of phase averaging. Using a simplified model of the beamsplitters, we will focus on the contribution of the phases picked up due to the geometry of the system on the visibility of experiments. Previous approaches have ignored the effect of the uncertainty in the wavepacket energy on the overall visibility, which is what is addressed in this thesis, in order to ascertain

optimum conditions for experiments. In Chapter 4 the arrival time distributions of the electron are calculated and modelled numerically for both a simplified and full case for the beamsplitters, and the effect of build parameters from Chapter 3 are also taken into account. So far the beamsplitters have been assumed to have symmetric phases, however in this chapter we will introduce the concept of asymmetry in the beamsplitters. The derivations of the full beamsplitter phases are by Sungguen Ryu in Ref. [39].

In Part III, we consider the rate of LO-phonon emission and behaviour of electrons after emitting an LO phonon. In Chapter 5 the first experimental observations of LO-phonons are introduced, and we explore how their discovery was made and the subsequent attempts to model the phenomenon semiclassically. We also introduce some of the tools that we will use in Chapter 6 to derive the fully-coherent master equation. In chapter 6, the master equation to describe the interaction between electrons and LO-phonons in these single-electron systems is derived, including the coherences that have been ignored in previous works, to form a complete quantum picture of the behaviour. The rates of emission of the LO-phonons are calculated using this master equation and compared to those found in previous works. We also begin to derive an equation of motion describing the behaviour electrons undergoing phonon emission, and model the motion of the electron in real space.

In Part IV we conclude by drawing together the results from Parts II and III to explain how they come together to affect hot-electron quantum optics experiments. We also speculate on potential future uses for our findings in both experiments and dynamical simulations.

Chapter 2

Quantum transport and solid-state physics

In this chapter, I will introduce the underlying theoretical concepts and derivations required to understand the systems that we will be considering throughout the rest of this thesis. Together with the previous chapter, they combine to allow the research presented in this thesis to take place, describing theoretical limits for optimal experimental builds.

2.1 Mesoscopic physics

Solid state physics is the study of how the atomic properties of a material affect its macroscopic behaviour. When considering the world of solid state physics and conductors, there is a distinct model of the microscopic world of atoms and of the macroscopic world of our everyday interactions, but what happens in the transition between the two? How do we define objects that are larger than an atom, but smaller than the characteristic lengths of electrons? Especially given the fact that these characteristic lengths can vary greatly in size themselves. Enter, mesoscopic physics. This is the name given to the study of conductors in this size range, usually made from a 2DEG (see section 2.2). This became relevant in the 1980s, when the possibility of creating conductors small enough to require this new description became a reality [40].

As mentioned above, a system is mesoscopic rather than microscopic when it is larger than the characteristic lengths of electrons. There are three lengths in particular that are important here.

- The de Broglie wavelength,
$$\lambda = \frac{h}{mv} \tag{2.1}$$
is the wavelength of a particle of a certain mass and energy, when looked at from the wave point of view in wave-particle duality [41]. Here, h is Planck's constant, m is the mass of the particle and v the velocity.

- The mean free path is the characteristic distance that an electron can travel before it's initial momentum is destroyed, and is given by
$$L_m = v\tau_m \tag{2.2}$$

where v is the velocity of the particle and τ_m is the momentum relaxation time [40].

- The phase relaxation length is the distance that an electron can travel before its initial phase is destroyed. This is slightly more complex than the momentum relaxation time, but is intrinsically linked with its properties. If the phase relaxation time is smaller than the momentum relaxation time then we have [40]

$$L_\phi = v\tau_\phi \tag{2.3}$$

where v is the velocity and τ_ϕ is the phase relaxation time. However, if the momentum relaxation time is significantly smaller than the phase relaxation time, this is no longer the case. After each momentum relaxation time, the velocity is randomised, such that at the end of a longer phase relaxation time we must take the root mean squared distance travelled instead, which results in a phase relaxation length of

$$L_\phi^2 = \frac{v^2\tau_m\tau_\phi}{2}. \tag{2.4}$$

The mean free path and phase relaxation length obviously differ depending on the medium through which the electron is travelling and the energy of the system as a whole, but making a system which is smaller than these lengths means that electrons can now be used in new and exciting ways, without having to worry about interactions that would otherwise render experiments useless, and without losing all useful information from them. A typical value of the momentum relaxation time for electrons in GaAs is $\tau_m \approx 10\,\text{ns}$, and as GaAs is a high-electron-mobility-transistor (HEMT) [42], the phase relaxation time τ_ϕ is approximately equal to the momentum relaxation time [40].

2.2 Two-dimensional electron gas (2DEG)

In order to conduct experiments there needs to be a method of transport for the electrons, and a medium through which they can travel. A 2DEG is a system which provides a high quality conductive channel through which the electrons can travel [40]. Some of the earliest experiments using 2DEGs used the surface of liquid helium on which free electrons can float and move, as demonstrated in Ref. [43]. More recently, three-layer graphene films have been used [44]. These offer the advantage of being solid objects which can be etched, patterned, and have metallic gates attached, which are useful qualities for experiments as we will see below.

Commonly used in experiments today are gallium arsenide (GaAs) and aluminium gallium arsenide (AlGaAs) heterostructures [45]. At the boundary between GaAs/AlGaAs layers a thin conducting layer is formed, with a typical carrier concentration between $2 \times 10^{11}\text{cm}^{-2}$ and $2 \times 10^{12}\text{cm}^{-2}$ [40]. These 2DEGs can be manipulated by applying a voltage to metallic gates placed above the layer of electrons. The area underneath these gates will then be depleted of electrons, leaving an empty gap in the 2DEG. This allows for experiments to be built entirely within the 2DEG, as paths and obstacles can be created and manipulated by applying specific voltages to the gates. Examples of these will be discussed later. Figure. 2.1

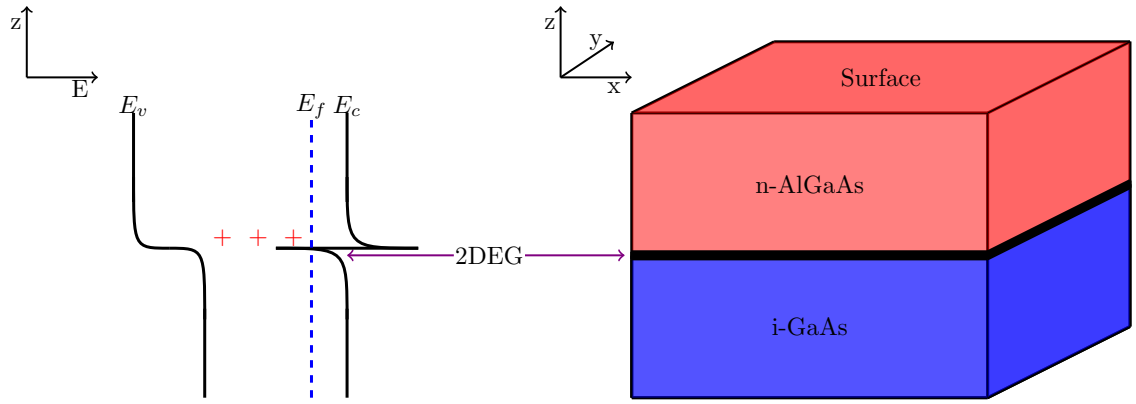

Figure 2.1: Adapted from Ref. [40]. A 2DEG is formed between layers of AlGaAs and GaAs. The Fermi level for GaAs is lower than that of AlGaAs, and when the two materials are brought together electrons spill over from the AlGaAs side into the GaAs layer, leaving behind positive charges, which causes the valence and conduction bands to bend. The Fermi energy evens out everywhere, which leaves a well of electrons between the materials, which is the 2DEG.

depicts this set up for a 2DEG in a GaAs/AlGaAs set up, as well as the energy level differences that form the layer of electrons.

2.3 Classical Hall effect

When electrons are confined to two-dimensions (x, y), as in the 2DEGs described above, and have a magnetic field applied in the z-direction, some very interesting physics can be observed outside of what one would ordinarily expect in the 3D world.

The application of a magnetic field to the 2D layer of electrons causes them to follow a circular path perpendicular to the field, as shown in Fig. 2.2. This path is described by the classical mechanics dictating the movement of a charged particle under a magnetic field. The force exerted on a charged particle by a magnetic field is known as the Lorentz force, and is given by,

$$\mathbf{F} = q\mathbf{v} \times \mathbf{B}, \tag{2.5}$$

where q is the charge of the particle, $\mathbf{v}$ is the velocity and $\mathbf{B}$ is the magnetic field vector. For an electron, this can be written as

$$\mathbf{F_e} = m\frac{\mathrm{d}\mathbf{v}}{\mathrm{d}t} = -e\mathbf{v} \times \mathbf{B}, \tag{2.6}$$

where m is the mass of the electron, and $e > 0$ is the charge of the electron.

The particle is confined to only the two dimensions (x, y), so the velocity in the z-direction is zero, and the velocity vector becomes $\mathbf{v} = (v_x, v_y, 0)$. The magnetic field is applied only in the z-direction, so the x and y components are zero, giving a magnetic field vector of $\mathbf{B} = (0, 0, B)$.

This gives us

$$\mathbf{F_e} = -e(yB, -xB, 0), \tag{2.7}$$

so the x component is

$$m\frac{\mathrm{d}v_x}{\mathrm{d}t} = -eyB, \tag{2.8}$$

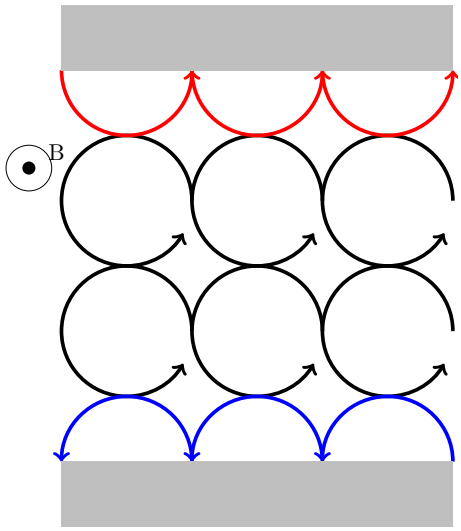

Figure 2.2: An example of the paths followed by electrons in a 2DEG with a magnetic field applied "out of the page". The electrons follow circular paths the radius of which are determined by the physical parameters of the system, in particular the magnitude of the magnetic field. The electrons at the edge of the system try to follow this same path, but they are blocked by the edge, and cannot "bounce" back on themselves, so they continue along, essentially bouncing along the edge of the system, allowing them to travel, inducing a current. The size of these orbits determines how far away the electrons travel from the edge, which is known as the guide centre.

and the y component is

$$m\frac{\mathrm{d}v_y}{\mathrm{d}t} = exB. \tag{2.9}$$

The Lorentz force acts perpendicular to both the direction of the magnetic field and the velocity, pushing the electron around in a circle, the direction of which is dependent on the direction of the magnetic field, and the radius of the circle is determined by the strength of the magnetic field. The electrons away from the edges of the sample will stay in place following the same circular path, resulting in a current of 0, but at the edges of the system the electron cannot continue on it's circular path, and cannot move in any other direction, so it "bounces" along the edge, as shown in Fig. 2.2. The distance away from the edge that the electron travels is the guide centre that we introduced in chapter 1. This is the classical picture for the mechanism of electron transport in a 2DEG.

It is also useful to introduce the cyclotron frequency, ω_c, which is calculated by equating the Lorentz force (F_L) with the centripetal force (F_c),

$$\begin{aligned} F_C = \frac{mv^2}{r}; \qquad & F_L = evB, \\ \Rightarrow \frac{mv}{r} = eB, & \end{aligned}$$

where m and e are the mass and charge of the particle respectively and r is the radius of the circular path. Angular velocity is given by $\omega_c = v/r$, which means that we have

$$\omega_c = \frac{v}{r} = \frac{eB}{m}. \tag{2.10}$$

The chirality of the system which the Hall effect provides can be seen in Fig. 2.2, as the electrons on opposite edges are forced to move in opposite directions.

2.4 Quantum Hall effect

The 1985 Nobel prize was awarded to Klaus von Klitzing for his discovery of the quantum Hall effect. In his 1980 paper his group performed experiments to investigate the fine structure constant of electrons in 2DEGs, and in doing so, discovered that the energy levels of the electron orbitals were exactly quantised in integer multiples of h/e^2, where h is Planck's constant and e is the electron charge [46]. This was a surprising result, followed closely by a further surprise - the fractional quantum Hall effect [47]. The crux of this discovery was that not only are electron orbitals quantised at integer multiples of h/e^2, but also quantised at specific fractions, h/fe^2, where $f = 1/3$ and $2/3$, which was explained using a multi-particle model [48]. Although the fractional quantum Hall effect is not used in this thesis, this discovery made waves in the mesoscopic physics community [49].

As we saw above in the classical picture, the radius of the circular paths is inversely proportional to the magnetic field, getting smaller as the magnetic field gets larger. When considered from a quantum mechanical perspective, we see that there are plateaus for ranges of magnetic fields, followed by sharp jumps up to another "radius" which in reality would be the reisistance. The experimental observations of these plateaus are so accurate that the quantum Hall effect is now used as the standard for resistance [50].

In order to enter the quantum Hall regime we must have both a very low temperature and a very high magnetic field acting perperndicular to the plane of the material. We must of course quantify what we mean by "very high" and "very low". An example of this can be seen in the 2003 paper by Ji *et al.* as discussed in section 1.3, where the experimental conditions used to enter the quantum Hall regime are a magnetic field of $B \sim 5.5$T and an environment temperature of $T \sim 6$mK [33].

2.5 Aharonov-Bohm phase

The AB phase is the name given to the phase experienced by an electron due to a magnetic or electric field, despite being shielded from the field [34]. In classical physics, only the field is important in describing the properties of charges and currents. It had previously been assumed that the potential was included only for mathematical purposes, and had no physical effect on them. The observation of the AB effect changes this, as a physical manifestation of the electromagnetic potential can be seen in the change in the interference pattern due to a present, but shielded magnetic field.

In their paper, Aharonov and Bohm suggest possible experimental set-ups with which to observe the predicted effect [34], such as that shown in Fig. 2.3, where a solenoid is placed in between the two slits in a double-slit experiment, but shielded from the rest. If the AB phase shift is indeed present, then a shift in the interference pattern should be seen when the solenoid is turned on. The next year R. G. Chambers observed just that [51]. There was however, much speculation that the effects may have been due to the solenoid not being appropriately shielded, and so, many

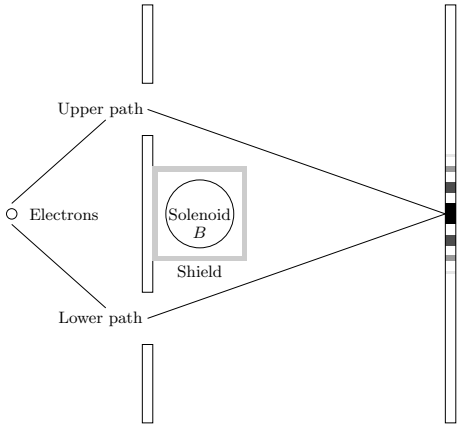

Figure 2.3: A schematic of the setup for an experiment to examine the AB phase. This is a Young's double slit experiment with electrons. A solenoid has been placed in between the two slits on the screen side, and has then been shielded from the rest of the experiment. Despite the fact that electrons never enter the magnetic field of the solenoid, a phase shift due to the field can be seen in the interference pattern on the screen when the solenoid is turned on.

more experiments were conducted to prove this until in 1986 an experiment was conducted which laid waste to all scepticism, by covering the magnet with both a superconducting layer and a copper layer to ensure absolutely no field could escape [52].

The phase picked up along a path S, is calculated as

$$\phi_{\mathrm{AB}}^{(S)} = \frac{q}{\hbar} \oint_S \mathbf{A} \cdot \mathrm{d}\mathbf{x}, \tag{2.11}$$

where $\mathbf{A}$ is the vector potential, and $\oint_S \mathbf{A}\,\mathrm{d}\mathbf{x} = \int H\,\mathrm{d}S$ is the total magnetic field inside the circuit [34]. As this gives a constant value, $A \neq 0$, within the circuit.

2.6 Landau levels and edge channels

Electrons in a system such as a 2DEG can be described by [40]

$$\left[E_c + \frac{1}{2m_e^*}\left(i\hbar\nabla + e\mathbf{A}\right)^2 + U(\mathbf{r})\right]\mathbf{\Psi}(\mathbf{r}) = E\mathbf{\Psi}(\mathbf{r}) \tag{2.12}$$

where E_c is the bulk band bottom energy, $U(\mathbf{r})$ is the confinement energy in each of the three-dimensions, $\mathbf{r} = \{x, y, z\}$, $\mathbf{A}$ is the vector potential and $m_e^* = 0.067m_e$ is the effective mass of an electron in GaAs. The electron charge is given by $e > 0$. This is the Schrödinger equation, where the Hamiltonian is

$$\hat{H}(\mathbf{r}) = E_c + \frac{1}{2m_e^*}\left(i\hbar\nabla + e\mathbf{A}\right)^2 + U(\mathbf{r}), \tag{2.13}$$

so we will start here.

Our system is unconfined in the x-direction, which means that the x-component of $U(\mathbf{r})$ is 0. Assuming these potentials are decoupled, our Hamiltonian then becomes

$$\hat{H}(\mathbf{r}) = E_c + \frac{1}{2m_e^*}\left(i\hbar\nabla + e\mathbf{A}\right)^2 + U(y) + U(z). \tag{2.14}$$

We consider the case where electron transport occurs in the quantum Hall regime. In order to enter this regime, we know we must have a strong magnetic field, so $B \gg 0$. We choose to work in the Landau Gauge, where the vector potential is $\mathbf{A} = -By\hat{e}_x$, and $\hat{e}_x$ is the unit vector in the x-direction. To simplify further, we can introduce the momentum operator, $\hat{\mathbf{p}} = -i\hbar\frac{\partial}{\partial x}$ in one-dimension and

$$\hat{\mathbf{p}} = -i\hbar\nabla. \tag{2.15}$$

in three-dimensions

We can substitute this into (2.13), to give

$$\begin{aligned}\hat{H}(\mathbf{r}) &= E_c + \frac{1}{2m_e^*}\left(-\hat{\mathbf{p}} - e\mathbf{A}\right)^2 + U(y) + U(z),\\ &= E_c + \frac{1}{2m_e^*}\left(\hat{\mathbf{p}} - eBye_x\right)^2 + U(y) + U(z).\end{aligned} \tag{2.16}$$

This equation can now be split into it's x, y and z components, giving

$$\hat{H}(\mathbf{r}) = E_c + \frac{1}{2m_e^*}\left(p_x - eBy\right)^2 + \frac{p_y^2}{2m_e^*} + U(y) + \frac{p_z^2}{2m_e^*} + U(z). \tag{2.17}$$

We can now introduce the quantum numbers based on the different confinements in the x-, y- and z-directions. In the x direction, the electrons propagate freely, meaning that they can be defined in terms of only the momentum k_x. In the y-direction, we have weak parabolic confinement, $U(y)$, so the electrons are quantised with respect to the Landau level, with quantum number m, where the lower m is, the tighter the quantum Hall "ring" is in which the electron moves. There is approximately 10 meV between levels, which is a large jump, so we can assume that the electron stays in the lowest level. There is still some movement in the y-direction due to the weak confinement, so the momentum k is also used here. In the z-direction we have very strong confinement, $U(z)$, such that the electron can only move in the x- and y-directions. This confinement can be modelled as an infinite square well or, more realistically, a triangular well. For the tight confinement we use here, these wells are very narrow and the energy levels are very far apart, such that the electron cannot move between them. These are quantised with quantum number n.

Using these confinements, the Schrödinger equation for this system reads

$$\hat{H}(\mathbf{r})\mathbf{\Psi_n}(\mathbf{r}) = E_\mathbf{n}\mathbf{\Psi_n} \tag{2.18}$$

where $\mathbf{n} = \{n, m, k_x\}$ are the indices. In order to solve the Schrödinger equation, we need to introduce the separable Ansatz,

$$\Psi_\mathbf{n}(\mathbf{r}) = \psi_{k_x}(x)\chi_{mk_x}(y)\phi_n(z). \tag{2.19}$$

We will now look at each direction separately. In the z-direction, we have

$$\epsilon_n\phi_n(z) = E_c + \left(\frac{p_z^2}{2m_e^*} + U(z)\right)\phi_n(z). \tag{2.20}$$

where E_c is the band edge energy, p_z is the momentum in the z-direction, m_e^* is the effective electron mass in GaAs and $U(z)$ is the confinement in the z direction. If

we assume this takes the form of an infinite square well, the wavefunctions are given by

$$\phi_n(z) = \begin{cases} \sqrt{\frac{2}{a}}\sin(k_z z) & \text{if } 0 \leq z \leq a \\ 0 & \text{otherwise} \end{cases} \tag{2.21}$$

where $k_z = \frac{\pi n}{a}$ and $n = 1, 2, ...$ We can also see the same effect with a triangular well, the wavefunction for which is given by [53]

$$\phi_n(z) = \begin{cases} \sqrt{2a^3} z e^{-z/(2a)} & \text{if } 0 \leq z \leq a \\ 0 & \text{otherwise} \end{cases} \tag{2.22}$$

With the tight confinement in the z-direction found in a 2DEG, we assume always that $n = 1$. The simulations throughout this thesis use a triangular well, with a width parameter of $a = 3\,\text{nm}$ [54, 24].

In the x-direction the motion of the electron is unconfined, which means that it can be described as a plane wave, normalised over the length of the conductor, L_x, i.e.,

$$\psi_{k_x}(x) = \frac{1}{\sqrt{L_x}} e^{ik_x x}. \tag{2.23}$$

The y-direction is slightly more complicated. We assume weak parabolic confinement in this direction,

$$U(y) = \frac{1}{2} m_e^* \omega_y^2 y^2, \tag{2.24}$$

where $\hbar\omega_y$ is the confinement frequency, and is taken to be 2.7 meV.s for all of our calculations. Combining this with the vector potential defined above, the Hamiltonian in the y-direction becomes

$$\hat{H}_{nk_x}(y) = \epsilon_n + \frac{(\hbar k_x - eBy)^2}{2m_e^*} + \frac{p_y^2}{2m_e^*} + \frac{1}{2} m_e^* \omega_y y^2 \tag{2.25}$$

which has the solution

$$\hat{H}_{nk_x}(y)\chi_{mk_x}(y) = E_{\mathbf{n}}\chi_{mk_x}(y). \tag{2.26}$$

where χ_{mk_x} are the eigenfunctions for the Hamiltonian. To find these eigenfunctions, it is useful now to write this in terms of the cyclotron frequency,

$$\omega_c = \frac{eB}{m_e^*}, \tag{2.27}$$

and the guide centre co-ordinate,

$$y_G(k) = \frac{\omega_c^2}{\Omega^2}\frac{\hbar k_x}{eB} = \frac{\omega_c}{\Omega^2}\frac{\hbar k_x}{m_e^*} \tag{2.28}$$

where $\Omega^2 = \omega_c^2 + \omega_y^2$ is the compound frequency made up of the cyclotron frequency ω_c and the confinement frequency in the y-direction, ω_y. We can then use these definitions to rewrite Eq. (2.25) as

$$\begin{aligned} \hat{H}_{nk_x}(y) &= \epsilon_n + \frac{(\hbar k_x - m_e^*\omega_c y)^2}{2m_e^*} + \frac{p_y^2}{2m_e^*} + \frac{1}{2} m_e^* \omega_y^2 y^2 \\ &= \epsilon_n + \frac{p_y^2}{2m_e^*} + \frac{\hbar^2 k_x^2}{2m_e^*} - \hbar k_x \omega_c y + \frac{1}{2} m_e^* \Omega^2 y^2. \end{aligned} \tag{2.29}$$

Now using the definition of the guide centre co-ordinate given above, we can further simplify

$$\begin{aligned}\hat{H}_{nk_x} &= \epsilon_n + \frac{p_y^2}{2m_e^*} + \frac{1}{2m_e^*}\left[\frac{\Omega^4}{\omega_c^2}m_e^* y_G^2\right] - \Omega^2 m_e^* y_G y + \frac{1}{2}m_e^*\Omega^2 y^2 \\ &= \epsilon_n + \frac{p_y^2}{2m_e^*} + \frac{1}{2}m_e^*\Omega^2\left[\frac{(\omega_c^2+\omega_y^2)}{\omega_c^2}y_G^2 - 2yy_G + y^2\right] \\ &= \epsilon_n + \frac{p_y^2}{2m_e^*} + \frac{1}{2}m_e^*\Omega^2\frac{\omega_y^2}{\omega_c^2}y_G^2 + \frac{1}{2}m_e^*\Omega^2(y-y_G)^2 \\ &= \epsilon_n + \frac{p_y^2}{2m_e^*} + \frac{\hbar^2 k_x^2}{2m_e^*}\frac{\omega_y^2}{\Omega^2} + \frac{1}{2}m_e^*\Omega^2(y-y_G)^2 \end{aligned} \tag{2.30}$$

This is a displaced harmonic oscillator, so we know that the eigenfunctions are

$$\chi_{mk_x}(y) = \frac{1}{l_\Omega}u_m\left(\frac{y-y_G(k)}{l_\Omega}\right) \tag{2.31}$$

where

$$l_\Omega = \sqrt{\frac{\hbar}{m_e^*\Omega}} \tag{2.32}$$

is the effective confinement length, which is the size of the parabolic trap, and

$$u_m(s) = \frac{1}{\sqrt{2^m m!}}\frac{1}{\pi^{1/4}}e^{-s^2/2}H_m(s) \tag{2.33}$$

where H_m are the Hermite polynomials, $H_0(x) = 1$, $H_1(x) = 2x$, $H_2(x) = 4x^2 - 2$, and so on to higher orders.

In the work we will be discussing, we only consider the lowest Landau level, where $m = 0$, so

$$u_0(s) = \frac{e^{-s^2/2}}{\pi^{1/4}}. \tag{2.34}$$

The eigenfunctions are therefore

$$\chi_{0k_x} = \sqrt{\frac{1}{l_\Omega\pi^{1/2}}}\exp\left[-\frac{1}{2}\left(\frac{y-y_G(k)}{l_\Omega}\right)^2\right]. \tag{2.35}$$

We can now solve the Schrödinger equation for $E_{\mathbf{n}}$ which will give us the dispersion relation for the electrons. We can do this with the equation for the y-direction, Eq. (2.26). First we multiply both sides of the equation by $\chi^*_{m'k'_x}$, and then we integrate over y.

$$\begin{aligned}\int \mathrm{d}y\chi^*_{m'k'_x}(y)\hat{H}_{nk_x}(y)\chi_{mk_x}(y) &= \int \mathrm{d}y\chi^*_{m'k'_x}(y)E_{\mathbf{n}}\chi_{mk_x}(y), \\ \Rightarrow \int \mathrm{d}y\chi^*_{m'k'_x}\hat{H}_{nk_x}\chi_{mk_x} &= E_{\mathbf{n}}\int \mathrm{d}y\chi^*_{m'k'_x}(y)\chi_{mk_x}(y), \\ \Rightarrow \int \mathrm{d}y\chi^*_{m'k'_x}\hat{H}_{nk_x}\chi_{mk_x} &= E_{\mathbf{n}}\delta_{m'm}\delta_{k'_x k_x}. \end{aligned} \tag{2.36}$$

which introduces the Kronecker deltas, $\delta_{m'm}$ and $\delta_{k'_x k_x}$. These are defined as

$$\delta_{m'm} = \begin{cases} 1 & \text{if } m = m' \\ 0 & \text{if } m \neq m' \end{cases} . \tag{2.37}$$

In order for this integral not to be zero, we must set $m = m'$ and $k_x = k'_x$, such that the integral can be written as

$$\int \mathrm{d}y \chi^*_{mk_x}(y) \hat{H}_{nk_x}(y) \chi_{mk_x}(y) = E_{\mathbf{n}}. \tag{2.38}$$

If we now combine Eq. (2.35) and Eq. (2.30) with this integral, we get

$$\begin{aligned} E_{\mathbf{n}} = \frac{1}{l_\Omega \pi^{1/2}} \int \mathrm{d}y \exp\left[-\frac{1}{2}\left(\frac{y - y_G(k)}{l_\Omega}\right)^2\right] \\ \times \left[\epsilon_n + \frac{p_y^2}{2m_e^*} + \frac{\hbar^2 k_x^2}{2m_e^*}\frac{\omega_y^2}{\Omega^2} + \frac{1}{2}m_e^*\Omega^2(y - y_G)^2\right] \exp\left[-\frac{1}{2}\left(\frac{y - y_G(k)}{l_\Omega}\right)^2\right] \end{aligned} \tag{2.39}$$

First we apply the momentum operator, giving

$$E_{\mathbf{n}} = \frac{1}{l_\Omega \pi^{1/2}} \int \mathrm{d}y \chi^*_{mk_x} \exp\left[-\left(\frac{y - y_G(k)}{l_\Omega}\right)^2\right] \sqrt{\frac{1}{l_\Omega \pi^{1/2}}} \left[\epsilon_n + \frac{k_x^2 \hbar^2}{2m_e^*}\frac{\omega_y^2}{\Omega^2} + \frac{1}{2}\hbar\Omega\right] \tag{2.40}$$

and now performing the integral gives us a dispersion relation of

$$E_{\mathbf{n}} = \epsilon_n + \frac{1}{2}\hbar\Omega + \frac{\omega_y^2}{\Omega^2}\frac{\hbar^2 k_x^2}{2m_e^*}. \tag{2.41}$$

This dispersion relation is central to the description of the systems in use throughout this thesis. The velocity of the electron can be derived from this dispersion relation, as [40]

$$v(n,k) = \frac{1}{\hbar}\frac{\partial E(n,k)}{\partial k_x} = \frac{\hbar k}{m_e^*}\frac{\omega_y^2}{\Omega^2}. \tag{2.42}$$

Throughout this thesis we will assume the electron wavepackets move with a constant velocity across the whole wavepacket, such that $v = v_0$. The energy dispersion describes the energy levels in which the electron travels, which are also visualised in Fig. 2.4. Here, the blue dashed and red dotted lines show the edge channels in which an electron travels. The lines closer to the edge have a higher energy than those travelling further away from the edge. We can also see the chirality here, as we could in Fig. 2.2.

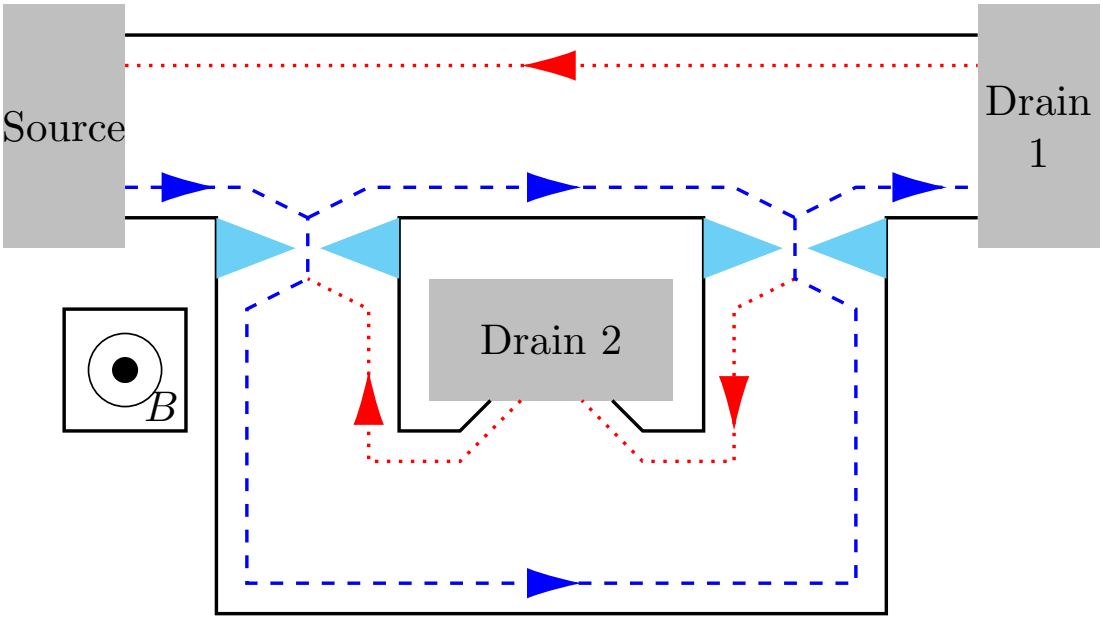

Figure 2.4: Hall bar geometry showing the dynamics of an MZI. The blue triangles represent the QPCs. The edge channels are shown as blue dashed and red dotted lines. We can see the different edge channels which can be occupied depending on the energy of the system, and also the chirality that comes from the magnetic field direction and skipping orbits sketched in Fig. 2.2. Adapted from Ref. [33].

Part II

Phase Averaging

Chapter 3

Optimising electron interferometry experiments

Over the next two chapters, we will introduce the ongoing research into experiments using both DC sources and SES, and address the methods used in previous works to describe the behaviour of electrons in these systems. We will also address the differences between techniques used to analyse the behaviour in systems using DC sources, cold SESs and finally a new type of SES which allows for the injection of hot-electrons. We will then derive an equation for the current in an electronic MZI and use this to calculate the visibility of the system under different conditions. In this work, we will also include a term that takes into consideration the uncertainty in the energy of the injected electron, and investigate the effect that this uncertainty has on the visibility of the system and how any reduction in visibility can be reduced.

To focus on the key physics, in Chapter 3 we consider a simple model of the beamsplitters, initially with transmission and reflection coefficients $T = R = 1/2$, before introducing a simplified calculation of the beamsplitter phase. In Chapter 4 we will go on to introduce the full effect of the energy dependence of the beamsplitters, including the phases introduced by them which we have neglected in Chapter 3. Again, we will begin with a simplified model of the induced phases, before introducing the full model as derived in Ref. [39].

3.1 Experiments with DC sources

In 2003, Ji *et al.* became the first to realise an electronic analogue of the optical MZI [33]. This interferometer was created in a GaAs-AlGaAs 2DEG, using QPCs as beamsplitters and ohmic contacts as electron detectors. The interferometers were found to have a visibility of 62%, which at the time was considered a very high visibility. It was also observed that with increasing temperature and electron energy, the visibility was reduced, although at the time the source of the decoherence was unknown (though they were able to show that it was not from inelastic scattering events). This realisation paved the way for future electron quantum-optics experiments.

The earlier experiments were conducted with thermal electrons, i.e. electrons with energies close to the Fermi level. In 2006, Neder *et al.* developed an experimental set up similar to that in Ref.[33], but with an additional quantum dot which

allowed for the choice of whether the beam entered the outer edge channel, or the inner [55]. As in Ref. [33], the length of the interferometer arms could be adjusted using modulation gates, in order to change the phase between the two arms using the AB effect [34]. It was found that the visibility of the system evolves in what they refer to as a "lobe" pattern, as a function of energy. The visibility appeared to drop to 0% for certain values of energy, at which points the phase, which is otherwise constant, jumps by π, and then returns abruptly back to it's constant value. Reducing the magnetic field reduced the overall visibility, and the periodicity of the lobes got smaller. Changing the path lengths of the interferometer did not affect the phase or periodicity of the lobes, but the visibility decreased as the path difference increased. This unusual behaviour could not be explained by the single particle model because of the energy dependence of the transmission, and suggests that there was interference of the electrons with their surroundings.

The decoherence of a single electron MZI was investigated further in 2007 by Litvin *et al.*, specifically the effects of temperature and voltage on the quantum interference [56]. The visibilities for this experiment were found to be significantly lower than those predicted by the theory in Ref. [57] and those found in the previous experiments by Ref. [33]. The reduction in the visibilities were considered as two contributions, one from the AB phase, distinguishable by its shift with magnetic field, and a contribution of small period oscillations from an unknown source suspected to be electrostatic in nature due to their independence from the magnetic field changes. After investigating the effect of both temperature and bias voltage on the decay of the oscillations (and therefore visibility) from both sources, it was found that the visibility decreases steadily with increasing temperature of the system and also the bias voltage. While the shape of the results matched that predicted by theory, the experimental visibility was in fact 80 times smaller than predicted by the theory. The suggested reasoning behind this small visibility is that the internal degrees of freedom of the QPC are very sensitive to the shape of the QPC potential, and in these experiments, the QPCs were shaped very differently from the ideal case assumed by the theory in Ref. [57].

In 2007, Roulleau *et al.* developed a statistical method to determine the visibility in electronic MZIs [58]. The experiments discussed previously had seen behaviours in visibility that were quite different in terms of value. It was determined that the phase averaging took the form of a Gaussian, proportional to the voltage squared; however, the source of this phase averaging was at this point still unknown. Although it has been known for a long time that there is a coherence length related to the edge states in quantum Hall edge channels, up until 2008, the exact value of this was not known. In their 2008 paper, Roulleau *et al.* present a method to determine a value for this [59]. The visibility was measured in the same system described in Ref. [58], and was found to decrease exponentially with temperature. They then define a coherence length, l_ϕ, such that $\mathcal{V} = \mathcal{V}_0 e^{-2L/l_\phi}$ and $l_\phi \propto T^{-1}$, where $\mathcal{V}$ is the temperature dependent visibility, $\mathcal{V}_0$ is the temperature independent contribution to the visibility and L is the length of the interferometer. The coherence length can then be inferred by looking at the visibility decrease of three different sizes of MZI.

Later on in 2008, Roulleau *et al.* investigated how noise affects the dephasing of the same system [60]. It was found that the decrease in visibility is due to Gaussian noise, and the results of the experiments were used to calculate the dephasing due to thermal noise, which matched the measurements of coherence length from the

previous experiments [59] exceptionally well. They demonstrate that the thermal noise, as well as the coupling between the two edge states due to the overlap of the wavefunctions describing each edge state [61], is what determines the finite coherence length.

The next step for Roulleau *et al.* was in 2009 to show that if another "floating" ohmic contact is added into the system, it can be used to destroy the coherence of the system [62]. Electrons are absorbed by the ohmic contact, and then reintroduced into the system, such that the detected current is still predictable using the equations for visibility. The reinjected electrons, however, are not the same electrons that were absorbed, meaning that their phase is now randomised and they no longer contribute to the overall interference of the system, thereby destroying the coherence of the system.

In 2009, Bieri *et al.* combined the previous studies by investigating the effect of energy dependence on the transmission probability of the beamsplitters [63]. The experiments discussed previously all set their beamsplitter transmission and reflection coefficients to be $T = R = 1/2$ respectively, in order to ensure the wavepackets arrive at the second beamsplitter in the same amounts at the same time, to give maximum visibility. In this experiment, the symmetries of the QPCs was varied, such that the input QPC transmission varied between $0 - 100\%$ and the output QPC transmission remained constant. For certain values of T, it was found that the visibility actually increased from the value at 50%, rather than decreasing as would be expected, depending on the voltage bias. Their investigations showed that this is in fact a property of a MZI with edge states, and not the transmission of the QPCs as beamsplitters. This is due to the fact that in experiments, there may be more than one edge state in each path, which can be held at different voltages depending on how they are attached to the source contact or the ground. The visibility in a system where the current is detected in the outer edge state, is shown in Eq. (3.1). As there is a coupling to the inner edge state, γ, we can see that there can still be some increase in the visibility with voltage, even in the case of potential-independent beamsplitters [63],

$$\mathcal{V}_{\text{Bieri}} = 2\sqrt{\left(\hat{T}_{21} + V\frac{\partial \hat{T}_{21}}{\partial V}\right)^2 + \left(\hat{T}_{21}V\gamma\right)^2}. \tag{3.1}$$

Jump ahead seven years, and Tewari *et al.* found that, contrary to theoretical predictions, the visibility of the electrons in an MZI are actually independent of energy above a certain threshold, rather than continuing a steady decline [64]. This hints towards the existence of another relaxation mechanism which has yet to be investigated.

3.1.1 Explanations of interferometer visibility

In 2004 the dominant dephasing method in these electron interferometer experiments was unknown. Two methods were proposed in 2004 by Marquardt and Bruder [65], a fluctuating classical field approach and an approach which involves introducing a dephasing terminal to the interferometer. Looking at the mean current alone, the two methods were virtually indistinguishable, however when the visibility of the shot noise was considered instead the effect of the dephasing depended strongly on the fluctuations.

In 2005, the sources of dephasing we investigated further by Chung *et al.* [57] who investigated theoretically the effects of dephasing introduced by a voltage probe. They investigated specifically the effect of finite temperature, applied bias and the difference in path lengths between the arms of the interferometer, and they found the dependence of the visibility on the transparency of the beamsplitters. They show that the phase dependent oscillations are suppressed by a factor on the interference term of $\sqrt{1-\epsilon}$, where $\epsilon = 1$ is complete dephasing.

The decay of the AB oscillations, which have been used in the previous works to investigate the visibility, can also be used to determine the coherence length of the electrons [66]. In the work by Haack *et al.* [66], which instead of considering DC sources, used cold, single-electron sources, the effect of path length difference on this decay was investigated, and they found that as the path length difference was increased, the visibility of the system decreased.

The effect of electron-electron interactions in a ballistic MZI was discussed in detail by Neuenhahn and Marquardt in 2008 [67] for different energy regimes. The diminishing effect on the coherence of both propagation distance and energy was discussed and modelled using three different tools depending on the energy regime.

One thing which this still leaves unexplained however, is the unusual oscillations seen by Neder *et al.* [55] with changing bias. In 2008, Neder *et al.* [68] found that this was in fact due to the Coulomb interaction between electrons, and soon after, an explanation of this was offered by Levkivskyi *et al.* [69]. They noted that when the electrons interact with the QPCs, they excite plasmons. These excitations are related to the bias voltage applied to the QPC, which would explain the loss seen in Ref. [55].

3.2 Hot electron sources and decoherence

So far we have concentrated on so-called "cold" electrons which are at energies around the Fermi level. There have, however, been advances in electron pump technology [19] which allow electrons to be injected at energies well above the Fermi level [6, 21, 70–76], as discussed in Chapter 1. This gap in energy also translates to a physical separation in the electrons from their surroundings, significantly reducing the effects of electron-electron interactions. For example, if we look at the sketch in Fig. 3.1, we see that for an electron emitted at approximately 100 meV above the Fermi energy the spatial separation between the injected electrons and the bulk is approximately 100nm [22].

In Ref. [38], it was shown that a hot-electron wavepacket can be reliably generated by quantum-dot-based SES when the Landauer-Büttiker traversal time [77, 78], which is a time scale describing how long it takes for a plane wave to travel through a barrier, is much shorter than the passage time [79, 80] which is how long it takes for the wavepacket to evolve into an orthogonal state. The starting state for an electron wavepacket in the lowest Landau level (i.e. $m = 0$, such that $|mk\rangle = |0k\rangle$) with momenta distributed according to a Gaussian is given by

$$|\Psi(0)\rangle = \sum_k N_\alpha e^{-\alpha(k-k_0)^2} |0k\rangle = \frac{N_\alpha L}{2\pi} \int \mathrm{d}k e^{-\alpha(k-k_0)^2} |0k\rangle \,, \tag{3.2}$$

where the central energy and wavenumber of the wavepacket can be expressed in

terms of

$$k_0 = \sqrt{\frac{2m_e^*}{\hbar^2}\left(\frac{\Omega}{\omega_y}\right)^2 E_0}, \tag{3.3}$$

and with the norm,

$$N_\alpha = \frac{(8\alpha\pi)^{1/4}}{\sqrt{L}}. \tag{3.4}$$

We also have the quantum Hall energy eigenstate for an energy E_k in position representation, given by

$$\begin{aligned} |x,y\rangle \langle x,y|0k\rangle &= \frac{1}{\sqrt{L}} e^{ikx} \chi_{0k}(y) |x,y\rangle , \\ &= \frac{1}{\sqrt{L}} e^{ikx} \frac{1}{\pi^{1/4}\sqrt{l_\Omega}} \exp\left\{-\frac{1}{2}\left[\frac{y - y_G(k)}{l_\Omega}\right]^2\right\} |x,y\rangle . \end{aligned} \tag{3.5}$$

These will be used in future chapters to describe the electron wavepacket in specific conditions.

Hot electrons must be treated differently to cold electrons, as they have a much higher energy, which means that their sources of decoherence differ from those of electrons near the Fermi energy, as shown in Fig. 3.1, and they have very short life times. The short duration of these wavepackets means that matching their arrival at a beamsplitter in a MZI is essential for observing interference. A detailed description of the arrival time distributions and how they are affected by phase averaging is therefore required for successful design of hot-electron interferometry experiments.

When considering cold-electrons, the main source of decoherence was found to be in electron-electron interactions due to the injected electrons proximity to the electrons in the rest of the system, the main source of this being through plasmonic excitations [81–84]. As the energy of the electrons increases, however, the effect of plasmons is suppressed and other sources of decoherence take over, as shown in Fig. 3.1. A theoretical overview of the many sources of decoherence in an MZI can be found in Ref. [22].

In 2019, Ota *et al.* [25] performed a spectroscopic study of hot-electron transport, and observed experimentally the many different relaxation effects in the system. Looking at the lower end of the energy spectrum ($\sim$ 10 meV), one can see evidence to support the idea that plasmon excitations are indeed the primary source of decoherence, along with other electron-electron interactions. As the electrons move to higher energies, they their behaviour is close to ballistic, until at the higher energies ($\sim$ 100 meV) there are very clear echoes of the traces which appear at energies below the main detected electron. These are known as LO-phonon replicas, caused by electrons which have emitted an LO-phonon and are therefore detected at lower energies. LO-phonons have characteristic energies in different materials, so the appearance of these replicas at integer multiples of this energy below the injection energy are evidence that LO-phonon emission has become the dominant relaxation mechanism. This has been investigated theoretically in Ref. [23], and will be discussed in more detail in part III.

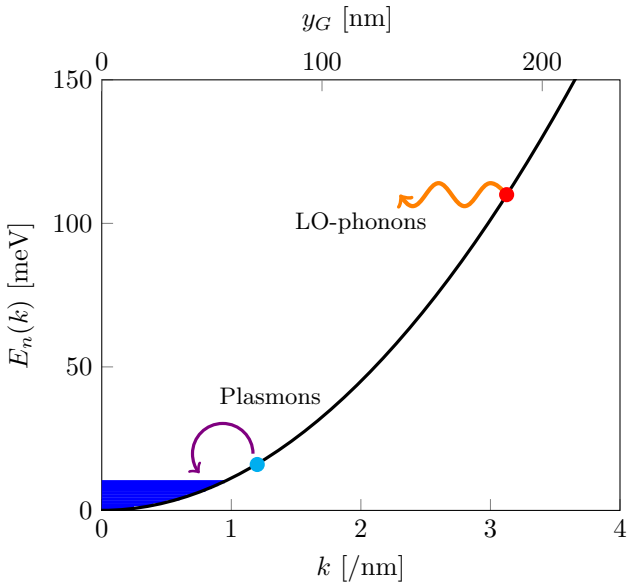

Figure 3.1: Adapted from Ref. [22]. Sketch of the relationship between energy, guide centre and wavenumber, along with the dominant relaxation method for the different realms. The Fermi sea is shown in blue.

3.3 Scattering theory

We can describe the path of electrons through an MZI in terms of scattering matrices, which describe the behaviour of electrons at the two beamsplitters. For DC sources, we would use the Landauer-Büttiker method to derive the scattering matrices and gain an equation for the current; however, with hot electrons we know the path they are taking, so can move directly to considering the scattering matrices for the paths followed. In this section, we will look at how these scattering matrices describe an MZI and the phases picked up in the system.

3.4 Scattering matrices of two beamsplitters

Beamsplitters in an electronic MZI have a dependence on the energy of the electrons, which affects both the phase and the transmission and reflection coefficients. The action of the two beamsplitters, $i = 1, 2$, can be described by

$$S_i = \begin{pmatrix} r_i & \tilde{t}_i \\ t_i & \tilde{r}_i \end{pmatrix}, \tag{3.6}$$

which with unitarity gives

$$S_i = \begin{pmatrix} \sqrt{R_i} e^{i\rho_i(k)} & \sqrt{T_i} e^{i\tilde{\theta}_i(k)} \\ \sqrt{T_i} e^{i\theta_i(k)} & \sqrt{R_i} e^{i\tilde{\rho}_i(k)} \end{pmatrix}, \tag{3.7}$$

with the reflection and transmission coefficients $|r_i|^2 + |t_i|^2 = R_i + T_i = 1$, and phases obeying

$$\theta_i(k) + \tilde{\theta}_i(k) - \rho_i(k) - \tilde{\rho}_i(k) = (2n+1)\pi \tag{3.8}$$

where $n = 0, \pm 1, \pm 2, ...$, which arises from unitarity, fulfilling the intuition of "what goes in, must come out", and the reversibility of quantum mechanics.

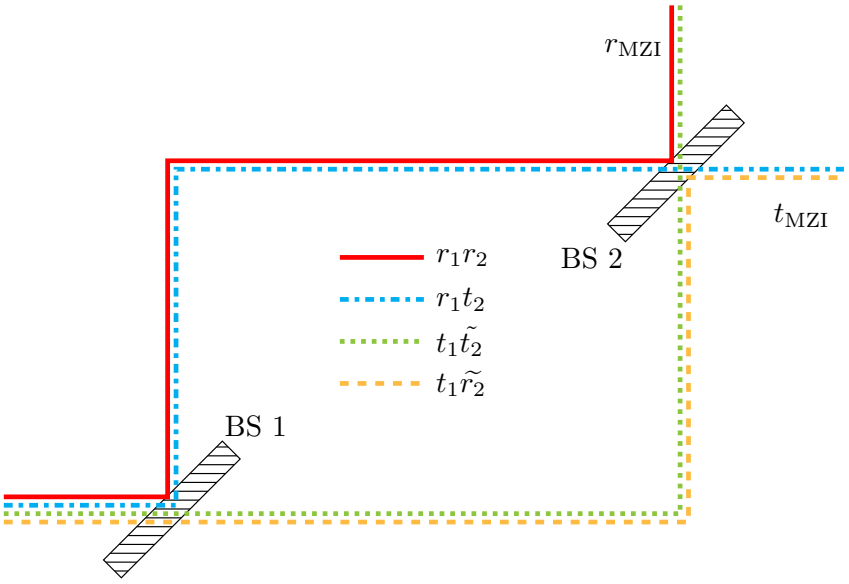

Figure 3.2: A sketch of the possible path options for an electron to follow. The solid red path shows a reflection at BS 1 and 2 and the green dotted line shows a transmission at BS 1 and BS 2, leading to both being detected in the upper channel. This combination is described by the equation for r_{MZI}. The yellow dashed and blue dot-dashed lines show a transmission at BS1 and reflection at BS2, and the vice versa, respectively, to be detected in the lower channel. This combination is described by the equation for t_{MZI}.

We are considering an MZI geometry with two beamsplitters with a phase accumulated in between. Considering input from just the upper arm, we can obtain an output wavefunction using

$$\begin{pmatrix} \Psi_U \\ \Psi_L \end{pmatrix} = S^{\mathrm{MZI}} \begin{pmatrix} \Psi_{\mathrm{in}} \\ 0 \end{pmatrix} = \begin{pmatrix} r^{\mathrm{MZI}} \Psi_{\mathrm{in}} \\ t^{\mathrm{MZI}} \Psi_{\mathrm{in}} \end{pmatrix} \tag{3.9}$$

where S^{MZI} is the total scattering matrix, and is given by

$$S^{\mathrm{MZI}} = \begin{pmatrix} r^{\mathrm{MZI}} & \tilde{t}^{\mathrm{MZI}} \\ t^{\mathrm{MZI}} & \tilde{r}^{\mathrm{MZI}} \end{pmatrix} = \begin{pmatrix} r_2 & \tilde{t}_2 \\ t_2 & \tilde{r}_2 \end{pmatrix} \begin{pmatrix} e^{i\phi_U(k)} & 0 \\ 0 & e^{i\phi_L(k)} \end{pmatrix} \begin{pmatrix} r_1 & \tilde{t}_1 \\ t_1 & \tilde{r}_1 \end{pmatrix}, \tag{3.10}$$

$$= \begin{pmatrix} r_1 r_2 e^{i\phi_U(k)} + t_1 \tilde{t}_2 e^{i\phi_L(k)} & \tilde{t}_1 r_2 e^{i\phi_U(k)} + \tilde{r}_1 \tilde{t}_2 e^{i\phi_L(k)} \\ r_1 t_2 e^{i\phi_U(k)} + t_1 \tilde{r}_2 e^{i\phi_L(k)} & \tilde{t}_1 t_2 e^{i\phi_U(k)} + \tilde{r}_1 \tilde{r}_2 e^{i\phi_L(k)} \end{pmatrix}. \tag{3.11}$$

where $\phi_{U/L}$ are the phase contributions from the dynamical and AB phase which we will calculate in Section 3.6. The paths corresponding to these are visualised in Fig. 3.2. Putting this into Eq. (3.9), and combining with Eq. (3.7) we obtain the important scattering amplitudes

$$\begin{aligned} r^{\mathrm{MZI}} &= r_1 r_2 e^{i\phi_U(k)} + t_1 \tilde{t}_2 e^{i\phi_L(k)}, \\ &= \sqrt{R_1 R_2} e^{i(\rho_1(k)+\rho_2(k)+\phi_U(k))} + \sqrt{T_1 T_2} e^{i(\theta_1(k)+\tilde{\theta}_2(k)+\phi_L(k))}, \end{aligned} \tag{3.12}$$

$$\begin{aligned} t^{\mathrm{MZI}} &= r_1 t_2 e^{i\phi_U(k)} + t_1 \tilde{r}_2 e^{i\phi_L(k)}, \\ &= \sqrt{R_1 T_2} e^{i(\rho_1(k)+\theta_2(k)+\phi_U(k))} + \sqrt{T_1 R_2} e^{i(\theta_1(k)+\tilde{\rho}_2(k)+\phi_L(k))}. \end{aligned} \tag{3.13}$$

This gives $r_k^{\mathrm{MZI}}\left(r_{k'}^{\mathrm{MZI}}\right)^*$ and $t_k^{\mathrm{MZI}}\left(t_{k'}^{\mathrm{MZI}}\right)^*$ as

$$r_k^{\mathrm{MZI}}\left(r_{k'}^{\mathrm{MZI}}\right)^* = \left(\sqrt{R_1^{(k)}R_2^{(k)}}e^{i[\rho_1(k)+\rho_2(k)+\phi_U(k)]} + \sqrt{T_1^{(k)}T_2^{(k)}}e^{i\left[\theta_1(k)+\tilde{\theta}_2(k)+\phi_L(k)\right]}\right) \times \left(\sqrt{R_1^{(k')}R_2^{(k')}}e^{-i[\rho_1(k')+\rho_2(k')+\phi_U(k')]} + \sqrt{T_1^{(k')}T_2^{(k')}}e^{-i\left[\theta_1(k')+\tilde{\theta}_2(k')+\phi_L(k')\right]}\right), \quad (3.14)$$

and

$$t_k^{\mathrm{MZI}}\left(t_{k'}^{\mathrm{MZI}}\right)^* = \left(\sqrt{R_1^{(k)}T_2^{(k)}}e^{i[\rho_1(k)+\theta_2(k)+\phi_U(k)]} + \sqrt{T_1^{(k)}R_2^{(k)}}e^{i[\theta_1(k)+\tilde{\rho}_2(k)+\phi_L(k)]}\right) \times \left(\sqrt{R_1^{(k')}T_2^{(k')}}e^{-i[\rho_1(k')+\theta_2(k')+\phi_U(k')]} + \sqrt{T_1^{(k')}R_2^{(k')}}e^{-i[\theta_1(k')+\tilde{\rho}_2(k')+\phi_L(k')]}\right), \quad (3.15)$$

which expand to

$$\begin{aligned} r_k^{\mathrm{MZI}}\left(r_{k'}^{\mathrm{MZI}}\right)^* &= \sqrt{R_1^{(k)}R_2^{(k)}}\sqrt{R_1^{(k')}R_2^{(k')}} \quad (3.16)\\ &\quad\times \exp\left[i\left\{\rho_1(k)+\rho_2(k)+\phi_U(k)-\rho_1(k')-\rho_2(k')-\phi_U(k')\right\}\right]\\ &+ \sqrt{R_1^{(k)}R_2^{(k)}}\sqrt{T_1^{(k')}T_2^{(k')}}\exp\left[i\left\{\rho_1(k)+\rho_2(k)+\phi_U(k)-\theta_1(k')-\tilde{\theta}_2(k')-\phi_U(k')\right\}\right]\\ &+ \sqrt{T_1^{(k)}T_2^{(k)}}\sqrt{R_1^{(k')}R_2^{(k')}}\exp\left[i\left\{\theta_1(k)+\tilde{\theta}_2(k)+\phi_L(k)-\rho_1(k')-\rho_2(k')-\phi_U(k')\right\}\right]\\ &+ \sqrt{T_1^{(k)}T_2^{(k)}}\sqrt{R_1^{(k')}R_2^{(k')}}\exp\left[i\left\{\theta_1(k)+\tilde{\theta}_2(k)+\phi_L(k)-\theta_1(k')-\tilde{\theta}_2(k')-\phi_L(k')\right\}\right] \end{aligned}$$

and

$$\begin{aligned} t_k^{\mathrm{MZI}}\left(t_{k'}^{\mathrm{MZI}}\right)^* &= \sqrt{R_1^{(k)}T_2^{(k)}}\sqrt{R_1^{(k')}T_2^{(k')}} \quad (3.17)\\ &\quad\times \exp\left[i\left\{\rho_1(k)+\theta_2(k)+\phi_U(k)-\rho_1(k')-\theta_2(k')-\phi_U(k')\right\}\right]\\ &+ \sqrt{R_1^{(k)}T_2^{(k)}}\sqrt{T_1^{(k')}R_2^{(k')}}\exp\left[i\left\{\rho_1(k)+\theta_2(k)+\phi_U(k)-\theta_1(k')-\tilde{\rho}_2(k')-\phi_L(k')\right\}\right]\\ &+ \sqrt{T_1^{(k)}R_2^{(k)}}\sqrt{R_1^{(k')}T_2^{(k')}}\exp\left[i\left\{\theta_1(k)+\tilde{\rho}_2(k)+\phi_L(k)-\rho_1(k')-\theta_2(k')-\phi_U(k')\right\}\right]\\ &+ \sqrt{T_1^{(k)}R_2^{(k)}}\sqrt{T_1^{(k')}R_2^{(k')}}\exp\left[i\left\{\theta_1(k)+\tilde{\rho}_2(k)+\phi_L(k)-\theta_1(k')-\tilde{\rho}_2(k')-\phi_L(k')\right\}\right] \end{aligned}$$

We can use these scattering amplitudes to determine the effect on electrons moving through the device, by considering the properties of the wavepackets themselves, as in Section 3.2. We can also use these to calculate the current in a hot-electron interferometer. In models of electrons from DC sources such as the one found in Ref. [57], the Landauer-Büttiker method [85] has been used to define the scattering matrices and the current in a system, however for these hot single-electrons, we instead multiply the Gaussian function which describes the wavepacket in terms of energy [38] by the scattering matrix, and integrate over energy to give the current in the system.

3.4.1 Hot-electron current

To find the current of hot electrons, we multiply the scattering matrix by a Gaussian distribution of the energy, and then integrate over energy, such that

$$I = ef\int_{-\infty}^{\infty} T(E)P(E)\,\mathrm{d}E, \quad (3.18)$$

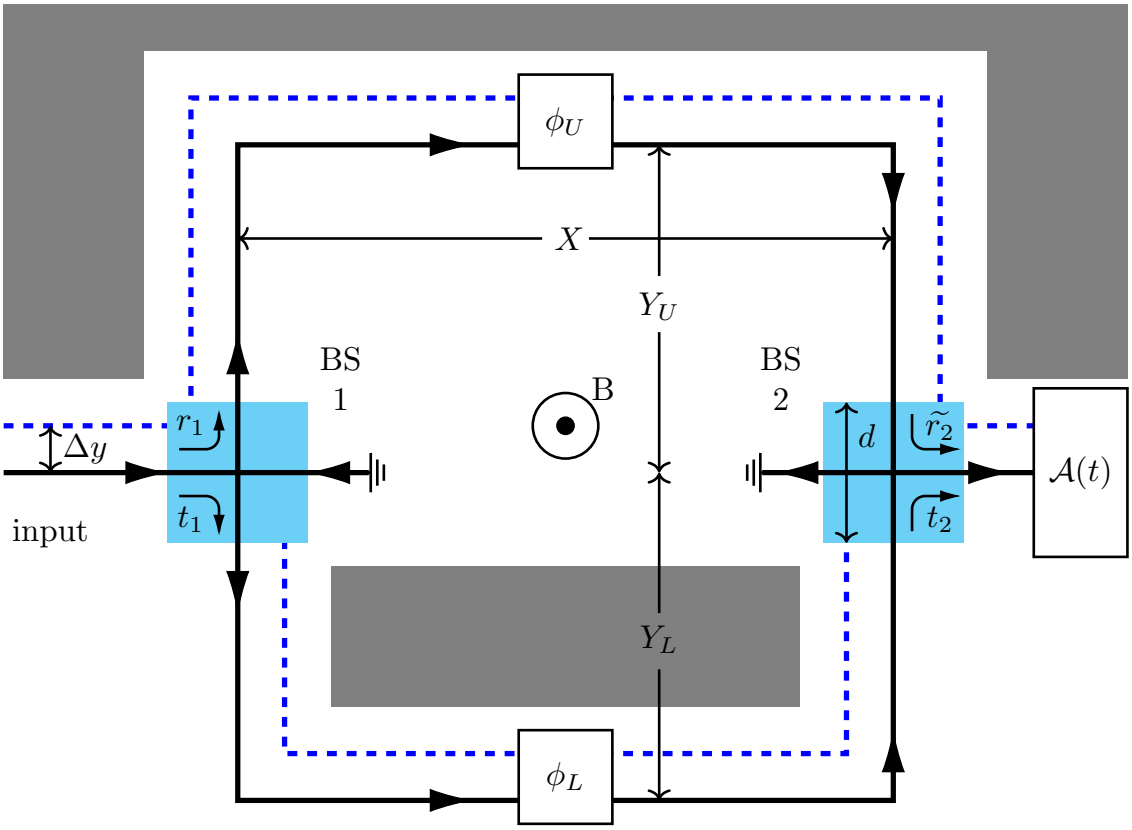

Figure 3.3: Schematic of a simple Mach-Zehnder Interferometer (MZI). The grey blocks show the edges of the interferometer, along which the edge states are formed for the electrons to travel along. When an electron is injected into the system with an energy $E = E_0$, the solid black path, known as the guide centre, y_G, is followed through the interferometer. Any small change in the energy leads to a shift, Δy, from the guide centre; the blue dashed line shows the path of an electron with energy $E = E_0 + \Delta E$ for example. The relationship between the change in energy and the guide centre shift is shown in Eq. (3.25). The dimensions of the MZI are labelled as X for the horizontal width of the black path, and Y_U and Y_L are the vertical contributions for the upper and lower black baths respectively. The blue boxes represent the (significantly exaggerated in size) QPC beamsplitters, with width d. The reflection and transmission parameters are shown in the beamsplitters as r_1, $\tilde{r_2}$, t_1 and t_2 for beamsplitter 1 and 2 respectively. For the purposes of our calculations, we initially ignore the contribution to the phases of the path lengths within these regions, as the beamsplitter contribution is considered separately to the geometric phases from the paths later on in this thesis. A magnetic field is applied to the system, and the electron travels through the interferometer as shown. The magnetic field induces an AB phase shift, which also depends on the area surrounded by the paths. The combination of the dynamical phase from the difference in path lengths and the AB phase for each arm is represented by $\phi_{U/L}$ in this figure. Electrons are detected at the ohmic contact, labelled $\mathcal{A}(t)$, which is also where the arrival time distributions (ATDs) are calculated.

where

$$T(E) = T_2R_1 + T_1R_2 + 2\sqrt{T_1T_2R_1R_2}\cos(\phi_{\text{tot}}), \tag{3.19}$$

with T and R as the transmission and reflection coefficients respectively, ϕ_{tot} is the total phase contribution from the AB, dynamical and beamsplitter phases, and

$$P(E) = \frac{1}{\sqrt{2\pi}\sigma_E} \exp\left[-\frac{1}{2}\frac{(E-E_0)^2}{\sigma_E^2}\right], \tag{3.20}$$

is a Gaussian distribution function. This expression is adapted from the expression describing the current in a dc source, which does not depend on the frequency of emission as this is not a factor for these sources. In Ref. [24] we can see that the gate voltages are tuned to pump one electron per cycle with a frequency of $f = 400\,\mu\text{s}^{-1}$.

To begin with in this chapter, we will assume energy independent beamsplitters, such that all phases due to the beamsplitter are 0, and we focus only on the dynamical and AB phases. We will also take the transmission and reflection coefficients to be $T_i = R_i = 1/2$. The energy dependence on the transmission and reflection coefficients of the beamsplitters will be incorporated later in this chapter, and the full beamsplitter phases are incorporated in Chapter 4. Before performing the integration, we first need to calculate the AB and dynamical phases for our interferometer.

3.5 Energy dependence of electron guide centres

Before we can start to calculate the different phases we first need to derive an equation relating the change in energy, ΔE, to the change in guide centre, Δy. Starting with Eq. (2.41),

$$E_n = \epsilon_n + \frac{1}{2}\hbar\Omega + \frac{1}{2}m_e^*\omega_y^2\left(\frac{\Omega}{\omega_c}\right)^2 y_G^2 \tag{3.21}$$

where y_G is the guide centre from Eq. (2.28),

$$y_G = \frac{\omega_c^2}{\Omega^2}\frac{\hbar k}{eB}. \tag{3.22}$$

If an electron is emitted at exactly the initial energy, E_0, then $y = y_0$ and the guide centre is,

$$y_0 = \frac{\omega_c^2}{\Omega^2}\frac{\hbar k_0}{eB}. \tag{3.23}$$

We know that a change in energy relates directly to a displacement from the guide centre and change in electron wavenumber, so we can write

$$y_0 + \Delta y = \frac{\omega_c^2}{\Omega^2}\frac{\hbar(k_0+\Delta k)}{eB}. \tag{3.24}$$

Inputting these definitions into Eq. (3.21) for $E_0 + \Delta E$ gives,

$$E_0 + \Delta E \approx \epsilon_0 + \frac{1}{2}\hbar\Omega + \frac{1}{2}m_e^*\omega_y^2\left(\frac{\Omega}{\omega_c}\right)^2 y_0^2 + m_e^*\omega_y^2\left(\frac{\Omega}{\omega_c}\right)^2 y_0\Delta y \tag{3.25}$$

Here, Eq. (3.25) has been linearised, elimating the Δy^2 term, as it is the square of a very small change and so is negligible (see Appendix B). This is the original equation for energy, with an added term at the end to include the effect of Δy. We

can combine this with the cyclotron frequency, $\omega_c = eB/m_e^*$, and write it in terms of the wavenumber, $k = k_0 + \Delta k$ as well, i.e.

$$\begin{aligned}\Delta E =& m_e^* \omega_y^2 \frac{\Omega^2}{\omega_c^2} y_0 \Delta y \\ =& \frac{\omega_y^2}{\Omega^2} \frac{\hbar^2}{m_e^*} k_0 \Delta k. \end{aligned} \tag{3.26}$$

We can also now introduce the electron velocity, v, as calculated in Chapter 2 which is described by [40, 37]

$$v = \frac{1}{\hbar}\frac{\mathrm{d}E}{\mathrm{d}k} = \frac{1}{\hbar}\frac{\Delta E}{\Delta k} = \frac{\omega_y^2}{\Omega^2}\frac{\hbar k}{m_e^*}. \tag{3.27}$$

We assume throughout this thesis that the Gaussian is small such that as the energy is varied across it's width, the velocity does not change significantly and can therefore be assumed to be constant, and is evaluated at E_0, to give

$$v_0 = \frac{\omega_y^2}{\Omega^2}\frac{\hbar}{m_e^*} k_0. \tag{3.28}$$

From Eq. (3.27) we can see that for small changes in E, we have

$$\Delta E = \hbar v_0 \Delta k, \tag{3.29}$$

which, in combination with the equation for wavenumber at small changes in E and therefore y,

$$\Delta k = \frac{\Omega^2}{\omega_c}\frac{m_e^*}{\hbar}\Delta y \tag{3.30}$$

gives an equation for ΔE in terms of Δy,

$$\Delta E = v_0 m_e^* \frac{\Omega^2}{\omega_c}\Delta y; \qquad \Rightarrow \Delta y = \frac{\omega_c}{\Omega^2}\frac{\Delta E}{m_e^* v_0}. \tag{3.31}$$

These relations will be used in the coming sections to establish the effects of these small changes in energy, and therefore guide centre, on the different phases of an electron.

3.5.1 Deviations of the guide centre

The deviation of the guide centre position discussed above, Δy, changes the geometry of the interferometer as a whole. This will affect the phases discussed in the next sections, so here we will determine exactly what changes we encounter in guide centre due to the small change in energy.

In Fig. 3.3, an electron emitted at exactly energy E_0 will follow the central path, shown by the black solid line and, as discussed above, a small deviation from this energy will cause the electron to travel either closer to the edge state, in the case of an increase in energy, or further away if the energy is decreased. The interferometer in Fig. 3.3 shows the path for an increase in energy as a blue dashed line, however all of the equations are valid for any Δy.

Although these calculations can be performed for any shaped geometry, for ease of calculations we have chosen to use a rectangular interferometer. If we follow the solid black line in the diagram, we have vertical lengths Y_U and Y_L and horizontal lengths X_U and X_L where $X_U = X_L = X$, but they are labelled separately for clarity in the transformations. In this, and all following notation in this chapter, U refers to the contribution from the upper path of the interferometer, and L to the lower. This means that the change in path length depends only on the changes in the length of vertical lengths, leaving the horizontal length unperturbed. In the case of a small change in energy, we assume that the electron follows the black line inside the blue box, representing the beamsplitter, and the blue dashed line everywhere else. This is because, as discussed in section 3.7, we will treat the beamsplitters separately. We can also take away the size of the beamsplitters, d, from the vertical sides for the same reason. The dimensions then have the following transformations

$$Y_U \rightarrow Y_U + \Delta y - d/2, \tag{3.32a}$$
$$Y_L \rightarrow Y_L - \Delta y - d/2, \tag{3.32b}$$
$$X_U \rightarrow X + 2\Delta y, \tag{3.32c}$$
$$X_L \rightarrow X - 2\Delta y. \tag{3.32d}$$

Now that we have the relations between energy, wavenumber and path coordinate, y, as well as their dependence on a change in energy, we can use these qualities to investigate the effect of these energy changes on the phases picked up by an electron in a MZI.

3.6 Dynamical and Aharonov-Bohm phases

There are two contributions to the phase shift from the changing geometry of the system: the AB phase and the dynamical phase. Here we derive the effect on the detected current and therefore visibility of small shifts in energy on the contributions of these two phases.

3.6.1 Dynamical Phase

The dynamical phase comes from the difference in length of the upper and lower paths in the interferometer. If the path lengths are the same there will be no phase shift from this, however this is not always the case.

The phase, ϕ_{dyn} is calculated by multiplying the path length difference by wavenumber k, i.e. $\phi_{\text{dyn}} = k(x_U - x_L)$ where x_U is the upper path length and x_L is the lower path length. Taking into account the small change in guide centre as shown in Eq. 3.32, these path lengths are then

$$x_U = 2Y_U + X + 4\Delta y - d, , \tag{3.33a}$$
$$x_L = 2Y_L + X - 4\Delta y - d, \tag{3.33b}$$
$$x_U - x_L = 2(Y_U - Y_L) + 8\Delta y. \tag{3.33c}$$

From this, we can define the central path difference, $l_0 = 2(Y_U - Y_L)$. If we now multiply Eq. (3.33c) by the wavenumber $k = k_0 + \Delta k$, we get

$$\phi_{\text{dyn}} = (k_0 + \Delta k)(l_0 + 8\Delta y), \tag{3.34}$$
$$= l_0 k_0 + 8\Delta y k_0 + l_0 \Delta k + 8\Delta y \Delta k. \tag{3.35}$$

We can now write this in terms of ΔE, via Δk, using Eq. (3.24) and Eq. (3.29) to get

$$\begin{aligned}\phi_{\text{dyn}} &= l_0 k_0 + 8\frac{\omega_c}{\Omega^2}\frac{\hbar \Delta k}{m_e^*}k_0 + l_0 \Delta k + 8\frac{\omega_c}{\Omega^2}\frac{\hbar \Delta k^2}{m_e^*}, \\ &= l_0 k_0 + 8\frac{\omega_c}{\Omega^2}\frac{\Delta E k_0}{m_e^* v_0} + \frac{l_0 \Delta E}{\hbar v_0} + 8\frac{\omega_c}{\Omega^2}\frac{\Delta E^2}{\hbar m_e^* v_0^2}.\end{aligned} \tag{3.36}$$

We also need k_0 in terms of an energy E_0, which is given by

$$\begin{aligned}E_0 &= \frac{1}{2}\frac{\hbar^2}{m_e^*}\frac{\omega_y^2}{\Omega^2}k_0^2, \\ &= \frac{1}{2}\hbar v_0 k_0, \\ \Rightarrow k_0 &= \frac{2E_0}{\hbar v_0}.\end{aligned} \tag{3.37}$$

So Eq. (3.36) becomes

$$\phi_{\text{dyn}} = \frac{2l_0 E_0}{\hbar v_0} + 16\frac{\omega_c^2}{\Omega^2}\frac{E_0 \Delta E}{\hbar \omega_c m_e^* v_0^2} + \frac{l_0 \Delta E}{\hbar v_0} + 8\frac{\omega_c^2}{\Omega^2}\frac{\Delta E^2}{\hbar \omega_c m_e^* v_0^2}, \tag{3.38}$$

which is the dynamical phase at an energy $E = E_0 + \Delta E$. This will combine with the AB phase to give the total phase from the geometry of the system, as calculated in the next section.

3.6.2 Aharonov-Bohm Phase

The magnetic flux through the MZI causes a phase shift called the AB phase [34]. This phase depends on the area surrounded by the paths of the arms of the interferometer and the magnetic field strength. The AB phase [34] for the geometry in Fig. 3.3 is ($e > 0$, $B > 0$)

$$\phi_{\text{AB}}^{(tot)} = \phi_{\text{AB}}^{(U)} - \phi_{\text{AB}}^{(L)} = \frac{e}{\hbar}BX(Y_U + Y_L) = \frac{e}{\hbar}BA, \tag{3.39}$$

where A is the area of the interferometer loop. Note that the sign of this quantity is critically important here — see Appendix A for the derivation. By calculating the area A using the blue dashed line in Fig. 3.3 outside the beamsplitters and the black solid line inside them, as discussed in section 3.5.1, we obtain,

$$\begin{aligned}A &= (X + 2\Delta y)(Y_U + \Delta y) + (X - 2\Delta y)(Y_L - \Delta y), \\ &= A_0 + l_0 \Delta y + 4(\Delta y)^2.\end{aligned} \tag{3.40}$$

Here we have introduced the area enclosed by the central (E_0) path $A_0 = X(Y_U + Y_L)$. Combining Eq. (3.39) and Eq. (3.40) gives an equation for ϕ_{AB} of

$$\phi_{\mathrm{AB}} = \frac{m_e^* \omega_c}{\hbar} \left[A_0 + l_0 \Delta y + 4(\Delta y)^2 \right], \tag{3.41}$$

as the cyclotron frequency, $\omega_c = eB/m_e^*$.

We can put Eq. (3.41) in terms of ΔE by using Eq. (3.31), to give

$$\begin{aligned} \phi_{\mathrm{AB}} =& \frac{m_e^* \omega_c}{\hbar} \left[4 \left(\frac{\Delta E \omega_c}{v_0 m_e^* \Omega^2} \right)^2 + \frac{\Delta E \omega_c}{v_0 m_e^* \Omega^2} l_0 + A_0 \right], \\ =& \frac{4\Delta E^2}{m_e^* v_0^2 \hbar \omega_c} \frac{\omega_c^4}{\Omega^4} + \frac{l_0}{\hbar v_0} \frac{\omega_c^2}{\Omega^2} \Delta E + \frac{m_e^* \omega_c}{\hbar} A_0. \end{aligned} \tag{3.42}$$

This is the AB phase for an electron with an energy $E = E_0 + \Delta E$. Combined with the dynamical phase for the same energy, this gives the total phase from the geometry of the system for an electron with some uncertainty in the injection energy, ΔE. We can now use these phases to calculate the current in an electronic MZI.

3.6.3 Current with a small energy perturbation

We can calculate the current in an electronic MZI using equation Eq. (3.18), which includes the total phase from the geometry for the system and from the beamsplitter. In this section, we will assume a 50:50 beamsplitter which therefore has no phase contribution. The contribution of the beamsplitter will be taken into account in the next section. We therefore only need the sum of the AB and dynamical phases for this section, which is

$$\begin{aligned} \phi_{\mathrm{tot}} = \phi_{\mathrm{AB}} + \phi_{\mathrm{dyn}} =& \frac{4\Delta E^2}{m_e^* v_0^2 \hbar \omega_c} \left(\frac{\omega_c}{\Omega} \right)^4 + \frac{\Delta E l_0}{\hbar v_0} \left(\frac{\omega_c}{\Omega} \right)^2 + \frac{m_e^* \omega_c}{\hbar} A_0 \\ &+ \frac{8\Delta E^2}{m_e^* v_0^2 \hbar \omega_c} \left(\frac{\omega_c}{\Omega} \right)^2 + \frac{16 E_0 \Delta E}{m_e^* v^2 \hbar \omega_c} \left(\frac{\omega_c}{\Omega} \right)^2 + \frac{l_0 \Delta E}{\hbar v_0} + \frac{2 l_0 E_0}{\hbar v_0}. \end{aligned} \tag{3.43}$$

This can be written in three parts, one of which depends on ΔE^2, one on ΔE and one which is independent of ΔE. The coefficients of each can be written as a_2, a_1 and a_0 respectively, giving

$$\phi_{\mathrm{tot}} = a_2 \Delta E^2 + a_1 \Delta E + a_0, \tag{3.44}$$

where

$$a_2 = \frac{4}{m_e^* v_0^2 \hbar \omega_c} \left(\frac{\omega_c}{\Omega} \right)^4 + \frac{8}{m_e^* v_0^2 \hbar \omega_c} \left(\frac{\omega_c}{\Omega} \right)^2, \tag{3.45a}$$

$$a_1 = \frac{16 E_0}{m_e^* v_0^2 \hbar \omega_c} \left(\frac{\omega_c}{\Omega} \right)^2 + \frac{l_0}{\hbar v_0} \left(\frac{\omega_c}{\Omega} \right)^2 + \frac{l_0}{\hbar v_0}, \tag{3.45b}$$

$$a_0 = \frac{m_e^* \omega_c}{\hbar} A_0 + \frac{2 l_0 E_0}{\hbar v_0}. \tag{3.45c}$$

Now we can combine Eq. (3.18), Eq. (3.19), Eq. (3.20) and Eq. (3.44), and use $\Delta E = E - E_0$ to give

$$I = ef \int_{\infty}^{\infty} \left\{ \frac{(T_2R_1 + T_1R_2)}{\sqrt{2\pi}\sigma_E} \exp\left[-\frac{\Delta E^2}{2\sigma_E^2} \right] + \frac{2\sqrt{T_1T_2R_1R_2}}{\sqrt{2\pi}\sigma_E} \cos\big(a_2\Delta E^2 + a_1\Delta E + a_0\big) \exp\left[-\frac{\Delta E^2}{2\sigma_E^2} \right] \right\} \mathrm{d}E. \quad (3.46)$$

This we can write in the form of an exponential to make integration possible. This we can do as we have the identity $2\cos(x) = [\exp(ix) + \exp(-ix)]$. Once we have it in terms of the exponentials only, we see that Eq. (3.46) becomes a Gaussian integral,

$$I = ef \left\{ (T_2R_1 + T_1R_2) + \frac{\exp[ia_0]}{\sqrt{2\pi}\sigma_E} \sqrt{T_1T_2R_1R_2} \times \left(\int_{-\infty}^{\infty} \left\{ \exp\left[-\left(\frac{1}{2\sigma_E^2} - a_2 i \right) \Delta E^2 + a_1 i \Delta E \right] + \text{c.c.} \right\} \mathrm{d}E \right) \right\}, \quad (3.47)$$

where c.c. is the complex conjugate. Fortunately, Gaussian integrals have standard results, so this integral can be solved as

$$\int_{-\infty}^{\infty} \exp\big[-fx^2 + gx\big] \, \mathrm{d}x = \frac{\sqrt{\pi}}{\sqrt{f}} \exp\left[\frac{g^2}{4f} \right], \quad (3.48)$$

to give

$$I = ef \left\{ (T_2R_1 + T_1R_2) + \sqrt{T_1T_2R_1R_2} \left(\frac{\exp[ia_0]}{\sqrt{1 - 2ia_2\sigma_E^2}} \exp\left[-\frac{1}{2} \frac{a_1^2\sigma_E^2}{(1 - 2ia_2\sigma_E^2)} \right] + \text{c.c.} \right) \right\}. \quad (3.49)$$

This is an equation for current with the effects of phase averaging included. At the minute, there are still imaginary parts to the equation. The equation for current should be real, so we need to separate the equation out into its real and imaginary parts, to see if we can manipulate them such that the final equation involves a real cosine term instead of imaginary exponentials. This results in the following expression,

$$I = ef \left\{ (T_2R_1 + T_1R_2) + \sqrt{\frac{T_1T_2R_1R_2}{\sqrt{1 + F^2}}} \times \left(\exp[i(a_0 + \theta)] \exp\left[\frac{-a_1^2\sigma_E^2(1 + iF)}{2(1 + F^2)} \right] + \text{c.c.} \right) \right\}, \quad (3.50)$$

where $F = 2a_2\sigma_E^2$. This has introduced a new phase shift, θ, which we find to be $\tan 2\theta = F$, (see Appendix C for details). The aim here has been to write Eq. (3.50) in such a way that the imaginary terms are removed. To do this, we separate the terms in the exponential such that the real and imaginary terms are written separately. This can then be written in terms of two exponentials of the form $e^{i\phi} + e^{-i\phi}$. We can then remove the imaginary terms by moving from the

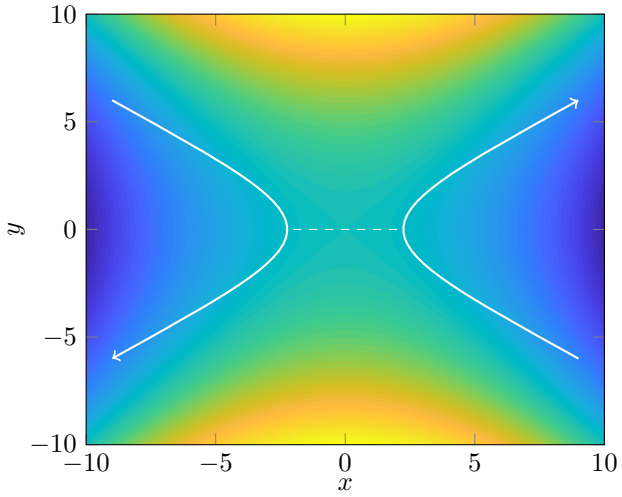

Figure 3.4: The potential for the Fertig-Halperin saddle-point model of a quantum point contact beamsplitter. Depending on the width of the beamsplitter and the magnitude of the central potential, electrons approaching from the left will either follow round to the bottom and leave on the left, which is a reflection, or will move through the middle and exit on the right, which is transmission. The white arrows are sketches of potential paths for an incoming electron. It should be noted that the x and y here are arbitrary coordinates, and are not the same as the x and y in the wavefunction, which are time dependent such that the transport is always in the x-direction.

exponential version of the equation to the cosine version, essentially reversing the step we took between Eq. (3.46) and Eq. (3.47) now that the integration has been performed. This gives a full equation for the current of an electron of

$$I = ef\left\{(T_2R_1 + T_1R_2) + 2\sqrt{\frac{T_1T_2R_1R_2}{\sqrt{1+F^2}}} \times \exp\left[\frac{-a_1^2\sigma_E^2}{2(1+F^2)}\right]\cos\left[a_0 + \theta - \frac{a_1^2\sigma_E^2F}{2(1+F^2)}\right]\right\} \quad (3.51)$$

taking into account the AB phase, the dynamical phase, and assuming beamsplitters which are not dependent on the same energy spreading. The cosine term describes the oscillations in the current, which are very fast in this system. We will often use the exponential term multiplied by the square root of the transmission and reflection coefficients to describe the visibility, as this is the dominant term in the equation. In the next section, we will incorporate the energy dependence in the beamsplitters into the model by introducing energy dependent terms for the transmission and reflection coefficients, and compare the results to the ideal case of perfect 50:50 beamsplitters.

3.7 Energy dependent transmission and reflection coefficients

Previously we have assumed energy independent beamsplitters, however in a realistic system the beamsplitters would have an energy dependence which we will take into account here. We will use the Fertig-Halperin saddle-point potential to describe the

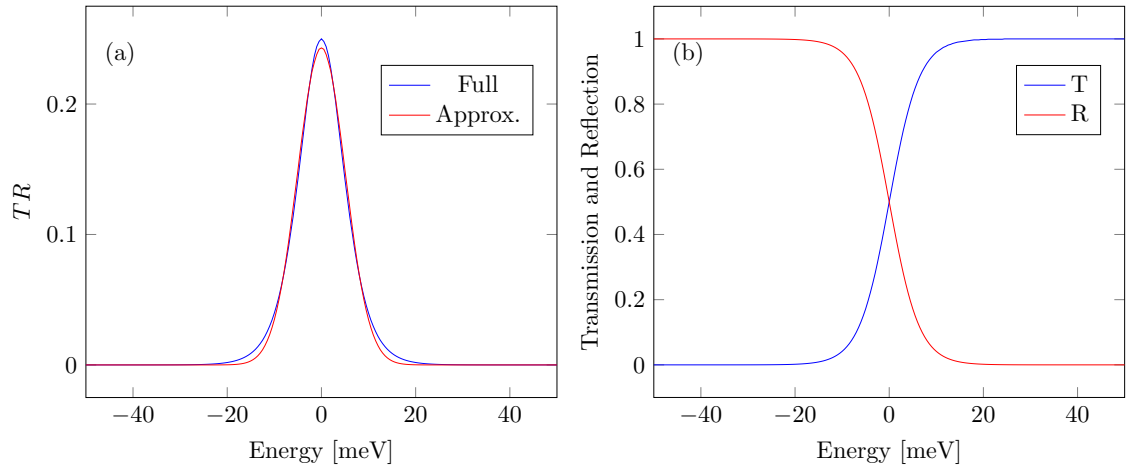

Figure 3.5: Part (a) Shows a comparison of the approximation in Eq. (3.55). The blue line is the full equation including the cosh term, and the red line is the gaussian approximation. Part (b) shows a plot of the energy dependent transmission and reflection coefficients. Both parts use a value of $E_{\text{sad}} = 10$ meV.

energy dependent beamsplitters, which gives a transmission probability of [86]

$$T = \frac{1}{1 + \exp(-\pi\epsilon)}, \tag{3.52}$$

where $\epsilon = (\Delta E + E_0 - V_0)/E_{\text{sad}}$. Here, $E_{\text{sad}} \approx (U_x U_y)^{1/2}/m_e^* \omega_c$, is the width of the beamsplitter and V_0 is the central energy of the beamsplitter, which can be set experimentally. A visualisation of this potential can be seen in Fig. 3.4.

We can then calculate the product of the transmission and reflection probabilities, as this combination of TR is the one used for our paths in Eq. (3.51),

$$TR = \frac{1}{1 + \exp(-\pi\epsilon)} \left[1 - \frac{1}{1 + \exp(-\pi\epsilon)}\right] \tag{3.53}$$

$$= \frac{1}{2} \left[\frac{1}{\cosh(\pi\epsilon) + 1}\right]. \tag{3.54}$$

This can be approximated as a Gaussian,

$$TR = \frac{1}{2} \left[\frac{1}{\cosh(\pi\epsilon) + 1}\right] \approx T_{\max} \exp\left[\frac{-\epsilon^2}{2\sigma_{TR}^2}\right] \tag{3.55}$$

where $T_{\max}$ is the amplitude, and σ_{TR} is the width of the Gaussian. We can determine the value for σ_{TR} using the Trust-Region algorithm to approximate the function in the form of a Gaussian. More on the Trust-Region algorithm can be found in Ref. [87]. We also rewrite ϵ as $\epsilon = \Delta E + x$, where $x = E_0 - V_0$ is the mid-point of the Gaussian, which represents the QPC acting as a 50:50 beamsplitter. This approximation can be seen in Fig. 3.5.

Assuming identical beamsplitters, the equation for current becomes

$$I = ef \int_{-\infty}^{\infty} \mathrm{d}\Delta E \; 2T(\Delta E)R(\Delta E)(1 + \cos[\phi(\Delta E)])P(\Delta E) \tag{3.56}$$

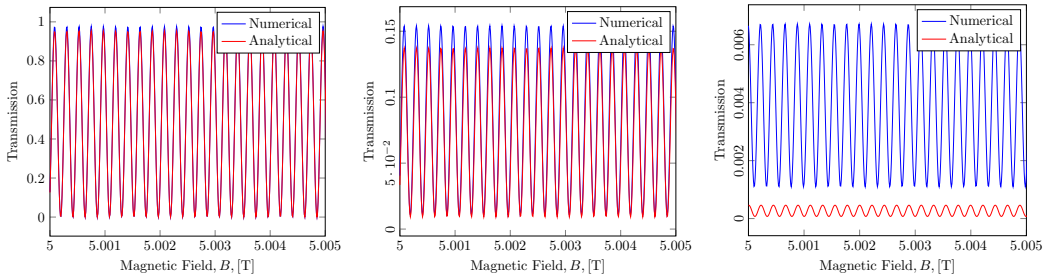

Figure 3.6: A comparison of the analytical expression in Eq. (3.59) for the total transmission as a function of magnetic field with that obtained from numerical integration of Eq. (3.57). From left to right the centre of the electron wave packet was $E_0 = 100, 90, 120$meV as compared with the centre of the saddle $V_0 = 100$meV. Other parameters were $\sigma_E = 1$meV, $\sigma_{TR} \approx \frac{\sqrt{2/\pi}}{3^{1/3}} E_{\text{sad}}$, which comes from the Gaussian fit to the saddle point potential transmission width, and $E_{\text{sad}} = 10$meV which is a beamsplitter width realistic to experiments.

and inserting the equation for the transmission and reflection product above we get

$$I = ef \frac{2T_{\max}}{\sqrt{2\pi}\sigma_E} \int_{-\infty}^{\infty} \mathrm{d}\Delta E \ \exp\left[\frac{-(\Delta E + x)^2}{2\sigma_{TR}^2}\right] \exp\left[-\frac{1}{2}\frac{\Delta E^2}{\sigma_E^2}\right] (1 + \cos\left[\phi(\Delta E)\right]) \,. \tag{3.57}$$

In order to facilitate the integration here we can combine the exponentials and write like terms together, such that it is more obviously a Gaussian integration,

$$\begin{aligned} I = ef \frac{2T_{\max}}{\sqrt{2\pi}\sigma_E} \exp\left[-\frac{x^2}{2\sigma_{TR}^2}\right] \\ \times \left\{ \int_{-\infty}^{\infty} \exp\left[-\left(\frac{1}{2\sigma_{TR}^2} + \frac{1}{2\sigma_E^2}\right)\Delta E^2 + \left(\frac{-x}{\sigma_{TR}^2}\right)\Delta E\right] \mathrm{d}\Delta E \right. \\ \left. + \int_{-\infty}^{\infty} \exp\left[-\left(\frac{1}{2\sigma_{TR}^2} + \frac{1}{2\sigma_E^2}\right)\Delta E^2 + \left(\frac{-x}{\sigma_{TR}^2}\right)\Delta E\right] \cos[\phi(\Delta E)] \, \mathrm{d}\Delta E \right\} . \end{aligned} \tag{3.58}$$

These are then integrated using the identity in Eq. (3.48) to give the full equation for current including the energy dependent beamsplitters,

$$I = ef \frac{\sigma'_E}{2\sigma_E} \exp\left[-\frac{1}{2}\left(\frac{\sigma_E'^2}{\sigma_E^2}\right)\frac{x^2}{\sigma_{TR}^2}\right] \left\{1 + \exp\left[-\frac{1}{2}\sigma_E'^2\phi_1^2\right] \cos\left[\phi_0 - \frac{x\sigma_E'^2\phi_1}{\sigma_{TR}^2}\right]\right\}, \tag{3.59}$$

which is written in terms of the rescaled energy width

$$\sigma_E'^2 = \frac{\sigma_E^2}{1 + \frac{\sigma_E^2}{\sigma_{TR}^2}}. \tag{3.60}$$

Fig. 3.6 shows the total transmission as a function of magnetic field for three different values of E_0. This shows that away from the tails of the Gaussian where the fringes are strong, the analytical expression agrees well with numerical integration of Eq. (3.57), which uses the non-approximated expressions.

3.8 Results

Equation (3.59) can be compared with that obtained with the energy-independent beamsplitters, Eq. (3.51) which in the case where the beamsplitters are identical

becomes

$$I = 2efTR\left\{1 + e^{-\frac{1}{2}\phi_1^2\sigma_E^2}\cos\phi_0\right\}. \tag{3.61}$$

where ϕ_1 contains all terms depending on energy in Eq. (3.51).

Relative to this expression, the energy-dependence of the beamsplitters brings three effects. First of all, we obtain an overall modulation of the transmission that simply results from our concrete model of the T and R coefficients. In the case where the wavepacket is injected such that $x = 0$, we obtain the forefactor $2TR = \sigma'_E/2\sigma_E$ relative to the previous expression. In the limit $\sigma_E \ll \sigma_{TR}$, we have $\sigma'_E \approx \sigma_E$, and this forefactor becomes $1/2$, consistent with 50:50 beamsplitters. In the opposite limit, $\sigma_E \gg \sigma_{TR}$, we have $\sigma'_E \approx \sigma_{TR}$ and the forefactor becomes $\sigma_{TR}/(2\sigma_E)$, which gives a reduction of the overall current. This is to be expected, as if the wavepacket is much larger than the beamsplitter, different parts of the wavepacket are "seeing" different transmission and reflection coefficients to other parts. In the case where we assume no energy dependence in the beamsplitter, we assume that an electron experiences each equally, whereas when different parts of the wavepacket experience different coefficients, they do not interfere perfectly, leading to a loss in visibility of the current. In the case where the beamsplitter is much larger than the wavepacket, the electron sees only the centre of the beamsplitter and so the whole wavepacket experiences essentially the same transmission and reflection coefficients, which is the same as the case for the 50:50 beamsplitter.

We also obtain a shift of the AB phase oscillations, however this is not significant to the phase averaging results as the shift does not affect that amplitude of the oscillations, and therefore the visibility. Finally, by finding the maximum and minimum current, we can use the equation for visibility in Eq. (1.1), we obtain a modified visibility

$$\nu = \frac{2\sqrt{R_1R_2T_1T_2}}{R_1R_2 + T_1T_2}\mathcal{D} \text{ or } \nu = \frac{2\sqrt{R_1R_2T_1T_2}}{R_1T_2 + T_1R_2}\mathcal{D}, \tag{3.62}$$

depending on the detection channel being considered, where $\mathcal{D}$ is the phase averaging contribution, given by

$$\mathcal{D} = \exp\left\{-\frac{1}{2}\left(\frac{l_0 + l_{\text{off}}}{\Sigma'_l}\right)^2\right\}. \tag{3.63}$$

Here we can see that the visibility can be maximised to 1 for symmetric beamsplitters where $T_1 = T_2 = R_1 = R_2 = 1/2$. This shows the power of the analytic solutions, as we can see, without the use of time consuming numerics, that there is a value of l_off that will maximise this equation. This phase averaging contribution is the same as that without the inclusion of the beamsplitters, but with the rescaled width

$$\Sigma'_l = \frac{\sigma_E}{\sigma'_E}\Sigma = \frac{\Omega^2}{\Omega^2 + \omega_c^2}\frac{\hbar v_0}{\sigma'_E}, \tag{3.64}$$

and the offset,

$$-l_{\text{off}} = \frac{8v_0\Omega^2}{\omega_c^2 + \Omega^2}\frac{\omega_c}{\omega_y^2}. \tag{3.65}$$

We can see that in the case where the beamsplitters are assumed to be 50:50, $\nu \to \mathcal{D}$. Physically, this is because for a 50:50 beamsplitter, there is no impact on the phase

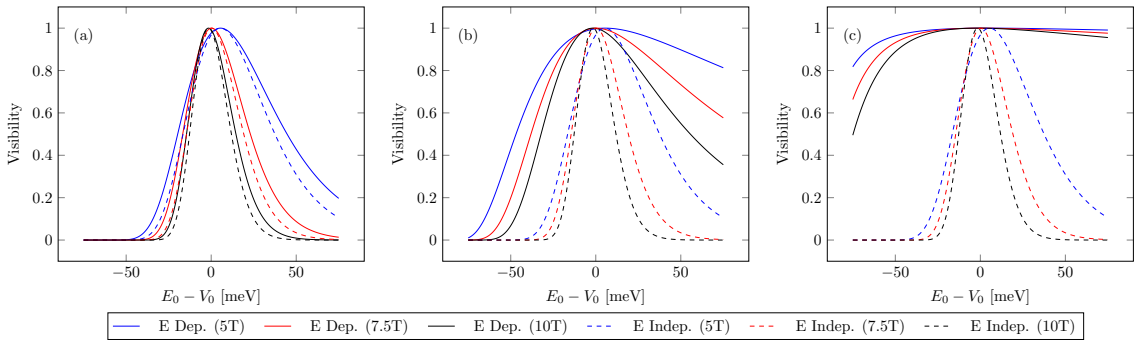

Figure 3.7: Comparison of visibilities for different values of σ_E/σ_{TR}. Here, $\sigma_E = 1$ meV, and in a) $\sigma_{TR} \approx \frac{\sqrt{2/\pi}}{3^{1/3}} E_{\text{sad}}$ which is approximately 2.7meV when $E_{\text{sad}} = 10$meV, b) $\sigma_{TR} = \sigma_E$ and c) $\sigma_E = 0.2$ meV. The visibility is shown for magnetic fields of 5, 7.5 and 10 Tesla, over a range of $E_0 - V_0$.

from the transmission and reflection coordinates themselves, because the wavepacket splits and recombines evenly at both beamsplitters.

We also see that the size of the path offset l_{off} depends on velocity. For cold electrons, around $E_0 = 5\,\text{meV}$, we find $l_{\text{offset}} \sim 100\,\text{nm}$. This value is small compared with typical interferometers, as well as being similar in magnitude to the single-particle coherence length for cold electrons [66], which explains why in previous models this effect has not been considered. In contrast, for hot electrons the value of l_{off} becomes closer to $1\,\mu\text{m}$. This is large in comparison with the size of the interferometers, and clearly such a significant offset will make a difference to MZI design, with the geometry of experiments needing to be tailored to a specific injection energy to ensure optimal visibility.

If we consider the case where $\sigma_E \ll \sigma_{TR}$, we have $\sigma'_E \approx \sigma_E$, and therefore $\Sigma'_l \approx \Sigma_l$. In this case, the width of the wave packet is the deciding factor for the visibility. In the opposite limit, $\sigma_E \gg \sigma_{TR}$, we have $\sigma'_E \approx \sigma_{TR}$ and $\Sigma'_l \approx \Sigma_l \sigma_E/\sigma_{TR}$ and the visibility is dominated by the narrow QPC resonance. A comparison of the visibility with and without beamsplitter energy-dependence can be found in Fig. 3.7. The maximum visibility obtained in all cases is $\nu = 1$.

The plots shown in Fig. 3.7 demonstrate the importance of the inclusion of the energy dependence of the beamsplitters. When considering beamsplitters with a width of around 10 meV, the the energy independent case is a fairly good representation of reality. However, as the difference between the size of the wavepacket and the size of the beamsplitter shrinks, the energy dependence of the beamsplitters becomes more important and the beamsplitters can no longer be approximated as energy independent devices. These equations for the visibility of the system derived in the previous section can be used to investigate the regions of energy for which the visibility is maximised. We will now explore how the visibility varies with magnetic field, energy, path length offset and beamsplitter width.

The optimum injection energy to obtain a maximised visibility can be seen in Fig. 3.8. We introduce here a new variable E_{peak}, which is the energy for which the path length difference has been optimised. If the $E_{\text{peak}} = 100\,\text{meV}$, then when the energy $E_0 = 100\,\text{meV}$, the visibility is maximised. We can do this by using this energy as the input to calculate the electron velocity, and therefore l_{off}. The reason for introducing this is that the physical systems can then be built with a path length

correct for a specific energy, and then the input energy, which is easier to change than the somewhat permanent MZI size, can be altered to match E_{peak}. Parts (a), (b) and (c) show the visibilities for $E_{\text{peak}} = 90, 100$ and 110 meV respectively. We can see from these plots that the width of potential injection energies doesn't change for each value of E_{peak}, but the maximum visibility is now centred around $E_0 = E_{\text{peak}}$. This is to be expected, as our choice of E_{peak} dictates the optimum energy at which the effect of phase averaging is eradicated.

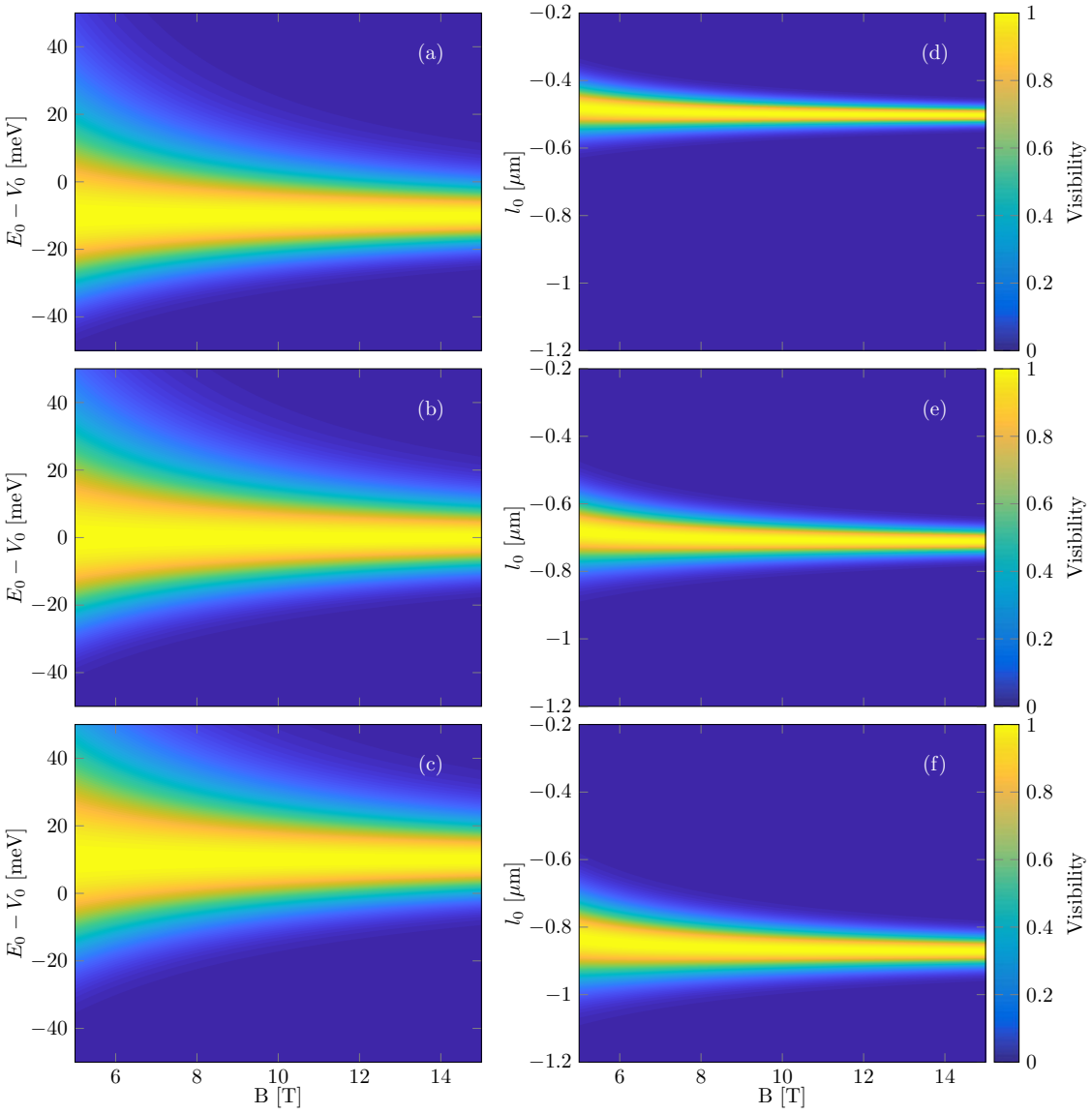

Figure 3.8: On the left, we have the visibility of an electron in a system with changing values of E_{peak}. Part (a) is for $E_{\text{peak}} = 90$ meV, (b) is for $E_{\text{peak}} = 100$ meV and (c) is for $E_{\text{peak}} = 110$ meV. The right hand side shows the visibility for an electron against the path length offset l_0 and the magnetic field, shown for three different values of E_0. Part (d) is for $E_0 = 50$ meV, (e) is for $E_0 = 100$ meV and (f) is for $E_0 = 150$ meV.

The results in Fig. 3.8 (d), (e) and (f) show the visibility against the path length difference $l_0 = 2(Y_U - Y_L)$ and magnetic field. Parts (d), (e) and (f) show the optimum path length difference for injection energies $E_0 = 50, 100$ and 150 meV, respectively. We can see that for increasing injection energy, the required offset

between the magnitude of the difference between the upper and lower path lengths increases. We also see that the range of path length offsets for maximum visibility increases with energy as well, so you are more likely to get a high visibility from the interferometer when operated at high energies, as far as phase averaging is concerned. This is not necessarily the case when other incoherent effects come in to play, however, as will be discussed later in this thesis. The visibility is more strongly peaked for higher magnetic fields because as the magnetic field increases, the width of the wavepacket, Σ_l', decreases which in turn reduces the phase averaging contribution to the visibility for fixed values of l_0 and l_{off}.

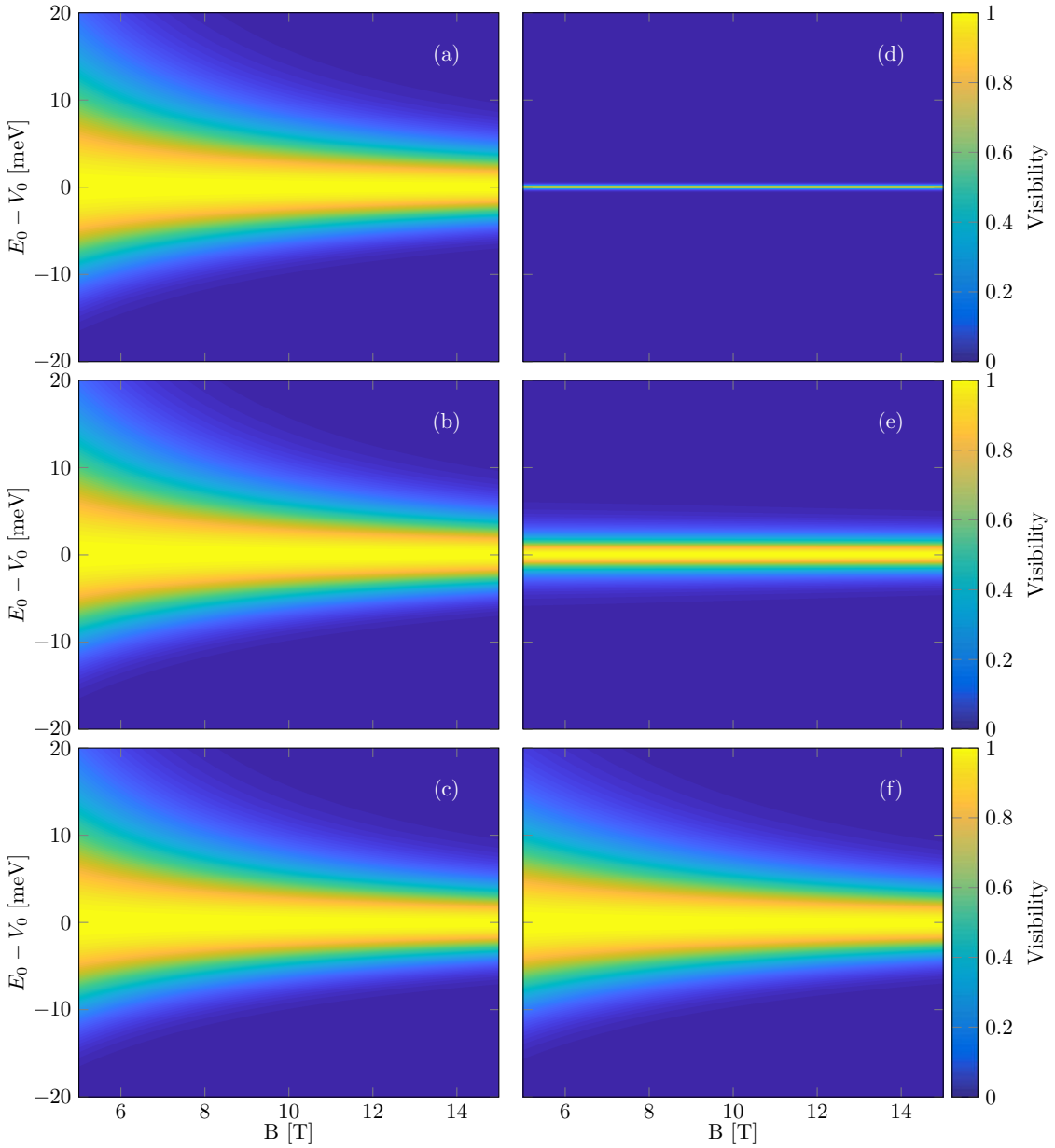

Figure 3.9: A comparison of the effect of energy dependence of the beamsplitters on the visibility as a function of $E_0 - V_0$ and magnetic field. Parts (a), (b) and (c) show the energy independent beamsplitters and (d), (e) and (f) are for energy dependent beamsplitters. This comparison is shown for various beamsplitter widths. In (a) and (d), $E_{\text{sad}} = 1$ meV, in (b) and (e), $E_{\text{sad}} = 10$ meV and in (c) and (f), $E_{\text{sad}} = 100$ meV.

The previous results have all been shown for energetically extremely wide beamsplitters. In these cases, the energy dependence of the beamsplitters doesn't have much of an effect, as the wavepacket only "sees" a small part of the beamsplitter, and therefore experiences essentially the same transmission and reflection coefficients throughout, however as the width of the beamsplitter decreases towards the width of the electron wavepacket (in this case, $\sigma_E = 1$ meV), we find that the dependence on energy becomes of much more significance. This can be seen in Fig. 3.9. In this figure, parts (a), (b) and (c) show the energy independent beamsplitters, and (d), (e) and (f) show the energy dependent beamsplitters derived in the previous section. They also vary in E_{sad} for each row, where (a) and (d) are for a beamsplitter width of $E_{\text{sad}} = 1$ meV, (b) and(e) are for $E_{\text{sad}} = 10$ meV and (c) and (f) are for $E_{\text{sad}} = 100$ meV.

It is clear from these heatmaps that the closer in width the electron wavepacket is to the width of the beamsplitter, the more important it becomes to take into account the energy dependence. For example, for $E_{\text{sad}} = \sigma_E = 1$ meV, the energy independent calculation of the visibility significantly overestimates the range of E_0 values for which the visibility is optimised.

The difference between the energy dependent and energy independent ranges can be seen in more detail in Fig. 3.10, for varying $E_0 - V_0$. Each of the lines is for a different magnetic field, and we can see that as the magnetic field increases, the overall percentage difference between the energy dependent and energy independent simulations decreases. Interestingly, we see that for the chosen values of beamsplitter width, the two simulations never match completely. They appear to converge as $E_0 \to 100$ meV, however they are never identical, and the difference is noticeably large for beamsplitter widths above those which are experimentally reasonable. The fidelity is defined as $\int \mathrm{d}E\, \tilde{\nu}_{\text{edep}} \tilde{\nu}_{\text{indep}}$, where ν_{edep} and ν_{indep} are the visibilities for the energy dependent and independent cases respectively, normalised by $\tilde{\nu} = \nu / \sqrt{\int \mathrm{d}E\, \nu^2}$ such that a perfect overlap would correspond to a fidelity of 1.

In the case of the visibility at constant E_0 for varying values of l_0, as shown in Fig. 3.8 d, e and f, there is not the same dependence on energy on the visibility, as the transmission and reflection coefficients do not depend on the path length at all.

This follows the same logic as above. When the beamsplitter width is small (approaching the width of the wavepacket itself), the wavepacket experiences multiple transmission and reflection coefficients at different points within itself, such that it no longer interferes perfectly at the second beamsplitter. If we assume a 50:50 beamsplitter, this effect is non-existent, so when comparing the energy dependent and independent cases, they differ significantly more in the narrow beamsplitter regime.

Beggi *et al.* (following [88]) give a simple theoretical treatment of the visibility that is the same as the above but does not take into account the change in path length and therefore phase obtained due to the uncertainty in the electron energy. Translating into our notation, Beggi's result for the visibility reads

$$\nu = \exp\left\{-\frac{1}{2}\frac{\sigma_E^2}{(\hbar v_0)^2} l_0^2\right\}. \tag{3.66}$$

Thus, relative to this result, our theory predicts two effects: the raw path difference l_0 is shifted to an effective value of $l_0 + l_{\text{off}}$ and the width is reduced by a factor of $\Omega^2/(\Omega^2 + \omega_c^2) \leq 1$. Beggi *et al.* also describe full numerical simulations of electron

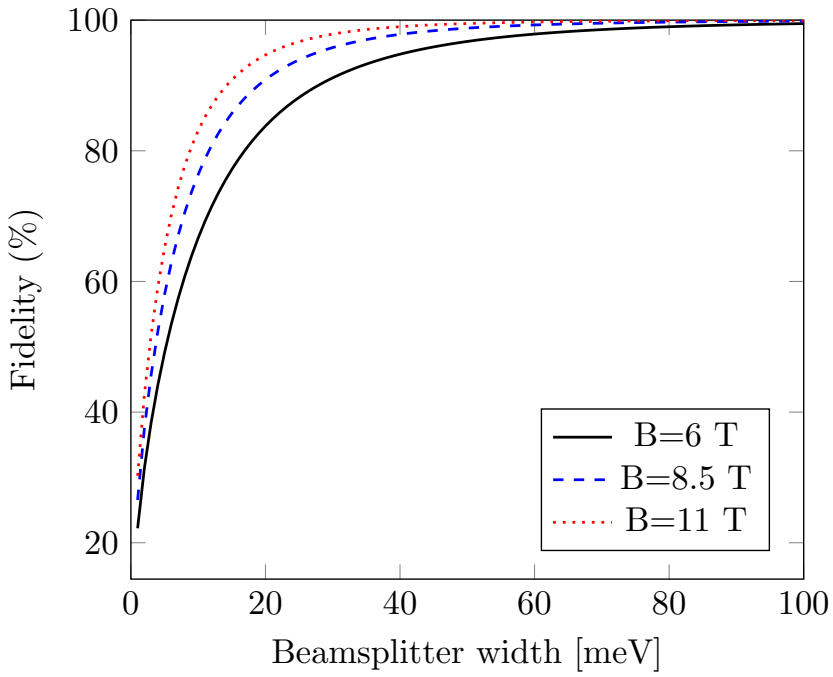

Figure 3.10: The fidelity as a percentage similarity of the energy dependent to energy independent visibilities for varying E_0 are shown of the plots in Fig. 3.9, for three chosen magnetic fields over a continuous range of beamsplitter widths.

transit through a MZI. In the results from these simulations, they do find evidence of the first of these effects. A numerical fit to their simulations gives a value of $l_{\text{off}} \approx 150\,\text{nm}$, which is within the range described here.

They do not find evidence of the latter effect. Indeed, their simulations show that the width Σ_l is increased by a factor in the range 1–2 that depends on the initial width σ_E. This they attribute to the energy dependence of the transmission probabilities, which is presumably captured by the shift from Σ_l to Σ_l'.

3.9 Chapter summary

In this chapter we have calculated the current in an electronic MZI with hot-electrons. We have established the effect of small changes in the energy of an electron on the length of the paths travelled inside the interferometer. The electron wavepacket generates two phase contributions which depend on the geometry of the system: the dynamical phase and the AB phase. We have found here that the small changes in energy that cause small changes in the path length actually have a large effect on the overall phase of the electron on detection. If the electron picks up slightly different phases due to the uncertainty of the electron energy, the electron will not interfere perfectly at the second beamsplitter, which reduces the amplitude of the current and therefore the visibility of the system. We have found that this effect of phase averaging can be reduced completely by introducing an offset to the path lengths of the upper and lower arms. This is contrary to the logic in optics, where the optimum setup is to have paths the same length, as has also been discussed in previous analytic treatment of electronic phase averaging [57, 66, 89]. The need for an offset, l_{off}, can be explained by the chirality of the edge channels

in the system. It's a lot easier for an electron to travel down in one direction than in the other, which means that there is an added travel time associated with one of the paths, which can be compensated for by making one of the paths longer than the other.

We also compare with the work of Beggi *et al.* [89] who derived a visibility with a zero offset. In their full simulations of electron transit through an MZI, however, they did find evidence of the maximum visibility being located at some path difference away from zero, which was in the same region as that predicted by our model. For hot-electrons, we find that this is on the order of 1 μm, which is a significant fraction of the size of the interferometers, so ensuring that this offset is taken into account is of significant importance in experiments.

We also investigated what happens when, instead of assuming 50:50 beamsplitters, we take into account the energy dependence of the beamsplitter according to the Fertig-Halperin model [86]. In the case of our calculations, we take into account that the energy of the electron is spread around the central energy, which means that on arrival at the beamsplitter, it will interact with the saddle potential differently across its width in energy space. We have found that for beamsplitters with an energy width much larger than that of the wavepacket, they interact as if the beamsplitter was not energy dependent. The reason for this is that the electron only "feels" a small part of the beamsplitter energy, such that the behaviour of the beamsplitter is the same across the energy width of the electron. As the wavepacket always has some width in energy, the energy dependent and energy independent models are never identical, however in the case of beamsplitters much wider than the wavepackets the energy independent model of the beamsplitter is valid. This is not so for narrower beamsplitters. As the energy width of the beamsplitter decreases towards the energy width of the wavepacket, the action of the beamsplitter on the wavepacket varies across the entire energy width of the wavepacket, affecting both the phase picked up by the wavepacket and the transmission and reflection probabilities.

Chapter 4

Arrival time distributions in Mach-Zehnder interferometers

As well as looking at the visibility of an electron arriving at a detector in a MZI, we can also investigate a property called the arrival time distribution (ATD), which describes the probability density that an electron will arrive at the detector at a certain time. These are calculated using the probability distribution of the electrons, taking into account all of the phases, including the full beamsplitter phases.

In this chapter, I will derive the ATD of the electrons using the scattering matrices. I start with a simplified version of the beamsplitters, before introducing the full beamsplitter phases and transmission and reflection coefficients. At the end of this chapter, I will introduce the concept of asymmetry of the beamsplitters and calculate the ATDs for different levels of asymmetry.

The numerical results in this chapter use the full equations for the potential of the system, while the analytics use an approximate form. While less accurate than the full numerics, these analytics are shown to be good approximations and can be used as a much faster way to investigate the effects of changes in parameters without the use of the time consuming numerical simulations. For example, it is useful to use the analytics to establish an area to focus on before using the numerics to obtain a much more detailed and accurate picture. It is also useful to give some intuition as to the behaviour, rather than relying only on the numerical data.

4.1 Arrival time distributions

The arrival time distribution of an electron is the probability density of how likely an electron of a given energy is to arrive in a channel by at that time. The ATDs are given by multiplying the probability distribution of an electron being detected in one of the channels by the velocity of the electron. Considering first an electron being detected in the upper channel, we can combine Eq. (3.9) and Eq. (3.2) to find the upper component of the wavefunction in time, which is given as

$$|\Psi_U(t)\rangle = \frac{N_\alpha L}{2\pi} \int \mathrm{d}k e^{-\alpha(k-k_0)^2} r^{\mathrm{MZI}} e^{-iE_k t/\hbar} |0k\rangle \,. \tag{4.1}$$

Electron transport occurs explicitly in the x-direction, so we can take the trace over y to average over the y contributions and give the probability distribution for the

upper channel as

$$P_U(x,t) = \int \mathrm{d}y |\langle xy|\Psi_U(t)\rangle|^2. \tag{4.2}$$

As $|\langle xy|\Psi_U(t)\rangle|^2 = \langle xy|\Psi_U(t)\rangle^* \langle xy|\Psi_U(t)\rangle$, the probability density is

$$P_U(x,t) = \frac{N_\alpha^2 L}{(2\pi)^2} \int \mathrm{d}y \int \mathrm{d}k \int \mathrm{d}k' e^{-\alpha(k-k_0)^2} e^{-\alpha(k'-k_0)^2} e^{-i(E_k - E_{k'})t/\hbar} \times r_k^{\mathrm{MZI}} \left(r_{k'}^{\mathrm{MZI}}\right)^* e^{ikx} e^{-ik'x} \chi_{0k}(y) \chi_{0k'}^*(y). \tag{4.3}$$

We can now take the trace over y to get an expression in terms of only x and t, using Eq. (3.5)

$$\int \mathrm{d}y \chi_{0k'}^*(y)\chi_{0k}(y) = \int \mathrm{d}y \frac{1}{\sqrt{\pi} l_\Omega} \exp\left\{-\frac{1}{2}\left[\frac{y - y_G(k)}{l_\Omega}\right]^2\right\} \exp\left\{-\frac{1}{2}\left[\frac{y - y_G(k')}{l_\Omega}\right]^2\right\} \tag{4.4}$$

$$= \exp\left[-\frac{\mu^2}{4}(k-k')^2\right], \tag{4.5}$$

where

$$\mu = \frac{\omega_c}{\Omega} l_\Omega. \tag{4.6}$$

such that the probability density becomes

$$P_U(x,t) = \frac{N_\alpha^2 L}{(2\pi)^2} \int \mathrm{d}k \int \mathrm{d}k' e^{-\alpha(k-k_0)^2} e^{-\alpha(k'-k_0)^2} \exp\left[-\frac{i(E_k - E_{k'})t}{\hbar}\right] \times r_k^{\mathrm{MZI}} \left(r_{k'}^{\mathrm{MZI}}\right)^* e^{i(k-k')x} \exp\left[-\frac{\mu^2}{4}(k-k')^2\right]. \tag{4.7}$$

We can now introduce new integration variables, which will make the numerical integration easier to perform. Recalling the definition $k = k_0 + \Delta k$, we can define

$$q = \Delta k - \Delta k' = k - k'; \qquad q' = \Delta k + \Delta k' = k + k' - 2k_0, \tag{4.8}$$

such that

$$E_k - E_{k'} = \hbar v_0 (k - k') = \hbar v_0 q. \tag{4.9}$$

As before, we assume that the electron wavepacket moves with constant velocity along its whole width, such that the velocity depends on k_0 only, rather than k and k'. We can also combine and rearrange to give expressions for k and k' in terms of q and q',

$$k = \frac{q + q'}{2} + k_0; \qquad k' = \frac{q' - q}{2} + k_0. \tag{4.10}$$

The integration now becomes

$$\int \mathrm{d}k \int \mathrm{d}k' \to \frac{1}{2} \int \mathrm{d}q \int \mathrm{d}q'. \tag{4.11}$$

where the half comes from the Jacobian. This means that we have an equation for the probability distribution of

$$P_U(x,t) = \frac{N_\alpha^2 L}{8\pi^2} \int \mathrm{d}q \int \mathrm{d}q' e^{-\frac{1}{2}\left(\alpha + \frac{1}{2}\mu^2\right)q^2} e^{-\frac{1}{2}\alpha q'^2} e^{iq(x - v_0 t)} r^{\mathrm{MZI}}_{k_0 + \frac{1}{2}(q+q')} \left(r^{\mathrm{MZI}}_{k0 + \frac{1}{2}(q'-q)}\right)^* \tag{4.12}$$

and we can use the same method to get an equation for the lower path of

$$P_L(x,t) = \frac{N_\alpha^2 L}{8\pi^2}\int \mathrm{d}q \int \mathrm{d}q' e^{-\frac{1}{2}\left(\alpha+\frac{1}{2}\mu^2\right)q^2} e^{-\frac{1}{2}\alpha q'^2} e^{iq(x-v_0t)} t^{\mathrm{MZI}}_{k_0+\frac{1}{2}(q+q')} \left(t^{\mathrm{MZI}}_{k0+\frac{1}{2}(q'-q)}\right)^*. \tag{4.13}$$

In order to calculate the ATDs, we can multiply this probability distribution by velocity, which gives

$$A_U(x_D,\tau) = v_0 P_U(x_D,\tau), \tag{4.14}$$
$$A_L(x_D,\tau) = v_0 P_L(x_D,\tau). \tag{4.15}$$

Here, x_D is the detector position, which we will choose as 0.

4.2 Energy dependent beamsplitters

Previously, we have set the beamsplitter contribution to the phase to 0. In this section we will introduce the beamsplitter phases, starting with a simplified version, where we set $\rho_i = \tilde{\rho}_i = \tilde{\theta}_i = 0$ and $\theta_i = \pi$, which gives us equations for the upper and lower wavefunctions of

$$r^{\mathrm{MZI}} = \sqrt{R_1 R_2} e^{i\phi_U} + \sqrt{T_1 T_2} e^{i(\pi+\phi_L)}, \tag{4.16}$$
$$t^{\mathrm{MZI}} = \sqrt{R_1 T_2} e^{i(\pi+\phi_U)} + \sqrt{T_1 R_2} e^{i(\pi+\phi_L)}. \tag{4.17}$$

and derive the beamsplitter portions of Eq. (4.12) and Eq. (4.13), i.e.

$$r_k^{\mathrm{MZI}} \left(r_{k'}^{\mathrm{MZI}}\right)^* = \left(\sqrt{R_1^{(k)} R_2^{(k)}} e^{i\phi_U(k)} + \sqrt{T_1^{(k)} T_2^{(k)}} e^{i[\pi+\phi_L(k)]}\right) \times \left(\sqrt{R_1^{(k')} R_2^{(k')}} e^{-i\phi_U(k')} + \sqrt{T_1^{(k')} T_2^{(k')}} e^{-i[\pi+\phi_L(k')]}\right), \tag{4.18}$$

$$t_k^{\mathrm{MZI}} \left(t_{k'}^{\mathrm{MZI}}\right)^* = \left(\sqrt{R_1^{(k)} T_2^{(k)}} e^{i[\pi+\phi_U(k)]} + \sqrt{T_1^{(k)} R_2^{(k)}} e^{i[\pi+\phi_L(k)]}\right) \times \left(\sqrt{R_1^{(k')} T_2^{(k')}} e^{-i[\pi+\phi_U(k')]} + \sqrt{T_1^{(k')} R_2^{(k')}} e^{-i[\pi+\phi_L(k')]}\right). \tag{4.19}$$

For the purposes of legibility, we will continue to refer to everything in terms of k and k' for now, but we will switch to the q, q' variables later on when it has been simplified as far as possible in current terms. The beamsplitter transmissions have the saddle point form as discussed in Chapter 3, given by

$$T_i(E_k) = \frac{1}{1+\exp\left[-\frac{\pi(E_k-V_0)}{E_{\mathrm{sad}}}\right]} \tag{4.20}$$

which is in terms of E as a function of k. The energy width of the beamsplitter is E_{sad}.

4.3 Phases

We can now consider the phases for the upper and lower part by first expanding the phase with respect to the wavenumber k around k_0, with $\Delta k = k - k_0$, such that

$$\phi^{U/L}(k) = \phi_0^{U/L} + (k - k_0)\phi_{k1}^{U/L}, \tag{4.21}$$

with

$$\phi_0^{U/L} = \phi^{U/L}(k_0); \qquad \phi_{k1}^{U/L} = \left.\frac{\mathrm{d}\phi^{U/L}}{\mathrm{d}k}\right|_{k=k_0}. \tag{4.22}$$

Applying this to our phase factors we get

$$r_k^{\mathrm{MZI}} \left(r_{k'}^{\mathrm{MZI}}\right)^* = \sum_{n=1}^{4} d_n^U \exp\left[i\left(a_n^U + b_n^U q + c_n^U q'\right)\right] \tag{4.23}$$

$$t_k^{\mathrm{MZI}} \left(t_{k'}^{\mathrm{MZI}}\right)^* = \sum_{n=1}^{4} d_n^L \exp\left[i\left(a_n^L + b_n^L q + c_n^L q'\right)\right]. \tag{4.24}$$

with the coefficients $a_n^{U/L}, b_n^{U/L}, c_n^{U/L}$ and $d_n^{U/L}$ as in table 4.1. The probability density of the upper and lower paths can now be written as

$$P_{U/L}(x,t) = \frac{N_\alpha^2 L}{8\pi^2} \sum_{n=1}^{4} d_n^{U/L} e^{i a_n^{U/L}} \int \mathrm{d}q' \exp\left[-\frac{\alpha}{2} q'^2 + i c_n^{U/L} q'\right] \times \int \mathrm{d}q \exp\left[-\frac{\left(\alpha + \frac{1}{2}\mu^2\right)}{2} q^2 + i\left(x - v_0 t + b_n^{U/L}\right) q\right]. \tag{4.25}$$

Now that we know how the phases combine in the integral, we can return to the geometric phases from Chapter 3, and split these in terms of their relationship to k.

		$a_n^{U/L}$	$b_n^{U/L}$	$c_n^{U/L}$	$\left(d_n^{U/L}\right)^2$
P_U	$n=1$	0	ϕ_{k1}^U	0	$R_1^{(k)} R_2^{(k)} R_1^{(k')} R_2^{(k')}$
	$n=2$	$\phi_0^U - \phi_0^L - \pi$	$\frac{1}{2}\left(\phi_{k1}^U + \phi_{k1}^L\right)$	$\frac{1}{2}\left(\phi_{k1}^U - \phi_{k1}^L\right)$	$R_1^{(k)} R_2^{(k)} T_1^{(k')} T_2^{(k')}$
	$n=3$	$-\left(\phi_0^U - \phi_0^L - \pi\right)$	$\frac{1}{2}\left(\phi_{k1}^U + \phi_{k1}^L\right)$	$-\frac{1}{2}\left(\phi_{k1}^U - \phi_{k1}^L\right)$	$T_1^{(k)} T_2^{(k)} R_1^{(k')} R_2^{(k')}$
	$n=4$	0	ϕ_{k1}^L	0	$T_1^{(k)} T_2^{(k)} T_1^{(k')} T_2^{(k')}$
P_L	$n=1$	0	ϕ_{k1}^U	0	$R_1^{(k)} T_2^{(k)} R_1^{(k')} T_2^{(k')}$
	$n=2$	$\phi_0^U - \phi_0^L$	$\frac{1}{2}\left(\phi_{k1}^U + \phi_{k1}^L\right)$	$\frac{1}{2}\left(\phi_{k1}^U - \phi_{k1}^L\right)$	$R_1^{(k)} T_2^{(k)} T_1^{(k')} R_2^{(k')}$
	$n=3$	$-\left(\phi_0^U - \phi_0^L\right)$	$\frac{1}{2}\left(\phi_{k1}^U + \phi_{k1}^L\right)$	$-\frac{1}{2}\left(\phi_{k1}^U - \phi_{k1}^L\right)$	$T_1^{(k)} R_2^{(k)} R_1^{(k')} T_2^{(k')}$
	$n=4$	0	ϕ_{k1}^L	0	$T_1^{(k)} R_2^{(k)} T_1^{(k')} R_2^{(k')}$

Table 4.1: Coefficients for the upper and lower channels. Here we have $d_n^{U/L} > 0$.

4.4 Dynamical and Aharonov-Bohm phases

We can recall the expressions for the geometric phases from Chapter 3, where Y_U and Y_L are the vertical contributions to the interferometer path and X is the horizontal path. When we include a small change in energy, ΔE, these contributions become $Y_U + \Delta y$ and $Y_L - \Delta y$ respectively, and X becomes $X \pm 2\Delta y$, for the upper/lower paths. We have the dynamical phase,

$$\phi_{\text{dyn}}^{U/L} = k x_{U/L} \tag{4.26}$$

where x_U and x_L are the upper and lower paths, which gives the dynamical phases as

$$\phi_{\text{dyn}}^{U/L} = k\left[2Y_{U/L} \pm X + 4\Delta y - d\right] \tag{4.27}$$

and the Aharonov-Bohm phase,

$$\phi_{\text{AB}}^{U/L} = -\frac{e}{\hbar}\int_0^{X+2\Delta y} (\mp B[Y_{U/L} \pm \Delta y])\,\mathrm{d}x = \pm\frac{e}{\hbar}B[Y_{U/L} \pm \Delta y][X \pm 2\Delta y] \tag{4.28}$$

giving

$$\phi_{\text{AB}}^{U/L} = \pm\frac{e}{\hbar}BX(Y_{U/L} \pm \Delta y) \tag{4.29}$$

which can be written in terms of k_0, as $\Delta y = (\omega_c^2/\Omega^2)\,(\hbar/eB)\,(k - k_0)$. When combined, our total phases from the upper and lower paths respectively are

$$\phi_U(k) = \frac{eB}{\hbar}XY_U + \left(\frac{\omega_c}{\Omega}\right)^2 X(k - k_0) + k\left[2Y_U + X - d\right] + 4\left(\frac{\omega_c}{\Omega}\right)^2 \frac{\hbar}{eB}\left(k^2 - k_0 k\right) \tag{4.30}$$

$$\phi_L(k) = -\frac{eB}{\hbar}XY_L + \left(\frac{\omega_c}{\Omega}\right)^2 X(k - k_0) + k\left[2Y_L + X - d\right] - 4\left(\frac{\omega_c}{\Omega}\right)^2 \frac{\hbar}{eB}\left(k^2 - k_0 k\right) \tag{4.31}$$

So using the relations in Eq. (4.22) we get

$$\phi_0^U = \frac{eB}{\hbar}XY_U + k_0\left[2Y_U + X - d\right] \tag{4.32}$$

$$\phi_{k1}^U = \left(\frac{\omega_c}{\Omega}\right)^2 X + \left[2Y_U + X - d\right] + 4\left(\frac{\omega_c}{\Omega}\right)^2 \frac{\hbar}{eB}k_0 \tag{4.33}$$

$$\phi_0^U = -\frac{eB}{\hbar}XY_L + k_0\left[2Y_L + X - d\right] \tag{4.34}$$

$$\phi_{k1}^U = \left(\frac{\omega_c}{\Omega}\right)^2 X + \left[2Y_L + X - d\right] - 4\left(\frac{\omega_c}{\Omega}\right)^2 \frac{\hbar}{eB}k_0 \tag{4.35}$$

We can use these simplified delay times to investigate the effect of a change in the energy, E_{peak}, (which we recall from Chapter 3 is the energy used to calculate the optimal path lengths) on the ATD. Figure 4.1 shows the ATDs for an electron travelling through an interferometer with an energy of $E_0 = 100\,\text{meV}$, where in each panel the value of E_{peak} has been changed such that the interferometer is no longer optimised for use with an electron of this energy. We can see in Fig. 4.1 that when $E_{\text{peak}} = E_0 = 100$ meV, as in (a), the lobes from the upper and lower paths arrive at the same time, such that we have maximum interference between the two paths.

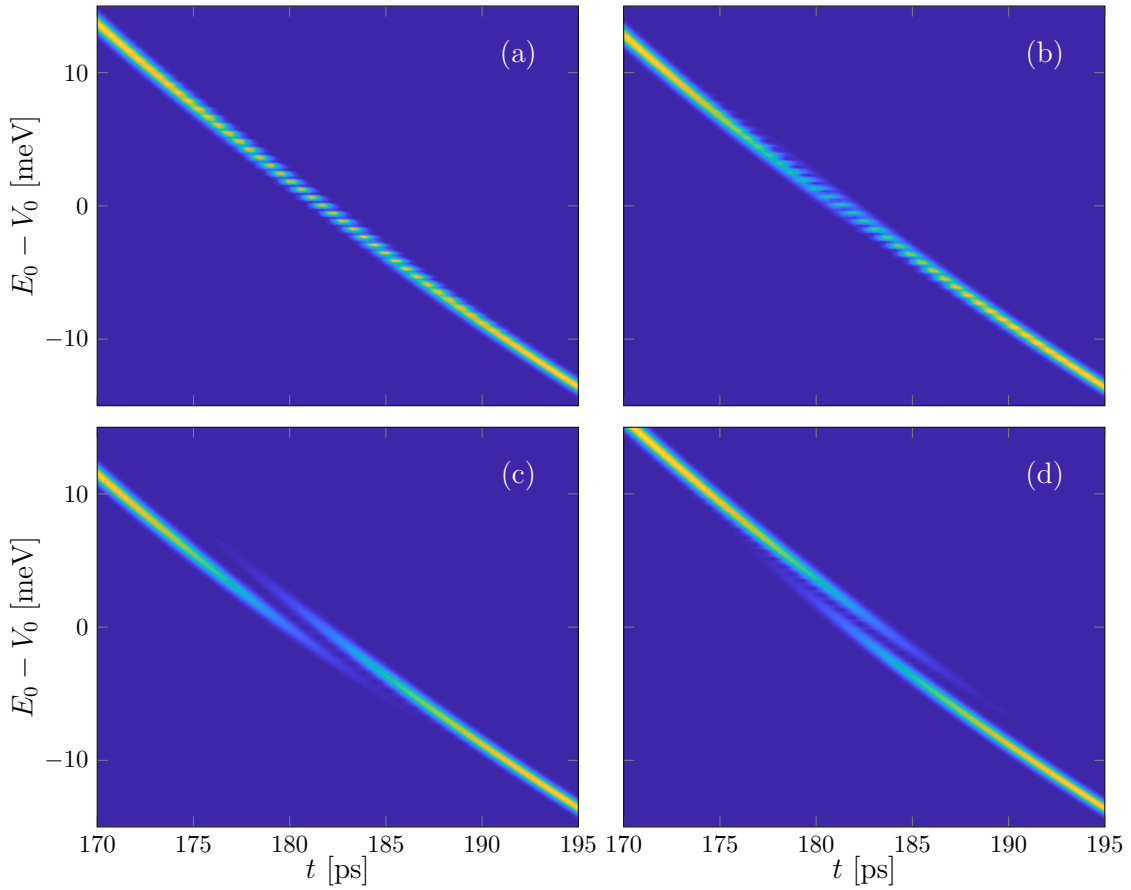

Figure 4.1: The ATD for electrons with the simple model of the beamsplitters from Section 4.2. Parts (a), (b), (c) and (d) show the results for $E_{\text{peak}} = 100, 90, 75$ and 125 meV respectively. We can see the two lobes from the upper and lower paths clearly, and the interference that occurs in their overlap. Other parameters for these simulations are $\sigma_E = 1$ meV, $E_{\text{sad}} = 10.52$ meV, $B = 11$ T, and the lengths of the interferometer arms had the horizontal length $X = 5$ and the vertical lengths $Y_U = 2$ μm, $Y_L = Y_U - 1/2l_{\text{off}}$, where l_{off} is calculated at each value ofE_{peak}.

If we change E_{peak} such that the path lengths are different to the optimum, we see that the two lobes no longer meet at $E_0 = 100$ meV. When the path offset isn't too far from optimised, as in (b) where $E_{\text{peak}} = 90$ meV, we still see some interference, however the amplitude of this interference, and therefore the visibility will no longer be maximised. The further from the optimum path lengths that we get, the less interference we see, until the electrons arrive at such different times that there is no longer any interference observed. In Fig. 4.1 (c) and (d) we see the case where $E_{\text{peak}} = 75$ meV and $E_{\text{peak}} = 125$ meV respectively. We can see clearly here that the lower path stays in position while the arrival from the upper path is the one that changes. This is because of the way we have defined Y_U and Y_L and their dependence on l_{off}.

4.5 Delay times

If we assume a narrow wavepacket where $\sqrt{\alpha} \gg k_0^{-1}$, we can sum Eq. (4.27) and Eq. (4.29) and linearise with respect to Δk to obtain the total phases picked up

along the arms

$$\phi_p \approx \pm\frac{eB}{\hbar}XY_{U/L} + k_0(2Y_{U/L} - d + X) + \Delta k\left\{\frac{\Omega^2+\omega_c^2}{\Omega^2}(2Y_pU/L + X) - d \pm 4k_0l_\Omega^2\left(\frac{\omega_c}{\Omega}\right)\right\}. \quad (4.36)$$

As Δy is very small in comparison to the size of the interferometer, we have very small changes in the paths. The validity of these expressions also relies on the path changes being small relative to the size of the MZI, i.e. $\sqrt{\alpha} \gg l_c^2/(2Y_{U/L} + X)$ for $\omega_c \gg \omega_y$. The beamsplitter transmission and reflection probabilities vary slowly with k when compared with the phases, so we can evaluate T and R at the central wave number k_0. Linearising the dispersion, as in Eq. (3.29) such that we have $E_k \simeq E_{k_0} + \hbar v_0\Delta k$ and performing the integration in Eq. (4.12) combined with Eq. (4.14) we get an equation for the ATD in the upper channel of the interferometer of

$$\mathcal{A}(t) \approx \sqrt{\frac{v_0^2}{\pi\left(2\alpha+\mu^2\right)}}\left\{R_1^{(0)}R_2^{(0)}\exp\left[-\frac{\left\{x_D - v_0(t-\tau_U)\right\}^2}{2\alpha+\mu^2}\right] + T_1^{(0)}T_2^{(0)}\exp\left[-\frac{\left\{x_D - v_0(t-\tau_L)\right\}^2}{2\alpha+\mu^2}\right] + 2\sqrt{R_1^{(0)}R_2^{(0)}T_1^{(0)}T_2^{(0)}} \times \exp\left[-\frac{v_0^2(\tau_U-\tau_L)^2}{8\alpha} - \frac{\left\{x_D - v_0(t-\frac{1}{2}\tau_L-\frac{1}{2}\tau_U)\right\}^2}{2\alpha+\mu^2}\right]\cos\Phi_0\right\}. \quad (4.37)$$

We can see that the ATD shows two moving lobes, resulting from travel round the upper and lower paths, and an interference term between them. The delay time of the two lobes is given by

$$\tau_p = \hbar\frac{d\Phi_p}{dE}\bigg|_{E=E0} = \frac{1}{v_0}\frac{d\Phi_p}{dk}\bigg|_{k=k_0}, \quad (4.38)$$

where

$$\Phi_U = \rho_1 + \rho_2 + \phi_U; \Phi_L = \theta_1 + \widetilde{\theta}_2 + \phi_L. \quad (4.39)$$

The interference term shows oscillations as a function of the central phase difference

$$\Phi_0 = \Phi_U - \Phi_L|_{k=k_0} = -\pi\frac{eB}{\hbar}a_0 + k_0l_0 + \Phi_0^{\mathrm{BS}}, \quad (4.40)$$

expressed in terms of the area enclosed by the central path, a_0, and the corresponding central path difference, l_0. We have also identified the beamsplitter contribution

$$\Phi_0^{\mathrm{BS}} = \rho_1 - \theta_1 + \rho_2 - \widetilde{\theta}_2\Big|_{k=k_0}. \quad (4.41)$$

Integrating Eq. (4.37) over time, we obtain the total probability of detection at the output to be

$$P_{\mathrm{tot}} = R_1^{(0)}R_2^{(0)} + T_1^{(0)}T_2^{(0)} + 2\sqrt{R_1^{(0)}R_2^{(0)}T_1^{(0)}T_2^{(0)}}\,\mathcal{D}\cos\left(\Phi_0\right) \quad (4.42)$$

where $\mathcal{D} = \exp\left[-v_0^2(\Delta\tau)^2/\left(8\alpha\right)\right]$, depends on the difference in delay times

$$\begin{aligned}\Delta\tau =& \tau_U - \tau_L \\ =& v_0^{-1}\frac{d}{dk}\left[\phi_U - \phi_L\right]_{k=k0} + \Delta\tau_{\mathrm{BS}}.\end{aligned} \tag{4.43}$$

with

$$\Delta\tau_{\mathrm{BS}} = v_0^{-1}\frac{d}{dk}\left(\rho_1 + \rho_2 - \theta_1 - \widetilde{\theta}_2\right), \tag{4.44}$$

the contribution due to the beamsplitters. The visibility of oscillations displayed by Eq. (4.42) is

$$\mathcal{V} = \mathcal{D} \times \frac{2\sqrt{R_1^{(0)}R_2^{(0)}T_1^{(0)}T_2^{(0)}}}{R_1^{(0)}R_2^{(0)} + T_1^{(0)}T_2^{(0)}} \tag{4.45}$$

such that $\mathcal{D}$ is observed to be the non-trivial contribution to the visibility that arises from phase averaging. We can see from this that when the beamsplitter is 50:50, $\mathcal{V} \to \mathcal{D}$. Writing $\alpha = \left(\hbar v_0/2\sigma_E\right)^2$ in terms of the energetic width σ_E of the initial wave packet, we can rewrite this phase-averaging factor as

$$\mathcal{D} = \exp\left\{-\frac{1}{2}\left(\frac{l_0 + l_{\mathrm{offset}}}{\Sigma_l}\right)^2\right\}. \tag{4.46}$$

This is the same as the phase averaging factor in Chapter 3, now with an expression for l_{offset} which also includes a contribution from the delay time of the electron,

$$l_{\mathrm{offset}} = \frac{\Omega^2 v_0}{\Omega^2 + \omega_c^2}\left[\frac{8\omega_c}{\omega_y^2} + \Delta\tau_{\mathrm{BS}}\right], \tag{4.47}$$

and the coherence length of the electron wave packet

$$\Sigma_l = \frac{\Omega^2}{\Omega^2 + \omega_c^2}\frac{\hbar v_0}{\sigma_E}. \tag{4.48}$$

Addressing the beamsplitter contribution in the above, if we make no further assumptions about the beamsplitters other than that they act symmetrically on electrons coming from different directions, the beamsplitter phases obey

$$\rho_i = \widetilde{\rho}_i = \theta_i - \pi/2 = \widetilde{\theta}_i - \pi/2, \tag{4.49}$$

at all wave numbers k. From this it follows that the delay difference is zero, $\Delta\tau_{\mathrm{BS}} = 0$, and the beamsplitters do not affect the phase averaging. The effect of asymmetric beamsplitters is discussed in Sec. 4.7.

Then, assuming symmetric beamsplitters and parameters typical of hot-electron experiments we find the offset length to assume a value $l_{\mathrm{offset}} \approx 700\,\mathrm{nm}$. In contrast, the coherence length is $\Sigma_l \approx 34\,\mathrm{nm}$ for a wave packet of energetic width $\sigma_E = 1\,\mathrm{meV}$. Thus, it is essential that the construction of a hot-electron MZI be such that the path difference satisfies $l_0 \approx -l_{\mathrm{offset}}$ at the injection energy, E_0 if interference is to be observed. At high magnetic fields, the offset length is largely independent of the field strength because the dependency from the cyclotron frequency cancels with that of the velocity.

4.6 Numerical results

We can use the transmission and reflection coefficients, along with the beamsplitter and geometrical phases to numerically simulate the arrival time distributions. These numerical models are useful because they are more accurate than the analytical approximations, however they take a lot more time to obtain results than using the analytics. They can be used in conjunction with one another, with the analytics giving a quick way to find an interesting location to look in, to then use the numerics to investigate in more detail. The predicted offset found in Chapter 3 depends on v_0, and therefore energy, E_0, so we can reintroduce the variable E_{peak} at which this l_{off} is optimised, and phase averaging effects vanish. The phase averaging factor can then be written as

$$\mathcal{D} = \exp\left\{-\frac{1}{2}\left(\frac{E_0 - E_{\text{peak}}}{\Sigma_E}\right)^2\right\} \tag{4.50}$$

where

$$\Sigma_E = \frac{\hbar\omega_y^2 E_{\text{peak}}}{4\omega_c\sigma_E} \tag{4.51}$$

is the energetic width of the visibility peak. For all of the calculations in this section, we set $E_{\text{peak}} = 100\,\text{meV}$ such that we obtain an offset of $l_{\text{offset}} \approx 700\,\text{nm}$. We can then use this l_{offset} to define the lengths of the beamsplitter arms.

We focus first of all on the scenario where the beamsplitters are symmetric and identical, i.e. $T_1 = T_2 = T$. As in Chapter 3, we consider the Fertig-Halperin saddle model of a quantum point contact [86], the transmission of which is

$$T = \frac{1}{[1 + \exp(-\pi\epsilon)]} \tag{4.52}$$

with $\epsilon = (E - V_0)/E_{\text{sad}}$; where $E_{\text{sad}} = \hbar\omega_{\text{BS}}^2/(2\omega_c)$ with $\hbar\omega_{\text{BS}}$ an energy characterising the curvature of the saddle. The phase associated with transmission through the beamsplitter is [1]

$$\theta = -\frac{1}{2}\epsilon + X\sqrt{X^2+\epsilon} + \frac{1}{2}\epsilon\ln\left(\frac{|\epsilon|}{2}\right) - \epsilon g\left(X^2/\epsilon\right) + \text{Im}\left[\ln\Gamma\left(\frac{1}{2} - \frac{i}{2}\epsilon\right)\right], \tag{4.53}$$

where $g(x) = \ln\left|\sqrt{|x| + \text{sgn}(x)} - \sqrt{|x|}\right|$, $X = \left[(d/l_c) - \left(2\epsilon^{(0)} l_c/d\right)\right]/\sqrt{8}$, and $\epsilon^{(0)} = (E_0 - V_0)/E_{\text{sad}}$. In this model, the size d of the beamsplitter region is rather arbitrary, and here we set $d = 3\sqrt{2}l_c$. As explained in the appendix of Ref. [39], the finiteness of this beamsplitter region means that the theory is only valid for energies $|E - V_0| \leq \hbar\omega_{BS}^2 d^2/\left(4\omega_c l_c^2\right)$. The other three beamsplitter phases are obtained through the relation (4.49) in the symmetric case.

Figure 4.2 shows the numerical energy-resolved arrival time distribution, plotted about the mean arrival time $\bar{t} = \int dt\ t\ \mathcal{A}(t)$. Parts (a) and (b) of this figure show results for when the effective width of the beamsplitter transmission E_{sad} is large compared with the visibility width of Eq. (4.51) ($\hbar\omega_{\text{BS}} = 100\,\text{meV}$ giving $E_{\text{sad}} \approx 263\,\text{meV}$ compared with a width of $\Sigma_E \approx 10\,\text{meV}$). In this case, both interferometer paths contribute to the arrival time distribution across the range shown and the

[1] The derivation of these phases was conducted by Sungguen Ryu, one of the coauthors of our paper, Ref. [39].

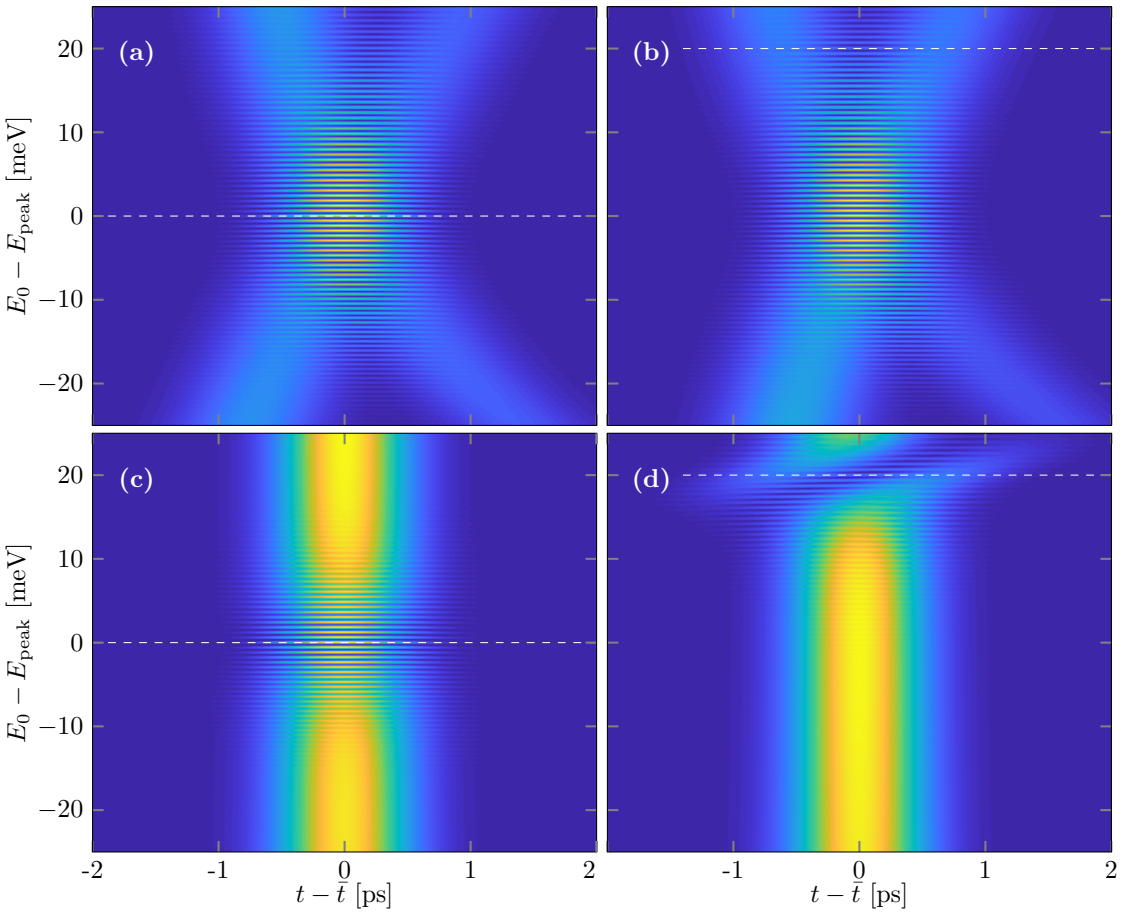

Figure 4.2: The arrival time distributions of electrons after they travel through an MZI as a function of time and injection energy E_0, calculated through the numerical evaluation of Eq. (4.14). The MZI path difference l_0 is set such that $l_0 = -l_{\text{offset}}$ at an energy of $E_{\text{peak}} = 100\,\text{meV}$. Results are plotted about the mean arrival time $\bar{t}$ at each energy. Panels (a) and (b) show results for $\hbar\omega_{\text{BS}} = 100\,\text{meV}$ with $V_0 = 100\,\text{meV}$ and $V_0 = 120\,\text{meV}$ respectively (marked with horizontal lines). With this beamsplitter width, interference is observed around $E_0 = E_{\text{peak}}$ and the position of V_0 is unimportant. Panels (c) and (d) show the same but with $\hbar\omega_{\text{BS}} = 20\,\text{meV}$. For this narrower beamsplitter, interference is observed around V_0 instead.

picture captured by analytic expression Eq. (4.37) is very much born out here. We see two lobes in the arrival time distribution that coincide when $E_0 = E_{\text{peak}}$ such that interference takes place. Figure 4.3 shows the visibility extracted from this numerical data (symbols), in comparison with the analytic result of Eq. (4.45) (solid lines). For the wide beamsplitter case shown in Fig. 4.3a, we see that the visibility is hardly affected by moderate changes in the centre of the beamsplitter transmission V_0. Thus we see the whole of the Gaussian visibility feature predicted by Eq. (4.50). The cross pattern in Fig. 4.2 (a) and (b) is caused by the beamsplitter acting as essentially a 50:50 beamsplitter, due to the fact that the electron only feels a small part of the beamsplitter. The paths in the arrival times are then split between electrons that followed the upper and lower paths equally.

In contrast, Figs. 4.2 (c) and (d) show results for a narrower beamsplitter with $\hbar\omega_{\text{BS}} = 20\,\text{meV}$ and $E_{\text{sad}} = 10.52\,\text{meV}$, which is approximately the visibility width Σ_E. In this case, the appearance of fringes is heavily influenced by the beamsplitter

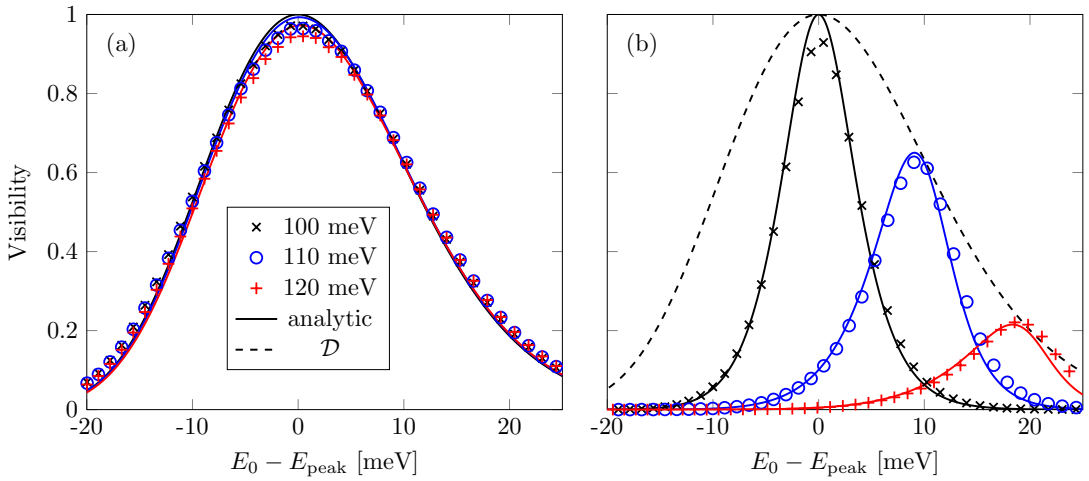

Figure 4.3: The MZI visibility as a function of injection energy E_0 for three values of the beamsplitter centre, $V_0 = 100$, 110 and 120 meV. Part (a) shows results for a beamsplitter width $\hbar\omega_{\rm BS} = 100$ meV; part (b) for $\hbar\omega_{\rm BS} = 20$ meV. Numerical results determined from Fig. 4.2 are shown as symbols; the analytic expression of Eq. (4.45) is shown as solid lines and the phase-averaging factor $\mathcal{D}$ of Eq. (4.46) is shown as a dashed line.

transmission. For the upper and lower energy ranges of Fig. 4.2c, only a single path of the MZI is traversed, and thus interference is restricted to a narrow range around V_0 where the product TR is significantly different from zero. The energy at which this occurs changes as we vary the beamsplitter centre V_0, as can be appreciated in Fig. 4.2d where $V_0 = 120$ meV and the fringes occur at the top of the displayed energy range. These changes are apparent in the visibility plots of Fig. 4.3 (b), where we see numerical visibility for three different values of V_0. We note that the phase-averaging factor $\mathcal{D}$ (dashed line) acts as an approximate envelope for the maximum visibilities as V_0 is changed.

4.7 Role of the beamsplitter phases

The effect of the beamsplitter phases on the MZI properties can be captured by the two quantities: the mean delay

$$\bar{\tau}_{\rm BS} = \frac{1}{2} v_0^{-1} \frac{d}{dk} \left(\rho_1 + \rho_2 + \theta_1 + \widetilde{\theta}_2 \right), \tag{4.54}$$

and the delay difference of Eq. (4.44). In the symmetric case, the wave packet delay given by the phase of Eq. (4.53) is

$$\tau_\theta = \frac{\hbar}{2E_{\rm sad}} \left\{ \ln \frac{|\epsilon|}{2} - 2g\left(\frac{X^2}{\epsilon}\right) - \mathrm{Re}\,\psi\left(\frac{1}{2} + \frac{i}{2}|\epsilon|\right) \right\} \tag{4.55}$$

where ψ is the digamma function. In this case, since all beamsplitter delay times are identical, we have $\bar{\tau}_{\rm BS} = 4\tau_\theta$ and $\Delta\tau_{\rm BS} = 0$. Then as noted above, the beamsplitter plays no role in determining the interference, only in shifting the overall position of the arrival time distribution. We now introduce an asymmetry into the action of the beamsplitters by considering a saddle with a different energetic width on either

side of the midpoint. Taking into account the asymmetry of the beamsplitters, the phases become [2]

$$\theta(E) = \sum_{\alpha=\mathrm{L,R}} \left[-\frac{1}{4}\epsilon_\alpha + \frac{1}{2}X_\alpha(E)\sqrt{X_\alpha^2(E)+\epsilon_\alpha} + \frac{1}{4}\epsilon_\alpha \ln\frac{|\epsilon_\alpha|}{4} - \frac{1}{2}\epsilon_\alpha g(X_\alpha(E)^2/\epsilon_\alpha) \right] + \arg\left[e^{-i\frac{\pi}{4}} \frac{\Gamma(\frac{1}{4}-\frac{1}{4}i\epsilon_\mathrm{R})}{\Gamma(\frac{1}{4}+\frac{1}{4}i\epsilon_\mathrm{R})} - e^{-i\frac{3\pi}{4}} \frac{\Gamma(\frac{3}{4}-\frac{1}{4}i\epsilon_\mathrm{R})}{\Gamma(\frac{3}{4}+\frac{1}{4}i\epsilon_\mathrm{R})} \right] - \arg\left[\frac{\Gamma(\frac{1}{4}-\frac{1}{4}i\epsilon_\mathrm{R})}{\Gamma(\frac{1}{4}-\frac{1}{4}i\epsilon_\mathrm{L})} + \frac{E_{1\mathrm{R}}}{E_{1\mathrm{L}}} \frac{\Gamma(\frac{3}{4}-\frac{1}{4}i\epsilon_\mathrm{R})}{\Gamma(\frac{3}{4}-\frac{1}{4}i\epsilon_\mathrm{L})} \right], \quad (4.56)$$

$$\rho(E) = -\frac{1}{2}\epsilon_\mathrm{L} + X_\mathrm{L}(E)\sqrt{X_\mathrm{L}^2(E)+\epsilon_\mathrm{L}} + \frac{1}{2}\epsilon_\mathrm{L}\ln\frac{|\epsilon_\mathrm{L}|}{4} - \epsilon_\mathrm{L} g(X_\mathrm{L}(E)^2/\epsilon_\mathrm{L}) + \arg\left[e^{-i\frac{\pi}{4}} \frac{\Gamma(\frac{1}{4}-\frac{1}{4}i\epsilon_\mathrm{R})}{\Gamma(\frac{1}{4}+\frac{1}{4}i\epsilon_\mathrm{L})} + \frac{E_{1\mathrm{R}}}{E_{1\mathrm{L}}} e^{-i\frac{3\pi}{4}} \frac{\Gamma(\frac{3}{4}-\frac{1}{4}i\epsilon_\mathrm{R})}{\Gamma(\frac{3}{4}+\frac{1}{4}i\epsilon_\mathrm{L})} \right] - \arg\left[\frac{\Gamma(\frac{1}{4}-\frac{1}{4}i\epsilon_\mathrm{R})}{\Gamma(\frac{1}{4}-\frac{1}{4}i\epsilon_\mathrm{L})} + \frac{E_{1\mathrm{R}}}{E_{1\mathrm{L}}} \frac{\Gamma(\frac{3}{4}-\frac{1}{4}i\epsilon_\mathrm{R})}{\Gamma(\frac{3}{4}-\frac{1}{4}i\epsilon_\mathrm{L})} \right], \quad (4.57)$$

and transmission and reflection coefficients which are calculated as

$$T(E) = \frac{E_{1\mathrm{R}}}{E_{1\mathrm{L}}} e^{-\frac{\pi}{4}(\epsilon_\mathrm{R}-\epsilon_\mathrm{L})} \left| \frac{e^{-i\frac{\pi}{4}} \frac{\Gamma(\frac{1}{4}-\frac{1}{4}i\epsilon_\mathrm{R})}{\Gamma(\frac{1}{4}+\frac{1}{4}i\epsilon_\mathrm{R})} - e^{-i\frac{3\pi}{4}} \frac{\Gamma(\frac{3}{4}-\frac{1}{4}i\epsilon_\mathrm{R})}{\Gamma(\frac{3}{4}+\frac{1}{4}i\epsilon_\mathrm{R})}}{\frac{\Gamma(\frac{1}{4}-\frac{1}{4}i\epsilon_\mathrm{R})}{\Gamma(\frac{1}{4}-\frac{1}{4}i\epsilon_\mathrm{L})} + \frac{E_{1\mathrm{R}}}{E_{1\mathrm{L}}} \frac{\Gamma(\frac{3}{4}-\frac{1}{4}i\epsilon_\mathrm{R})}{\Gamma(\frac{3}{4}-\frac{1}{4}i\epsilon_\mathrm{L})}} \right|^2, \quad (4.58)$$

$$R(E) = \left| \frac{e^{-i\frac{\pi}{4}} \frac{\Gamma(\frac{1}{4}-\frac{1}{4}i\epsilon_\mathrm{R})}{\Gamma(\frac{1}{4}+\frac{1}{4}i\epsilon_\mathrm{L})} + \frac{E_{1\mathrm{R}}}{E_{1\mathrm{L}}} e^{-i\frac{3\pi}{4}} \frac{\Gamma(\frac{3}{4}-\frac{1}{4}i\epsilon_\mathrm{R})}{\Gamma(\frac{3}{4}+\frac{1}{4}i\epsilon_\mathrm{L})}}{\frac{\Gamma(\frac{1}{4}-\frac{1}{4}i\epsilon_\mathrm{R})}{\Gamma(\frac{1}{4}-\frac{1}{4}i\epsilon_\mathrm{L})} + \frac{E_{1\mathrm{R}}}{E_{1\mathrm{L}}} \frac{\Gamma(\frac{3}{4}-\frac{1}{4}i\epsilon_\mathrm{R})}{\Gamma(\frac{3}{4}-\frac{1}{4}i\epsilon_\mathrm{L})}} \right|^2, \quad (4.59)$$

where the subscripts L and R here denote the left and right sides of the beamsplitter. When $\epsilon_\mathrm{R} = \epsilon_\mathrm{L} = \epsilon$, we can see that the above equations cancel to the symmetric case, as $\epsilon_{\mathrm{R/L}} = (E - V_0)/E^{\mathrm{sad}}_{\mathrm{L/R}}$.

We can introduce the parameter η, which describes the degree of asymmetry of the saddle, with $\eta = 0$ equivalent to the symmetric case above, and $\eta \to 1$ an extreme limit of asymmetry in which the beamsplitter all but closes on one side. This is chosen such that the mean width

$$\frac{1}{2}\left(E^{\mathrm{sad}}_\mathrm{L} + E^{\mathrm{sad}}_\mathrm{R}\right) = \frac{\hbar\left(\omega_\mathrm{L}^2 + \omega_\mathrm{R}^2\right)}{4\omega_c} = \frac{\hbar\omega_{\mathrm{BS}}}{2\omega_c}, \quad (4.60)$$

is independent of η and compares directly with the expression E_{sad} in the symmetric case. Here we use ω_L and ω_R, where $\hbar\omega_{\mathrm{L/R}}$ are the confinement energies on either side of the saddle. In the symmetric case we set $\omega_\mathrm{L} = \omega_\mathrm{R} = \omega_{\mathrm{BS}}$ and the L/R subscript can be dropped, however for the asymmetric case we set

$$\omega_\mathrm{L} = \sqrt{2}\omega_{\mathrm{BS}} \cos\left[\frac{1}{4}\pi(1+\eta)\right], \quad (4.61a)$$

$$\omega_\mathrm{R} = \sqrt{2}\omega_{\mathrm{BS}} \sin\left[\frac{1}{4}\pi(1+\eta)\right]. \quad (4.61b)$$

[2]The derivation of these phases was conducted by Sungguen Ryu, one of the coauthors of our paper, Ref. [39].

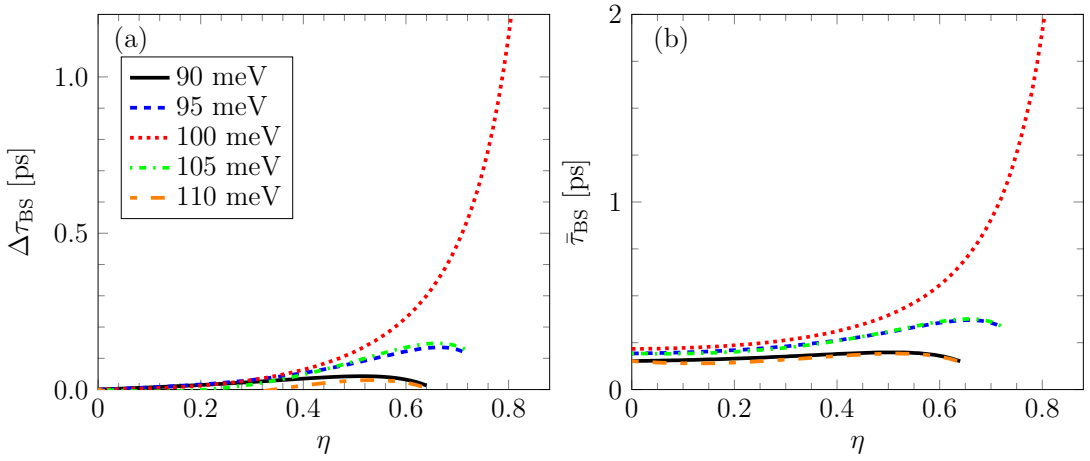

Figure 4.4: Panel (a) shows beamsplitter contribution to the difference in delay times $\Delta\tau_{\rm BS}$ as a function of beamsplitter asymmetry parameter η for various injection energies E_0. Panel (b) shows the corresponding mean beamsplitter delay time $\bar{\tau}_{\rm BS}$. The parameters here are $B = 11\,\mathrm{T}$, $\sigma_E = 1\,\mathrm{meV}$, $E_{\rm sad} = 100\,\mathrm{meV}$, $V_0 = 100\,\mathrm{meV}$ and $\hbar\omega_{\rm BS} = 20\,\mathrm{meV}$.

The energy range for which this model of the beamsplitter is valid is

$$\frac{|E - V_0|}{\hbar} \leq \left(\frac{d}{l_c}\right)^2 \frac{\omega_{BS}^2}{2\omega_c} \cos^2\left[\frac{\pi}{4}(\eta + 1)\right]. \tag{4.62}$$

Thus, as the degree of asymmetry increases, the region of validity decreases, and goes to zero for $\eta \to 1$. Fig. 4.4 shows the delay-time difference and the mean delay of the beamsplitters as a function of asymmetry for typical parameters and for several different values of E_0. We see that both these quantities have a very similar dependence on both η and E_0, with the main difference being that $\Delta\tau_{BS} \to 0$ for $\eta \to 0$ whereas $\bar{\tau}_{\rm BS}$ tends to the finite value of Eq. (4.55). For a given value of η, the delay difference is maximised when $E_0 = V_0$. As η increases, so does $\Delta\tau_{\rm BS}$ and, for $E_0 = V_0$ this time even diverges in the limit $\eta \to 1$.

The size of the delay difference determines the role that the beamsplitters play in the interference pattern. Taking an example of $\eta = 1/2$ with $E_0 = V_0 = E_{\rm peak} = 100\,\mathrm{meV}$ we obtain $\Delta\tau_{\rm BS} \approx 0.1\,\mathrm{ps}$. Since this is small compared with temporal width of the wave packet, $\sim 1\,\mathrm{ps}$, this level of asymmetry will not significantly affect the observed interference. In contrast, For larger asymmetries, e.g. $\eta = 3/4$, we find $\Delta\tau_{\rm BS} = 0.7\,\mathrm{ps}$ and since this is comparable with the temporal width, we can expect beamsplitter phases to be important here. Fig. 4.5 shows the energy-resolved arrival time distribution of an electron for two values of asymmetry: (a) $\eta = 1/2$ and (b) $\eta = 3/4$, with other parameters that match Fig. 4.2c (which may be thought of as the $\eta = 0$ case in this sequence). Fig. 4.5a shows that this level of asymmetry changes the arrival distribution very little, with the main effect being that the distribution becomes non-symmetric about $E_0 - V_0 = 0$. This stems from a corresponding asymmetry about V_0 in the transmission probability of the beamsplitters. Increasing η further, as in Fig. 4.5c, we observe that the interference pattern becomes significantly modified indicating that the beamsplitter phases here are playing a significant role in determining the details of the interference. We note that, for wider saddles [e.g. $\hbar\omega_{\rm BS} = 100\,\mathrm{meV}$ such as in Fig. 4.2a], the magnitude of $\Delta\tau^{\rm BS}$ is substantially less than observed here and the effect on the arrival time

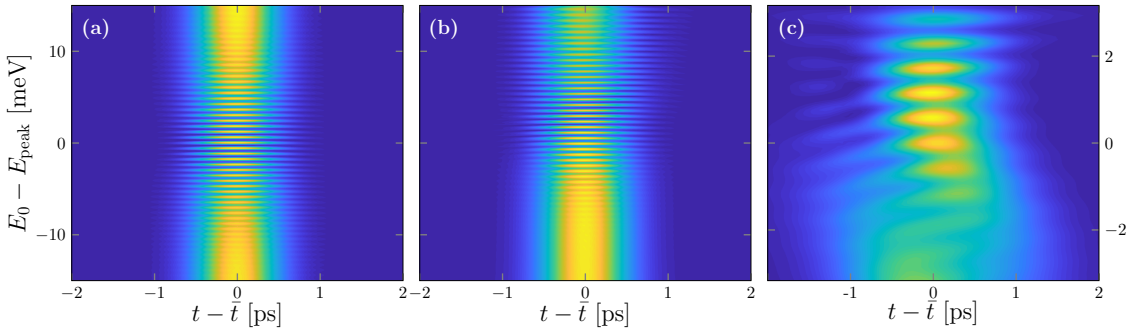

Figure 4.5: As Fig. 4.2c but here with asymmetric beamsplitters with asymmetry parameter: (a) $\eta = 0$, (b) $\eta = 1/2$, and (c) $\eta = 3/4$. The plot in (a) is the equivalent of using symmetric beamsplitters. Increasing the asymmetry first shifts the position of maximum visibility [as in (b)] and then at higher levels [as in (c)] modifies the interference pattern. The energy ranges used here are compatible with keeping the majority of the wave packet within the window defined by Eq. (4.62).

distributions for the same level of asymmetry is negligible.

4.8 Chapter summary

In this chapter we have derived a wavepacket picture of the interference in a hot-electron MZI, and focused on the energy-dependent arrival time distribution, as can be read out in experiment [74, 75]. We calculated the arrival time distribution of the electron wavepackets, investigating the effect of the width of the beamsplitters on these arrival times. First of all, we introduced a simplified model of the beamsplitter phases to get an idea of how they will affect the arrival time distributions. We have investigated what happens when the injection energy of the electron deviates from the energy for which the path lengths are optimised. The results of these numerical simulations clearly showed two lobes for the electrons arriving from the different paths. If the electron energy is not that for which the path lengths have been optimised, we see evidence that the electrons arrive at different times, meaning there is reduced or no interference observed between the lobes.

We have then included the complete beamsplitter phases, as seen in Ref. [39], in determining interference patterns. We found that for energetically wide beamsplitters, the size of visibility features is essentially determined by the single-particle coherence length Σ_l. The central energy of the beamsplitter has little effect on the arrival time for electrons in this case, as the electrons feel only a small percentage of the width, and therefore the same energy across the whole. Away from this limit, the transmission properties of the beamsplitters become important for determining the range of energy over which oscillations can be observed, as the beamsplitter is now of the same order of size as the electron itself. Looking at Fig. 3.4, we can see that if the wavepacket is approximately the same size as the beamsplitter, it will experience a range of energies, and therefore transmission and reflection coefficients. When modelling these systems, it is therefore important to include these beamsplitter phases and transmission and reflection coefficients in simulations to get a realistic view of what is happening. Concerning the contribution of the beamsplitters to the travel times and hence to phase averaging, if the beamsplitters are

symmetric or if they are asymmetric but alike and aligned, then they only contribute an overall delay to the arrival times, and no loss of visibility is observed. On the other hand, opposing asymmetries in the beamsplitters can affect both the quality and the structure of the interference patterns. However, we found that this only becomes relevant at rather high degrees of asymmetry.

We also calculated the visibility of the electrons from the arrival time distributions, and compared these to the analytic approximations for visibility. We found that for wide beamsplitters, the visibility is not affected by the central energy of the beamsplitter, V_0, however when the beamsplitter is narrower, the maximum visibility decreases with distance away from E_{peak}. Without the transmission and reflection coefficients included, we see that the phase averaging factor, $\mathcal{D}$ is a good model for the maximum visibility for values of $E_0 \neq E_{\text{peak}}$.

Part III

LO-phonon emission

Chapter 5

LO-phonons in electron quantum optics

In the same way that a photon is a quanta of light [90], a phonon is a quanta of sound waves. More specifically, they are the collective excitation of atoms in a crystalline structure [91]. In this chapter, I will describe the history of phonon emission in hot-electron quantum-optics experiments, before deriving some of the general tools that we will use in Chapter 6.

5.1 Phonons in condensed matter systems

Phonons come in two main categories: optical phonons and acoustic phonons. The type of phonon depends on the direction of its travel. If the atoms in the crystal are displaced in the same direction of propagation of the wave, it is known as an acoustic phonon, causing the atoms to behave in the same way as if a sound wave was passing through. If the atoms move out of phase with each other, this is known as an optical phonon, so named because in certain types of crystal, they can be excited by infrared radiation. While acoustic phonons are also relevant in single-electron systems [22, 24, 92, 54], this thesis will concentrate only on LO-phonons.

LO-phonons have different characteristic energies depending on the material of the system they are found in. In GaAs, they have an energy of 36 meV, and are approximately dispersionless [92], so they are easy to distinguish from other effects in experiments, as we will discuss in the next section.

5.2 Experimental observations

In 2011, the relaxation mechanisms of electrons above the Fermi level were investigated in detail by Taubert *et al.* [92]. In their paper, they investigate multiple relaxation methods, including electron-phonon interactions. Their experiments, conducted for a range of magnetic fields, found that as the magnetic field increases, the role of LO-phonon emission in electron relaxation becomes dominant. This is actually the opposite to the results of the 2013 study by Fletcher *et al.*, who set out to investigate experimentally the detection of electrons emitted at energies around 150 meV above the Fermi level [74], and found that for the higher magnetic fields, evidence of LO-phonon emission is absent. It should, however, be noted that the

experiments of the latter were conducted in a magnetic field range much higher than those in the former, which means direct comparison is not possible [74].

Both sets of experiments were performed in a GaAs/AlGaAs 2DEG such as that described in part I [92, 74]. In Ref. [74], electrons were pumped from the source and then detected 3μm away. These experiments were performed at two magnetic fields, $B = 6$ T and $B = 12$ T. At the higher of the two magnetic fields, a distinct peak shows the arrival of electrons with an energy that increases linearly with the voltage of the input gate [74], however, for the lower magnetic field, $B = 6$ T, there are further peaks observed at multiple integers of 36 meV below the injection energy. This is evidence of LO-phonon emission, as LO-phonons in GaAs are known to have an energy of 36 meV, so each "phonon replica", as they are thus referred to, represents an electron detected after having emitted one or more LO-phonons.

Since these experiments detecting the presence of LO-phonon emission, more have been conducted specifically to investigate the rate at which LO-phonons are emitted [24]. The study in Ref. [24] is a detailed investigation into the effect of electron energy, edge-potential profile and and magnetic field on the rate of emission of LO phonons. Particularly interesting is the effect of the magnetic field on the emission rate, given the discrepencies in the experiments discussed previously [74, 92]. It was here found that the higher the magnetic field, the lower the rate of emission of the LO phonons, although emission was still observed at $B = 12$ T, unlike in [74] which was performed at much higher energies than Ref. [24]. It is thought that the reason for this discrepency is that the behaviour changes between the regimes the two papers studied, and so the same behaviour could not be seen in both.

Ota *et al.* performed a full experimental investigation into the different mechanisms for relaxation in a single-electron system [25]. Their results very clearly showed that for low energies, plasmon emission and other electron-electron interactions are dominant. These Coulomb interactions are then suppressed with increasing energy, leading to near ballistic motion of the electrons, up to higher energies around 150 meV, at which point the dominant mechanism becomes LO-phonon emission, as indicated by the presence of phonon-replicas at integer multiples of 36 meV below the injection energy, which is seen in Ref. [74].

5.3 Theoretical background

In 2016, Emary *et al.* [23] considered the effect of LO phonon emission on the relaxation rates of single electrons in quantum Hall edge channels. The electron-phonon interactions are described using the Fröhlich Hamiltonian [93, 94], which is the method that has been adopted in this thesis. The Fröhlich Hamiltonian takes the Hamiltonians describing electrons and phonons individually, and the interaction Hamiltonian between the two, and combines these elements to describe the overall interaction between electrons and phonons. The Hamiltonian for the electrons is given by

$$H_e = \Sigma_{\mathbf{n}} \hbar\omega_{\mathbf{n}} c^\dagger_{\mathbf{n}} c_{\mathbf{n}}, \tag{5.1}$$

where $c_{\mathbf{n}}$ and $c_{\mathbf{n}}^{\dagger}$ are the annihilation and creation operators for an electron. The phonon Hamiltonian is written as

$$H_p = \sum_{\mathbf{q}} \hbar\omega_{LO} a_{\mathbf{q}}^{\dagger} a_{\mathbf{q}}, \tag{5.2}$$

where $\hbar\omega_{LO}$ is the energy of the LO-phonons and $a_{\mathbf{q}}^{\dagger}$ and $a_{\mathbf{q}}$ are the annihilation and creation operators for an LO-phonon. The Hamiltonian for the interaction between the electrons and phonons is

$$H_{e-ph} = \sum_{\mathbf{n}} \sum_{\mathbf{q}} \Lambda_{\mathbf{n'n}} c_{\mathbf{n'}}^{\dagger} c_{\mathbf{n}} \left(a_{\mathbf{q}} + a_{-\mathbf{q}}^{\dagger} \right) \tag{5.3}$$

These are derived fully in the next section.

It was found that the phonon scattering rate as a function of magnetic field drops approximately exponentially, with the drop being significantly steeper at low injection energies (50 meV) than high (150 meV) [23] (we can see this in our later plots in Fig. 6.1 (a)). This is understandable in that LO phonons can only be emitted if the electron is of a high enough energy in the first place, so for higher energy electrons, it is possible for more phonons to be emitted than for lower energy electrons.

It was in comparison with the theory in this paper that Johnson *et al.* [24] noticed that in certain regimes, the rates derived in Ref. [23] were in fact several orders of magnitude too small [24]. This suggested that there was something else missing from the story, which was later found to be scattering between Landau levels due to the emission of acoustic phonons [24]. These are not something which will be considered in this thesis, but they are an interesting phenomenon nonetheless. The theory of this emission was studied by Emary *et al.* [54] in 2019. It was found that acoustic phonons are suppressed at higher energies, due to the speed of the electron through the system, however it is at these higher energies that LO-phonons become the dominating effect. The emission rate of acoustic phonons also depends significantly on the strength of the confinement in the z-direction, and can be suppressed by using a wider well, which does not affect the rate of emission of LO-phonons as strongly as acoustic phonons, thereby avoiding having to increase the effect of LO-phonon in order to reduce the acoustic [23, 54]. In 2020, Clark *et al.* described multiple decoherence mechanisms in a single-electron system, with the goal of finding optimum experimental conditions which mitigate the decoherence as much as possible [22].

In part II of this thesis, we found optimal regions for reducing the dephasing due to phase averaging. We can therefore use this in conjunction with Ref. [22] to determine the optimal conditions for experiments. The LO-phonon rates were calculated using only the diagonal-terms of the master equation, and the inter-arm coherence was considered, however the intra-arm coherences were not taken into account, which is the addition made in this thesis. The results of Ref. [22] show that the dephasing and incoherent effects do not all vary with magnetic field and injection energy in the same way, meaning that there has to be some trade off between the different sources of decoherence. This means that one mechanism cannot be suppressed by increasing a parameter without subsequently increasing the effect of another, including LO-phonon emission [22]. In fact, if we compare the results of this paper with those found in part II of this thesis, we see that the range

of energies for which dephasing due to phase averaging is suppressed is the greatest when the magnetic field is low, however in Ref. [22], low magnetic fields actually increase the effect on dephasing of LO phonons (as calculated using the semiclassical rates and no intra-arm coherences).

The 2016 paper is a theoretical approach to calculating the emission rates of LO phonons, describing the behaviour of electrons after emission semi-classically [23]. In order to calculate a complete quantum picture, one must also consider the coherence of the electrons, which is the addition made in this thesis.

5.4 Fröhlich Hamiltonian

In this Part of this thesis, we will be deriving a fully-quantum master equation to describe the behaviour of electrons undergoing LO-phonon emission. We will describe this behaviour using the Fröhlich Hamiltonian [93], which we will briefly derive in this section, following the methods set out in Refs. [94, 95].

Phonons in a semiconductor are the group wave motion of the ions in the semiconductor. To first order, the wavefunction of the coupling between electrons and ions is given as $\Psi(\mathbf{r};\mathbf{R}) = \chi(\mathbf{R})\psi(\mathbf{r};\mathbf{R})$, which obeys the Schrödinger equation

$$H_{e-i}(\mathbf{R})\psi_n(\mathbf{r};\mathbf{R}) = E_n(\mathbf{R})\psi_n(\mathbf{r};\mathbf{R}). \tag{5.4}$$

Here, $\mathbf{r}$ is the position of the electron, $\mathbf{R}$ is the position of the ion, and H_{e-i} is the Hamiltonian describing the interaction between the electron and the ion.

When the ions in the semiconductor are displaced such that $\mathbf{R} = \mathbf{R}_0 + \mathbf{u}$, where u is the displacement, the electrons feel a change in potential, V, where V^0 is the potential due to only the electron-ion interaction. This linear change in potential is then given as

$$\delta_{\mathbf{R}} V = \mathbf{u} \cdot \nabla V^0\big|_{\mathbf{R}_0} \tag{5.5}$$

In semiconductors, however, the electrons in the bulk are not isolated, such that any interaction between one electron with the ions is also affected by interactions between all of the other electrons and ions in the system. This can be dealt with by introducing a screening term into Eq. (5.5). The measure of screening here is the inverse dielectric constant, ϵ [96, 97], such that

$$\delta_{\mathbf{R}} V = \mathbf{u} \cdot \epsilon^{-1} \nabla V^0\big|_{\mathbf{R}_0}. \tag{5.6}$$

We now have an equation describing the change in potential felt by an electron in an electron-ion interaction. The next step in deriving the Fröhlich Hamiltonian, is to decide what it is that we want to consider. We're looking for a Hamiltonian to describe the interaction between an electron and a phonon, which comes from the equation we have just derived. In its simplest form, the Fröhlich Hamiltonian looks like

$$H = H_e + H_{ph} + H_{e-ph}, \tag{5.7}$$

where H_e is the Hamiltonian describing the electron, H_{ph} is the Hamiltonian describing the phonon, and H_{e-ph} is the Hamiltonian describing the interaction between the two. The next step, then, is to define these terms, so that we can combine them to give the Fröhlich Hamiltonian.

The Hamiltonian for an electron, in its most general form is

$$H_e = \sum_{\mathbf{k}\nu\sigma} E_{\mathbf{k}\nu} c^\dagger_{\mathbf{k}\nu\sigma} c_{\mathbf{k}\nu\sigma} \tag{5.8}$$

where $E_{\mathbf{k}\nu\sigma}$ is the band energy, $c^\dagger_{\mathbf{k}\nu\sigma}$ and $c_{\mathbf{k}\nu\sigma}$ are the creation and annihilation operators for an electron in the state where $\mathbf{k}$ is the momentum, ν is the band index and σ is the spin. We can describe phonons using the simple harmonic oscillator, such that the Hamiltonian is

$$H_{ph} = \sum_{\mathbf{q}j} \hbar\omega_{\mathbf{q}j} \left(a^\dagger_{\mathbf{q}j} a_{\mathbf{q}j} + \frac{1}{2} \right) \tag{5.9}$$

where $a^\dagger_{\mathbf{q}j}$ and $a_{\mathbf{q}j}$ are the creation and annihilation operators of phonons for which $\mathbf{q}$ is the momentum and j is the branch index and $\hbar\omega_{\mathbf{q}j}$ is the energy.

The creation and annhilation operators for a quantum harmonic oscillator as describes the phonons are [94]

$$a^\dagger_{\mathbf{q}} = \sqrt{\frac{m\omega_{\mathbf{q}}}{2\hbar}} \left(\hat{x}_{\mathbf{q}} + \frac{i}{m\omega_{\mathbf{q}}} \hat{p}_{-\mathbf{q}} \right) \tag{5.10}$$

$$a_{\mathbf{q}} = \sqrt{\frac{m\omega_{\mathbf{q}}}{2\hbar}} \left(\hat{x}_{\mathbf{q}} - \frac{i}{m\omega_{\mathbf{q}}} \hat{p}_{-\mathbf{q}} \right) \tag{5.11}$$

where $\hat{x_{\mathbf{q}}}$ and $\hat{p}_{-\mathbf{q}}$ are the position and momentum operators respectively. We can see from this that the sum of the creation and annihilation operators is proportional to only the position operator, $\hat{x_{\mathbf{q}}}$,

$$a^\dagger_{\mathbf{q}j} + a_{\mathbf{q}j} = \sqrt{\frac{2m\omega_{\mathbf{q}j}}{\hbar}} \hat{x}_{\mathbf{q}j} \tag{5.12}$$

We then need the operator of atom displacements, which can be obtained from the solid state properties of the materials. In the electron-phonon system, these are given as the sum total of the equilibrium position $A^{\mathbf{q}j}_{s\alpha}$ multiplied by the position operator, written in terms of the creation and annihilation operators

$$u_{ls\alpha} = e^{i\mathbf{q}\mathbf{R}^0_{ls}} \frac{1}{\sqrt{N_{\mathbf{q}}}} \sum_{\mathbf{q}j} A^{\mathbf{q}j}_{s\alpha} \left(a_{\mathbf{q}j} + a^\dagger_{-\mathbf{q}j} \right) \tag{5.13}$$

where

$$A^{\mathbf{q}j}_{s\alpha} = \eta_{s\alpha}(\mathbf{q}j) \sqrt{\frac{\hbar}{2m_s\omega_{\mathbf{q}j}}} \tag{5.14}$$

Here, the indices l, s denote the unit cell and atoms inside the unit cell, respectively, and η is the eigenvector of the normal mode $\mathbf{q}j$. The coupling constant for the electrons and phonons can be determined using Eq. (5.6) and Eq. (5.13), as

$$\Lambda^{\mathbf{k}+\mathbf{q}\nu',\mathbf{k}\nu}_{\mathbf{q}j} = \sum_{s\alpha} A^{\mathbf{q}j}_{s\alpha} \langle \mathbf{k}+\mathbf{q}\nu'\sigma | \delta^{\mathbf{q}}_{s\alpha} V | \mathbf{k}\nu\sigma \rangle \tag{5.15}$$

From Eq. (5.6) we then obtain the full equation for the electron-phonon interaction Hamiltonian,

$$H_{e-ph} = \sum_{\mathbf{k}\nu\nu'\sigma} \sum_{\mathbf{q}j} \Lambda^{\mathbf{k}+\mathbf{q}\nu',\mathbf{k}\nu}_{\mathbf{q}j} c^\dagger_{\mathbf{k}+\mathbf{q}\nu'\sigma} c_{\mathbf{k}\nu'\sigma} \left(a_{\mathbf{q}j} + a^\dagger_{-\mathbf{q}j} \right) \tag{5.16}$$

These are the components necessary for the Fröhlich Hamiltonian as we will be using it for the rest of this thesis.

5.5 General Master Equation

In this section we will derive a general master equation to which we will later use to derive the master equation for our specific system. Here we follow the method set out in Ref. [98]. To derive our master equation we will work in the interaction picture. The interaction picture is used when we do not want to look at any free evolution of the state, only interactions, such that both the state vectors and the operators concerned have a time dependence, unlike the Schrödinger and Heisenberg pictures which have time dependence in only the state vectors or the operators respectively. The interaction and Schrödinger pictures are related as to enter the interaction picture, we can split a Hamiltonian in the Schrödinger picture into two components, $H_S = H_{0,S} + H_{1,S}$. Usually, we choose to split the Hamiltonian such that $H_{0,S}$ contains only the time independent terms and $H_{1,S}$ contains the time dependent terms.

We define $H \equiv H_0 + V$ as the Hamiltonian where $H_0 \equiv H_S + H_B$ is the Hamiltonian of the uncoupled "system" (H_S) and "bath" (H_B) Hamiltonians, and $V \equiv H_{SB}$ is the perturbation which describes the interaction between the two. The full Hamiltonian is therefore $H = H_S + H_B + H_{SB}$

We will consider the description as two parts; one that we are interested in, which is the system, and one that we want to separate the system from, which is the bath. In our case the system is the electrons and the bath is the LO-phonons. We aren't interested in the behavious of the LO-phonons themselves, but we are interested in their interaction with the system, our electrons. To do this, we need to derive a description which takes into account only the system information, using the Hamiltonians above.

To describe the system we also need a density matrix, χ, that describes the full system and bath, and obeys the Liouville-von-Neumann equation,

$$\frac{d}{dt}\chi(t) = -\frac{i}{\hbar}[H, \chi(t)] \tag{5.17}$$

$$\Rightarrow \chi(t) = e^{-iHt/\hbar}\chi(t=0)e^{iHt/\hbar}. \tag{5.18}$$

Here, $\chi(t=0)$ is our initial condition at $t = 0$.

We need to convert this density operator from the Schrödinger picture to the interaction picture. To move between the two, we can use the relationship

$$\tilde{\chi}(t) \equiv e^{iH_0t/\hbar}\chi(t)e^{-iH_0t/\hbar} \tag{5.19}$$

We can now find the equation of motion for the density operator in the interaction picture. To do this we need to apply Eq. (5.19) to Eq. (5.18) and move through time

$$\begin{aligned}\frac{d}{dt}\tilde{\chi}(t) &= \left[\frac{\mathrm{d}}{\mathrm{d}t}e^{iH_0t/\hbar}\right]\chi(t)e^{-iH_0t/\hbar} + e^{uH_0t/\hbar}\left[\frac{\mathrm{d}}{\mathrm{d}t}\chi(t)\right]e^{-iH_0t/\hbar} + e^{iH_0t/\hbar}\chi(t)\left[\frac{\mathrm{d}}{\mathrm{d}t}e^{-iH_0t/\hbar}\right], \\ &= \frac{iH_0}{\hbar}e^{iH0t/\hbar}\chi(t)e^{-iH_0t/\hbar} + e^{iH_0t/\hbar}\left[\frac{\mathrm{d}}{\mathrm{d}t}\chi(t)\right]e^{-iH_0t/\hbar} - \frac{i}{\hbar}e^{iH_0t/\hbar}\chi(t)\left[H_0e^{-iH_0t/\hbar}\right].\end{aligned} \tag{5.20}$$

We can use the definition of the commutator and Eq. (5.19) to simplify this to

$$\frac{d}{dt}\tilde{\chi}(t) = \frac{i}{\hbar}[H_0, \tilde{\chi}(t)] + e^{iH_0t/\hbar}\frac{d}{dt}\chi(t)e^{-iH_0t/\hbar} \tag{5.21}$$

Now we can use Eq. (5.17) and the definitions above of $H \equiv H_0 + V$ and $H_0 \equiv H_S + H_B$ to give

$$\begin{aligned}\frac{d}{dt}\tilde{\chi}(t) &= \frac{i}{\hbar}[H_0, \tilde{\chi}(t)] - ie^{iH_0t/\hbar}[H, \chi(t)]e^{-iH_0t/\hbar} && (5.22)\\ &= \frac{i}{\hbar}[H_0, \tilde{\chi}(t)] - ie^{iH_0t/\hbar}[H_0 + V, \chi(t)]e^{-iH_0t/\hbar}\\ &= \frac{i}{\hbar}[H_0, \tilde{\chi}(t)] - \frac{i}{\hbar}[H_0 + \tilde{V}(t), \tilde{\chi}(t)]\\ &= -\frac{i}{\hbar}[\tilde{V}(t), \tilde{\chi}(t)]. && (5.23)\end{aligned}$$

we can integrate this, to give

$$\tilde{\chi}(t) = \chi(t=0) - i\int_0^t \mathrm{d}t' \left[\tilde{V}(t'), \tilde{\chi}(t')\right], \tag{5.24}$$

which we can then insert back in to Eq. (5.23), which gives us

$$\begin{aligned}\frac{d}{dt}\tilde{\chi}(t) &= -\frac{i}{\hbar}\left[\tilde{V}(t), \left\{\chi(t=0) - i\int_0^t \mathrm{d}t' \left[\tilde{V}(t'), \tilde{\chi}(t')\right]\right\}\right] && (5.25)\\ &= -\frac{i}{\hbar}\left\{\tilde{V}(t)\chi(t=0) - i\int_0^t \mathrm{d}t' \left[\tilde{V}(t'), \tilde{\chi}(t')\right]\right. && (5.26)\\ &\qquad \left. -\chi(t=0) - i\int_0^t \mathrm{d}t' \left[\tilde{V}(t'), \tilde{\chi}(t')\right]\tilde{V}(t)\right\} && (5.27)\\ &= -\frac{i}{\hbar}[\tilde{V}(t), \chi(t=0)] - \int_0^\infty \mathrm{d}t'[\tilde{V}(t), [\tilde{V}(t'), \tilde{\chi}(t')]] && (5.28)\end{aligned}$$

Now that we have our equation of motion for the density matrix for the initial conditions, we want to find the effective density matrix of the system only, which is the bit we're interested in i.e. the electrons. We can do this by taking the trace over the bath of the density matrix, $\rho(t) \equiv \mathrm{Tr}_B[\chi(t)]$. To do this, we must first introduce the Born Approximation and the Bath Correlation functions.

5.5.1 Born approximation

The Born approximation is the assumption that the interaction between the bath and system is weak, so that any influence on the bath is small, and can therefore be treated as a constant [99]. This can be written as

$$\tilde{\chi}(t') \approx R_0 \otimes \tilde{\rho}(t') \tag{5.29}$$

where $\tilde{\rho}$ is the density matrix describing the system in the interaction picture. We assume a thermal equilibrium for the bath, i.e.

$$R_0 = \frac{e^{-\beta H_B}}{\mathrm{Tr}\, e^{-\beta H_B}}, \tag{5.30}$$

where $\beta = 1/k_BT$. We are working at zero temperature, so as $T \to 0, \beta \to \infty$, which means that $R_0 \to |0\rangle\langle 0|$. Eq. (5.28) therefore becomes

$$\frac{d}{dt}\tilde{\rho}(t) = -\frac{i}{\hbar}\,\mathrm{Tr}_B\left[\tilde{V}(t), R_0 \otimes \tilde{\rho}(t=0)\right] - \int_0^t \mathrm{d}t'\,\mathrm{Tr}_B\left[\tilde{V}(t), \left[\tilde{V}(t'), R_0 \otimes \tilde{\rho}(t')\right]\right] \tag{5.31}$$

We can denote our system operators as S_α and bath operators B_α, such that

$$V = \sum_\alpha S_\alpha \otimes B_\alpha. \tag{5.32}$$

We can input this into Eq. (5.31), to give

$$\frac{d}{dt}\tilde{\rho}(t) = -\frac{i}{\hbar}\sum_{\alpha_1} \mathrm{Tr}_B \left[\tilde{S}_{\alpha_1}(t)\tilde{B}_{\alpha_1}(t), R_0 \otimes \rho(t=0)\right] - \int_0^t \mathrm{d}t' \sum_{\alpha_1\alpha_2} \mathrm{Tr}_B \left[\tilde{S}_{\alpha_1}(t)\tilde{B}_{\alpha_1}(t), \left[\tilde{S}_{\alpha_2}(t')\tilde{B}_{\alpha_2}(t'), R_0 \otimes \tilde{\rho}(t')\right]\right] \tag{5.33}$$

We can now make some assumptions in order to simplify our master equation. We assume that the inital state, $\rho(t=0)$ represents an interaction which generates no first order dynamics in the bath. If the bath term creates or destroys anything, the trace over the bath will be zero, so there are only non-zero first order terms if there is a system interaction coupled with the bath. The first term therefore disappears. Now we need only concentrate on the integral term. Evaluating the commutator within the integral gives

$$\frac{d}{dt}\tilde{\rho}(t) = -\int_0^t \mathrm{d}t' \sum_{\alpha_1\alpha_2} \Big\{ \mathrm{Tr}\left[\tilde{B}_{\alpha_1}(t)\tilde{B}_{\alpha_2}(t')R_0\right] \tilde{S}_{\alpha_1}(t)\tilde{S}_{\alpha_2}(t')\tilde{\rho}(t') - \mathrm{Tr}\left[\tilde{B}_{\alpha_1}(t)R_0\tilde{B}_{\alpha_2}(t')\right] \tilde{S}_{\alpha_1}(t)\tilde{\rho}(t')\tilde{S}_{\alpha_2}(t') - \mathrm{Tr}\left[\tilde{B}_{\alpha_2}(t')R_0\tilde{B}_{\alpha_1}(t)\right] \tilde{S}_{\alpha_2}\tilde{\rho}(t')\tilde{S}_{\alpha_1}(t) + \mathrm{Tr}\left[R_0\tilde{B}_{\alpha_2}(t')\tilde{B}_{\alpha_1}(t)\right] \tilde{\rho}(t')\tilde{S}_{\alpha_2}(t')\tilde{S}_{\alpha_1}(t)\Big\} \tag{5.34}$$

This form of the master equation is still quite unwieldy; however, by introducing the bath correlation functions, we can trace over the bath terms to further simplify the equation.

5.5.2 Bath correlation functions

We can now introduce the bath correlation functions,

$$C_{\alpha_1\alpha_2}(t,t') \equiv \mathrm{Tr}_B \left[\tilde{B}_{\alpha_1}(t)\tilde{B}_{\alpha_2}(t')R_0\right], \tag{5.35}$$

and

$$C_{\alpha_2\alpha_1}(t',t) \equiv \mathrm{Tr}_B \left[\tilde{B}_{\alpha_2}(t')\tilde{B}_{\alpha_1}(t)R_0\right]. \tag{5.36}$$

We can assume that for a bath in equilibrium $[R_0, H_B] = 0$, so

$$C_{\alpha_1\alpha_2}(t,t') \equiv C_{\alpha_1\alpha_2}(t-t'), \tag{5.37}$$

and

$$C_{\alpha_2\alpha_1}(t',t) \equiv C_{\alpha_2\alpha_1}(t'-t) \tag{5.38}$$

We can now rewrite Eq. (5.34) as

$$\frac{d}{dt}\tilde{\rho}(t) = -\int_0^t \mathrm{d}t' \sum_{\alpha_1\alpha_2} \Big\{ C_{\alpha_1\alpha_2}(t-t') \left[\tilde{S}_{\alpha_1}(t)\tilde{S}_{\alpha_2}(t')\tilde{\rho}(t') - \tilde{S}_{\alpha_2}\tilde{\rho}(t')\tilde{S}_{\alpha_1}(t)\right] + C_{\alpha_2\alpha_1}(t'-t) \left[\tilde{\rho}(t')\tilde{S}_{\alpha_2}(t')\tilde{S}_{\alpha_1}(t) - \tilde{S}_{\alpha_1}(t)\tilde{\rho}(t')\tilde{S}_{\alpha_2}(t')\right]\Big\} \tag{5.39}$$

In order to deal with the bath correlation functions mathematically, we can introduce another approximation.

5.5.3 Markov approximation

The Markov approximation assumes that the bath correlation function is strongly peaked around $\tau \equiv t - t' \simeq 0 \Rightarrow t \simeq t'$, with a peak width of $\delta\tau$, and that this peak width is much smaller than the rate of change of $\tilde{\rho}(t')$. We can then say that for $\tilde{\rho}$ in the interaction picture, $t = t'$, so we can replace $\tilde{\rho}(t')$ with $\tilde{\rho}(t)$ within the integral.

The Markov approximation is valid in the case where the decay rate is small enough such that the time scale introduced for the integration is large enough that the correlation functions are sharply peaked. Interestingly, this has to be verified *a posteriori*, so we will ensure the consistency of the approximation after seeing the end results.

Later we will be calculating the equation of motion for the travelling wave, so we can now move from the interaction picture back into the Schrödinger picture, using the relation

$$\frac{d}{dt}\tilde{\rho}(t) = \frac{i}{\hbar}\left[H_S, \tilde{\rho}(t)\right] + e^{iH_S t/\hbar}\frac{d}{dt}\rho(t)e^{-iH_S t/\hbar} \tag{5.40}$$

$$\Rightarrow \frac{d}{dt}\rho(t) = -\frac{i}{\hbar}\left[H_S, \rho(t)\right] + e^{-iH_S t/\hbar}\frac{d}{dt}\tilde{\rho}(t)e^{iH_S t/\hbar}. \tag{5.41}$$

such that

$$\begin{aligned}\frac{d}{dt}\rho(t) = &-\frac{i}{\hbar}\left[H_S, \rho(t)\right] \\ &- \int_0^t \mathrm{d}t' \sum_{\alpha_1\alpha_2} \Big\{ C_{\alpha_1\alpha_2}(t-t')\left[S_{\alpha_1}\tilde{S}_{\alpha_2}(t'-t)\rho(t) - \tilde{S}_{\alpha_2}(t'-t)\rho(t)S_{\alpha_1}\right] \\ &\qquad + C_{\alpha_2\alpha_1}(t'-t)\left[\rho(t)\tilde{S}_{\alpha_2}(t'-t)S_{\alpha_1} - S_{\alpha_1}\rho(t)\tilde{S}_{\alpha_2}(t'-t)\right]\Big\}\end{aligned} \tag{5.42}$$

Due to the sharp peak, the integral $[0, t] \approx [0, \infty]$, as the function is highly localised in time. We can now define

$$D_{\alpha_1} \equiv \lim_{t\to\infty}\int_0^t \mathrm{d}\tau \sum_{\alpha_2} C_{\alpha_1\alpha_2}(\tau)\tilde{S}_{\alpha_2}(-\tau) \tag{5.43}$$

$$E_{\alpha_1} \equiv \lim_{t\to\infty}\int_0^t \mathrm{d}\tau \sum_{\alpha_2} C_{\alpha_2\alpha_1}(-\tau)\tilde{S}_{\alpha_2}(-\tau) \tag{5.44}$$

where $\tau = t - t'$ as above. This allows us to write our master equation in the simplified form

$$\frac{d}{dt}\rho(t) = -\frac{i}{\hbar}\left[H_S, \rho(t)\right] - \sum_{\alpha_1}\left[S_{\alpha_1}D_{\alpha_1}\rho(t) - D_{\alpha_1}\rho(t)S_{\alpha_1} + \rho(t)E_{\alpha_1}S_{\alpha_1} - S_{\alpha_1}\rho(t)E_{\alpha_1}\right] \tag{5.45}$$

This is the general master equation which we will use in the next chapter, inputting the specific Hamiltonians for the electron system that we are considering.

5.6 Chapter summary

In the following chapter I will use the general master equation above derive a fully quantum master equation to describe the dynamics of the electrons undergoing loss

via LO-phonon emission. To do this, I will calculate the rates using the method in Ref. [23], with the addition that I will now also consider the off-diagonal rates in the master equation. I will also use the Fröhlich Hamiltonian for LO-phonon emission [23, 93, 94] in the interaction picture to describe the behaviour of the electron, again keeping the off-diagonal terms of the density matrix which describe the coherence of the electron as well as the population.

Chapter 6

Fully-quantum description of LO-phonon emission

We derive a fully quantum master equation to describe the dissipation experienced by a single electron upon emitting an LO-phonon. We will use a Fermi's Golden Rule approach to calculate the rate of phonon emission, and then derive the master equation using the Fröhlich Hamiltonian, including both the diagonal (population) and off diagonal (coherence) terms of the density matrix. Previous approaches have considered only the population terms, making them semi-classical explanations of electron behaviour under phonon emission [23]. The inclusion of the coherence terms here completes the picture of the quantum behaviour.

In order to derive the equation, we will start with the system and bath Hamiltonians and move into the interaction picture as we want to concentrate only on the system and the interaction of the system with the bath. We will then use the Born approximation and the Markov approximation in order to reduce the complexity of the master equation and make it solvable. After this we will calculate the rate of emission of the LO-phonons and compare to the semiclassical case as seen in Ref. [23].

Once we have a fully quantum master equation including the rate of emission, in Sec. 6.5 we will present solutions to a subensemble of the dynamics that undergoes no-phonon emission by considering an unravelling of the dynamics of the previously determined master equation. We will also see the numerical solution for the conditional dynamics in order to visualise the decay of an electron under these circumstances.

In experiments it is generally the electrons that have not emitted a phonon that we are interested in detecting as they are still coherent, so for this thesis we will concentrate on examining the dynamics of this case.

6.1 Master equation for LO phonon emission

Now that we have the general form of the master equation we can input the specific bath and system Hamiltonians for our system, i.e. the LO-phonon bath and the electron system derived in Chapter 5. For $\mathbf{n} = \{m, n, k\}$, the system Hamiltonian is

$$H_S = \sum_{\mathbf{n}} \hbar\omega_{\mathbf{n}} c^\dagger_{\mathbf{n}} c_{\mathbf{n}}, \tag{6.1}$$

and the bath Hamiltonian is

$$H_B = \sum_q \hbar\omega_{\mathrm{LO}} a_q^\dagger a_q, \tag{6.2}$$

where $q = |\mathbf{q}|$, and $\mathbf{q}$ is the three-dimensional wave vector of the bulk LO-phonons. The interaction term can then be given in terms of the system and bath operators, S_α and B_α as we saw in Sec. 5.5,

$$\begin{aligned} H_{SB} &= \sum_\alpha S_\alpha \otimes B_\alpha \\ &= \sum_{\mathbf{nn'}} c_{\mathbf{n'}}^\dagger c_{\mathbf{n}} \sum_{\mathbf{q}} \Lambda_{\mathbf{n'n}}(\mathbf{q})(a_{-\mathbf{q}}^\dagger + a_{\mathbf{q}}), \end{aligned} \tag{6.3}$$

where $\alpha = \{\mathbf{nn'}\}$. We also have that $a_{\mathbf{q}}$ is the annihilation operator for these phonons and $\Lambda_{\mathbf{n'n}}$ is the matrix element from the Fröhlich Hamiltonian, Eq. (5.16) [94, 95], and in full is [23]

$$\Lambda_{\mathbf{n'n}}(\mathbf{q}) = \sum_{\mathbf{p}} M(\mathbf{q}) \left\langle \Psi_{\mathbf{n'}} | \mathbf{p} + \mathbf{q} \right\rangle \left\langle \mathbf{p} | \Psi_{\mathbf{n}} \right\rangle, \tag{6.4}$$

where

$$M(\mathbf{q}) = \frac{M_0}{\sqrt{V}} \frac{1}{|\mathbf{q}|}, \tag{6.5}$$

and

$$M_0^2 = 4\pi\alpha\hbar \frac{(\hbar\omega_{\mathrm{LO}})^{3/2}}{(2m_e^*)^{1/2}}. \tag{6.6}$$

This we will evaluate more precisely later in Sec. 6.3. We can split our interaction term into the system operators and the bath operators. We have B_{α_1} and B_{α_2}, S_{α_1} and S_{α_2}, defined as

$$S_{\alpha_1} = c_{\mathbf{n}_1'}^\dagger c_{\mathbf{n}_1}, \tag{6.7a}$$

$$S_{\alpha_2} = c_{\mathbf{n}_2'}^\dagger c_{\mathbf{n}_2}, \tag{6.7b}$$

$$B_{\alpha_1} = \sum_{\mathbf{q}_1} \Lambda_{\mathbf{n}_1'\mathbf{n}_1}(\mathbf{q}_1)(a_{-\mathbf{q}_1}^\dagger + a_{\mathbf{q}_1}), \tag{6.7c}$$

$$B_{\alpha_2} = \sum_{\mathbf{q}_2} \Lambda_{\mathbf{n}_2'\mathbf{n}_2}(\mathbf{q}_2)(a_{-\mathbf{q}_2}^\dagger + a_{\mathbf{q}_2}). \tag{6.7d}$$

As we are looking at the interaction of phonons and electrons, we will work in the interaction picture. An operator in the Schrödinger picture can be transformed to the interaction picture using

$$A_I(t) = e^{iH_{0,S}t/\hbar} A_S e^{-iH_{0,S}t/\hbar}. \tag{6.8}$$

The time dependent operators for our system in the interaction picture then become

$$\tilde{S}_{\alpha_1}(t) = c_{\mathbf{n}_1'}^\dagger e^{i\omega_{\mathbf{n}_1'}t} c_{\mathbf{n}_1} e^{-i\omega_{\mathbf{n}_1}t}, \tag{6.9a}$$

$$\tilde{S}_{\alpha_2}(t) = c_{\mathbf{n}_2'}^\dagger e^{i\omega_{\mathbf{n}_2'}t'} c_{\mathbf{n}_2} e^{-i\omega_{\mathbf{n}_2}t'}, \tag{6.9b}$$

$$\tilde{B}_{\alpha_1}(t) = \sum_{\mathbf{q}_1} \Lambda_{\mathbf{n}_1'\mathbf{n}_1}(\mathbf{q}_1) \left(a_{-\mathbf{q}_1}^\dagger e^{i\omega_{\mathrm{LO}}t} + a_{\mathbf{q}_1} e^{-i\omega_{\mathrm{LO}}t} \right), \tag{6.9c}$$

$$\tilde{B}_{\alpha_2}(t') = \sum_{\mathbf{q}_2} \Lambda_{\mathbf{n}_2'\mathbf{n}_2}(\mathbf{q}_2) \left(a_{-\mathbf{q}_2}^\dagger e^{i\omega_{\mathrm{LO}}t'} + a_{\mathbf{q}_2} e^{-i\omega_{\mathrm{LO}}t'} \right). \tag{6.9d}$$

We can now use these in Eq. (5.45) to derive a master equation specific to this system.

6.2 Master equation

Recalling Eq. (5.43) and Eq. (5.44), we can evaluate D_1 and E_2 using Eqs (6.9a), (6.9b), (6.9c) and (6.9d). Taking the trace over the bath operators and using Eq. (5.43) and Eq. (5.44), we get the equations

$$D_1 = \sum_{\mathbf{q}} \Lambda_{\mathbf{n}_1'\mathbf{n}_1}(\mathbf{q})\Lambda_{\mathbf{n}_2'\mathbf{n}_2}(-\mathbf{q}) \sum_{\mathbf{n}_2\mathbf{n}_2'} c^\dagger_{\mathbf{n}_2'} c_{\mathbf{n}_2} \int_0^\infty \mathrm{d}\tau \exp\left[i\left(\omega_{\mathbf{n}_2} - \omega_{\mathbf{n}_2'} - \omega_{\mathrm{LO}}\right)\tau\right], \tag{6.10}$$

$$E_2 = \sum_{\mathbf{q}} \Lambda^*_{\mathbf{n}_1'\mathbf{n}_1}(\mathbf{q})\Lambda^*_{\mathbf{n}_2'\mathbf{n}_2}(-\mathbf{q}) \sum_{\mathbf{n}_1\mathbf{n}_1'} c^\dagger_{\mathbf{n}_1'} c_{\mathbf{n}_1} \int_0^\infty \mathrm{d}\tau \exp\left[i\left(\omega_{\mathbf{n}_1} - \omega_{\mathbf{n}_1'} + \omega_{\mathrm{LO}}\right)\tau\right]. \tag{6.11}$$

In order to evaluate this integral we use the Cauchy principal value theorem to evaluate the improper integral, adding an infinitesimal Cauchy term, $\varepsilon\tau$, and working in the limit $\varepsilon \to 0^+$. If we first look at the integral term in D_1, which we denote as D_{int}, including the infinitesimal $\varepsilon\tau$ we have

$$\begin{aligned}
D_{\mathrm{int}} &= \lim_{\varepsilon\to 0^+} \int_0^\infty \mathrm{d}\tau \exp\left[i\left(\omega_{\mathbf{n}_2} - \omega_{\mathbf{n}_2'} - \omega_{\mathrm{LO}}\right)\tau - \varepsilon\tau\right], \\
&= \lim_{\varepsilon\to 0^+} \left[\frac{\exp\left[i\left(\omega_{\mathbf{n}_2} - \omega_{\mathbf{n}_2'} - \omega_{\mathrm{LO}}\right)\tau - \varepsilon\tau\right]}{i\left(\omega_{\mathbf{n}_2} - \omega_{\mathbf{n}_2'} - \omega_{\mathrm{LO}}\right) - \varepsilon}\right]_0^\infty, \\
&= \lim_{\varepsilon\to 0^+} \left[0 - \frac{1}{i\left(\omega_{\mathbf{n}_2} - \omega_{\mathbf{n}_2'} - \omega_{\mathrm{LO}}\right) - \varepsilon}\right], \qquad (6.12) \\
&= \lim_{\varepsilon\to 0^+} \frac{i}{\left(\omega_{\mathbf{n}_2} - \omega_{\mathbf{n}_2'} - \omega_{\mathrm{LO}}\right) + i\varepsilon}. \qquad (6.13)
\end{aligned}$$

As ϵ is an infinitesimal, we can take the limit of this as $\epsilon \to 0^+$, and evaluate

$$\begin{aligned}
D_{\mathrm{int}} &= \lim_{\varepsilon\to 0^+} i\frac{\left(\omega_{\mathbf{n}_2} - \omega_{\mathbf{n}_2'} - \omega_{\mathrm{LO}}\right) - i\varepsilon}{\left(\omega_{\mathbf{n}_2} - \omega_{\mathbf{n}_2'} - \omega_{\mathrm{LO}}\right)^2 + \varepsilon^2}, \\
&= \frac{i}{\left(\omega_{\mathbf{n}_2} - \omega_{\mathbf{n}_2'} - \omega_{\mathrm{LO}}\right)} - \lim_{\varepsilon\to 0^+} i\left(\frac{i\varepsilon}{\left(\omega_{\mathbf{n}_2} - \omega_{\mathbf{n}_2'} - \omega_{\mathrm{LO}}\right)^2 + \varepsilon^2}\right) \qquad (6.14)
\end{aligned}$$

here, we have taken the limit of the left hand term already. To take the limit of the right hand term, we notice that it is of the form of a Lorentzian,

$$L(x) = \frac{1}{\pi}\frac{\varepsilon}{\omega^2 + \varepsilon^2}, \tag{6.15}$$

which is normalised such that $\int_{-\infty}^{\infty} L(x)\,\mathrm{d}x = 1$. Due to its shape, when we take the limit of $\varepsilon \to 0$ of the Lorentzian, it becomes infinitely narrow and infinitely tall,

whilst still maintaining it's normalisation - in other words, at the limit of $\varepsilon \to 0^+$, Eq. (6.15) is a delta function $\delta(\omega)$. We can put this back into our equation, to give

$$D_{\text{int}} = \left[\mathbb{P} \frac{i}{\left(\omega_{\mathbf{n}_2} - \omega_{\mathbf{n}_2'} - \omega_{\text{LO}}\right)} + \pi\delta\left(\omega_{\mathbf{n}_2} - \omega_{\mathbf{n}_2'} - \omega_{\text{LO}}\right) \right], \tag{6.16}$$

where $\mathbb{P}$ is the Cauchy principle value. The first term in this equation is what's known as a level shift, a small shift in the energy levels, which can be absorbed into the states. Placing this back into Eq. (6.10) gives

$$D_1 = \sum_{\mathbf{q}} \Lambda^{k_1' k_1}_{n_1' n_1}(\mathbf{q}) \Lambda^{k_2' k_2}_{n_2' n_2}(-\mathbf{q}) \sum_{n_2 n_2'} \sum_{k_2 k_2'} c^\dagger_{\mathbf{n}_2'} c_{\mathbf{n}_2} \left[\pi\delta\left(\omega_{\mathbf{n}_2} - \omega_{\mathbf{n}_2'} - \omega_{\text{LO}}\right) \right]. \tag{6.17}$$

We can apply exactly the same process to Eq. (6.11), which leaves us with

$$E_2 = \sum_{\mathbf{q}} \Lambda^*_{\mathbf{n}_1' \mathbf{n}_1}(\mathbf{q}) \Lambda^*_{\mathbf{n}_2' \mathbf{n}_2}(-\mathbf{q}) \sum_{\mathbf{n}_1 \mathbf{n}_1'} c^\dagger_{\mathbf{n}_1'} c_{\mathbf{n}_1} \left[\pi\delta\left(\omega_{\mathbf{n}_1} - \omega_{\mathbf{n}_1'} + \omega_{\text{LO}}\right) \right]. \tag{6.18}$$

Using Eq. (6.17) and Eq. (6.18), we can go back to the general master equation, Eq. (5.45). The definition of $M(\mathbf{q})$ depends only on $|\mathbf{q}|$, so any negative in this term is removed. We can now input $-\mathbf{q}$ in place of $\mathbf{q}$, then taking the complex conjugate and utilising the fact that we have a sum over all $\mathbf{q}$, we find that

$$\Lambda_{\mathbf{n}'\mathbf{n}}(-\mathbf{q}) = \left[\Lambda_{\mathbf{n}\mathbf{n}'}(\mathbf{q})\right]^* \tag{6.19}$$

Our master equation then becomes

$$\begin{aligned}
\frac{d}{dt}\rho(t) = &-\frac{i}{\hbar}\left[H_S, \rho(t)\right] \\
&- \sum_{\substack{n_1, n_1', \\ n_2, n_2', \mathbf{q}}} \Big\{ \Lambda_{\mathbf{n}_1' \mathbf{n}_1}(\mathbf{q}) \Lambda^{k_2 k_2' *}_{n_2 n_2'}(\mathbf{q}) \pi\delta(\hbar\omega_{\mathbf{n}_2} - \hbar\omega_{\mathbf{n}_2'} - \hbar\omega_{\text{LO}}) c^\dagger_{\mathbf{n}_1'} c_{\mathbf{n}_1} c^\dagger_{\mathbf{n}_2'} c_{\mathbf{n}_2} \rho(t) \\
&\quad - \Lambda_{\mathbf{n}_1' \mathbf{n}_1}(\mathbf{q}) \Lambda^*_{\mathbf{n}_2 \mathbf{n}_2'}(\mathbf{q}) \pi\delta(\hbar\omega_{\mathbf{n}_2} - \hbar\omega_{\mathbf{n}_2'} - \hbar\omega_{\text{LO}}) c^\dagger_{\mathbf{n}_2'} c_{\mathbf{n}_2} \rho(t) c^\dagger_{\mathbf{n}_1'} c_{\mathbf{n}_1} \\
&\quad + \Lambda^*_{\mathbf{n}_2 \mathbf{n}_2'}(\mathbf{q}) \Lambda_{\mathbf{n}_1' \mathbf{n}_1}(\mathbf{q}) \pi\delta(\hbar\omega_{\mathbf{n}_2} - \hbar\omega_{\mathbf{n}_2'} + \hbar\omega_{\text{LO}}) \rho(t) c^\dagger_{\mathbf{n}_2'} c_{\mathbf{n}_2} c^\dagger_{\mathbf{n}_1'} c_{\mathbf{n}_1} \\
&\quad - \Lambda^*_{\mathbf{n}_2 \mathbf{n}_2'}(\mathbf{q}) \Lambda_{\mathbf{n}_1' \mathbf{n}_1}(\mathbf{q}) \pi\delta(\hbar\omega_{\mathbf{n}_2} - \hbar\omega_{\mathbf{n}_2'} + \hbar\omega_{\text{LO}}) c^\dagger_{\mathbf{n}_1'} c_{\mathbf{n}_1} \rho(t) c^\dagger_{\mathbf{n}_2'} c_{\mathbf{n}_2} \Big\}.
\end{aligned} \tag{6.20}$$

With the master equation in this form, we can see the three different "types" of term that make up the master equation. The first term in this equation is the von Neumann term and gives the closed system dynamics, which come from having moved from the interaction picture into the Schrödinger picture. The second type are the so-called "jump" terms, which have the form $L\rho L^\dagger$, where L is a Lindblad operator (in Eq. (6.20), these are the third and fifth lines of the equation). These correspond to a quantum jump in which the system shifts from one state to another. The final type are the reset terms, of the form $L^\dagger L\rho$ or $\rho L^\dagger L$ (in Eq. (6.20), these are the second and fourth lines of the equation). The reset term doesn't change the state, as the jump term does, but rather reduces the population within the current state.

This is a multi-particle model. We want to concentrate on one particle only so need to find expectation value, $\langle \mathbf{n}' | \dot{\rho}(t) | \mathbf{n} \rangle$. The creation and annihilation operators in each of the terms in the sum introduce Kronecker deltas when taking the

expectation value. The non-zero elements of these Kronecker deltas then allow us to narrow down the indices that we are using, such that

$$\begin{aligned}\frac{d}{dt}\langle \mathbf{n}_4|\rho(t)|\mathbf{n}_3\rangle = \frac{-i}{\hbar}\langle \mathbf{n}_4|[H_S,\rho(t)]|\mathbf{n}_3\rangle \\ -\sum_{\mathbf{q}}\Bigg\{\sum_{\mathbf{n}_2,\mathbf{n}_2'}\Lambda_{\mathbf{n}_4\mathbf{n}_2'}(\mathbf{q})\Lambda^*_{\mathbf{n}_2\mathbf{n}_2'}(\mathbf{q})\pi\delta(\hbar\omega_{\mathbf{n}_2}-\hbar\omega_{\mathbf{n}_2'}-\hbar\omega_{\mathrm{LO}})\langle \mathbf{n}_2|\rho(t)|\mathbf{n}_3\rangle \\ -\sum_{\mathbf{n}_1',\mathbf{n}_2}\Lambda_{\mathbf{n}_1'\mathbf{n}_3}(\mathbf{q})\Lambda^*_{\mathbf{n}_2\mathbf{n}_4}(\mathbf{q})\pi\delta(\hbar\omega_{\mathbf{n}_2}-\hbar\omega_{\mathbf{n}_4}-\hbar\omega_{\mathrm{LO}})\langle \mathbf{n}_2|\rho(t)|\mathbf{n}_1'\rangle \\ +\sum_{\mathbf{n}_2,\mathbf{n}_2'}\Lambda^*_{\mathbf{n}_2\mathbf{n}_2'}(\mathbf{q})\Lambda_{\mathbf{n}_2\mathbf{n}_3}(\mathbf{q})\pi\delta(\hbar\omega_{\mathbf{n}_2}-\hbar\omega_{\mathbf{n}_2'}+\hbar\omega_{\mathrm{LO}})\langle \mathbf{n}_4|\rho(t)|\mathbf{n}_2'\rangle \\ -\sum_{\mathbf{n}_1,\mathbf{n}_2'}\Lambda^*_{\mathbf{n}_3\mathbf{n}_2'}(\mathbf{q})\Lambda_{\mathbf{n}_4\mathbf{n}_1}(\mathbf{q})\pi\delta(\hbar\omega_{\mathbf{n}_3}-\hbar\omega_{\mathbf{n}_2'}+\hbar\omega_{\mathrm{LO}})\langle \mathbf{n}_1|\rho(t)|\mathbf{n}_2'\rangle\Bigg\}. \quad (6.21)\end{aligned}$$

In our continued attempts to simplify the master equation and make some more sense of the many indices we have to consider, we can rename the indices such that they are numbered only. Within the sum of $\mathbf{q}$, the indices represented by $\mathbf{n}_{1/2}(')$ are the starting states of the electron. All of these indices actually only represent two states in total, and as the terms of the equation are independent from each other, we can rewrite the starting indices as simply $\mathbf{n}_{1/2}=\mathbf{n}_1$ and $\mathbf{n}'_{1/2}=\mathbf{n}_2$. Rearranging the matrix elements according to the relation in Eq. (6.19) and using the fact that delta functions are even functions, i.e. $\delta(-x)=\delta(x)$, we get

$$\begin{aligned}\frac{d}{dt}\langle \mathbf{n}_4|\rho(t)|\mathbf{n}_3\rangle = -\frac{i}{\hbar}\langle \mathbf{n}_4|[H_S,\rho(t)]|\mathbf{n}_3\rangle \\ -\sum_{\mathbf{n}_1}\sum_{\mathbf{n}_2}\sum_{\mathbf{q}}\Lambda_{\mathbf{n}_4\mathbf{n}_1}(\mathbf{q})\Lambda^*_{\mathbf{n}_2\mathbf{n}_1}(\mathbf{q})\pi\delta(\hbar\omega_{\mathbf{n}_2}-\hbar\omega_{\mathbf{n}_1}-\hbar\omega_{\mathrm{LO}})\langle \mathbf{n}_2|\rho(t)|\mathbf{n}_3\rangle \\ +\sum_{\mathbf{n}_1}\sum_{\mathbf{n}_2}\sum_{\mathbf{q}}\Lambda^*_{\mathbf{n}_3\mathbf{n}_1}(-\mathbf{q})\Lambda_{\mathbf{n}_4\mathbf{n}_2}(-\mathbf{q})\pi\delta(\hbar\omega_{\mathbf{n}_2}-\hbar\omega_{\mathbf{n}_4}-\hbar\omega_{\mathrm{LO}})\langle \mathbf{n}_2|\rho(t)|\mathbf{n}_1\rangle \\ -\sum_{\mathbf{n}_1}\sum_{\mathbf{n}_2}\sum_{\mathbf{q}}\Lambda^*_{\mathbf{n}_2\mathbf{n}_1}(\mathbf{q})\Lambda_{\mathbf{n}_2\mathbf{n}_3}(\mathbf{q})\pi\delta(\hbar\omega_{\mathbf{n}_1}-\hbar\omega_{\mathbf{n}_2}-\hbar\omega_{\mathrm{LO}})\langle \mathbf{n}_4|\rho(t)|\mathbf{n}_1\rangle \\ +\sum_{\mathbf{n}_1}\sum_{\mathbf{n}_2}\sum_{\mathbf{q}}\Lambda^*_{\mathbf{n}_3\mathbf{n}_1}(\mathbf{q})\Lambda_{\mathbf{n}_4\mathbf{n}_2}(\mathbf{q})\pi\delta(\hbar\omega_{\mathbf{n}_1}-\hbar\omega_{\mathbf{n}_3}-\hbar\omega_{\mathrm{LO}})\langle \mathbf{n}_2|\rho(t)|\mathbf{n}_1\rangle. \quad (6.22)\end{aligned}$$

We want to rearrange the Λ in each term so that the order of indices better matches the delta function of each term, and to put them all in the same form such that we can write a general equation for the decay rate to describe all of them. To do this,

we recall the relation in Eq. (6.19), and rearrange each of the terms, to give

$$\begin{aligned}\frac{d}{dt}\langle \mathbf{n}_4|\rho(t)|\mathbf{n}_3\rangle = &-\frac{i}{\hbar}\langle \mathbf{n}_4|[H_S,\rho(t)]|\mathbf{n}_3\rangle \\ &- \sum_{\mathbf{n}_1\mathbf{n}_2\mathbf{q}} \Lambda^*_{\mathbf{n}_2\mathbf{n}_1}(\mathbf{q})\Lambda_{\mathbf{n}_4\mathbf{n}_1}(\mathbf{q})\pi\delta(\hbar\omega_{\mathbf{n}_2}-\hbar\omega_{\mathbf{n}1}-\hbar\omega_{\mathrm{LO}})\langle \mathbf{n}_2|\rho(t)|\mathbf{n}_3\rangle \\ &+ \sum_{\mathbf{n}_1\mathbf{n}_2\mathbf{q}} \Lambda^*_{\mathbf{n}_2\mathbf{n}_4}(\mathbf{q})\Lambda_{\mathbf{n}_1\mathbf{n}_3}(\mathbf{q})\delta(\hbar\omega_{\mathbf{n}_2}-\hbar\omega_{\mathbf{n}_4}-\hbar\omega_{\mathrm{LO}})\langle \mathbf{n}_2|\rho(t)|\mathbf{n}_1\rangle \\ &- \sum_{\mathbf{n}_1\mathbf{n}_2\mathbf{q}} \left[\Lambda^*_{\mathbf{n}_1\mathbf{n}_2}(\mathbf{q})\Lambda_{\mathbf{n}_3\mathbf{n}_2}(\mathbf{q})\pi\delta(\hbar\omega_{\mathbf{n}_1}-\hbar\omega_{\mathbf{n}_2}-\hbar\omega_{\mathrm{LO}})\right]^*\langle \mathbf{n}_4|\rho(t)|\mathbf{n}_1\rangle \\ &+ \sum_{\mathbf{n}_1\mathbf{n}_2\mathbf{q}} \left[\Lambda^*_{\mathbf{n}_1\mathbf{n}_3}(\mathbf{q})\Lambda_{\mathbf{n}_2\mathbf{n}_4}(\mathbf{q})\pi\delta(\hbar\omega_{\mathbf{n}_1}-\hbar\omega_{\mathbf{n}_3}-\hbar\omega_{\mathrm{LO}})\right]^*\langle \mathbf{n}_2|\rho(t)|\mathbf{n}_1\rangle\,. \end{aligned} \tag{6.23}$$

Now that we have similar forms for each term. We need to write a definition for the rate of emission of an LO-phonon, Γ, which works for all terms. To do this, we use Fermi's Golden rule, which gives the transition probability from an initial state, $|i\rangle$, to a final state, $|f\rangle$, as $\Gamma_{fi} = (2\pi/\hbar)|\langle f|H_1|i\rangle|^2\xi(E_f)$, where ξ is the density of states (as we consider single particles well away from the Fermi energy, and at zero temperature, we can set $\rho = 1$) and H_1 is the Hamiltonian describing the perturbation of the state going from i to f [100]. Applying this to the elements of our master equation, we get equations for the rates of

$$\Gamma^{\mathbf{n}_1\mathbf{n}_2}_{\mathbf{n}_1\mathbf{n}_4} = \frac{2\pi}{\hbar}\sum_{\mathbf{q}} \Lambda^*_{\mathbf{n}_2\mathbf{n}_1}(\mathbf{q})\Lambda_{\mathbf{n}_4\mathbf{n}_1}(\mathbf{q})\delta(\hbar\omega_{\mathbf{n}_2}-\hbar\omega_{\mathbf{n}_1}-\hbar\omega_{\mathrm{LO}}), \tag{6.24}$$

$$\Gamma^{\mathbf{n}_4\mathbf{n}_2}_{\mathbf{n}_3\mathbf{n}_1} = \frac{2\pi}{\hbar}\sum_{\mathbf{q}} \Lambda^*_{\mathbf{n}_2\mathbf{n}_4}(\mathbf{q})\Lambda_{\mathbf{n}_1\mathbf{n}_3}(\mathbf{q})\delta(\hbar\omega_{\mathbf{n}_2}-\hbar\omega_{\mathbf{n}_4}-\hbar\omega_{\mathrm{LO}}), \tag{6.25}$$

$$\Gamma^{\mathbf{n}_2\mathbf{n}_1}_{\mathbf{n}_2\mathbf{n}_3} = \frac{2\pi}{\hbar}\sum_{\mathbf{q}} \Lambda^*_{\mathbf{n}_1\mathbf{n}_2}(\mathbf{q})\Lambda_{\mathbf{n}_3\mathbf{n}_2}(\mathbf{q})\delta(\hbar\omega_{\mathbf{n}_1}-\hbar\omega_{\mathbf{n}_2}-\hbar\omega_{\mathrm{LO}}), \tag{6.26}$$

$$\Gamma^{\mathbf{n}_3\mathbf{n}_1}_{\mathbf{n}_4\mathbf{n}_2} = \frac{2\pi}{\hbar}\sum_{\mathbf{q}} \Lambda^*_{\mathbf{n}_1\mathbf{n}_3}(\mathbf{q})\Lambda_{\mathbf{n}_2\mathbf{n}_4}(\mathbf{q})\delta(\hbar\omega_{\mathbf{n}_1}-\hbar\omega_{\mathbf{n}_3}-\hbar\omega_{\mathrm{LO}}). \tag{6.27}$$

We can now use these definitions in the full equation to simplify further to give

$$\begin{aligned}\frac{d}{dt}\langle \mathbf{n}_4|\rho(t)|\mathbf{n}_3\rangle = &-\frac{i}{\hbar}\langle \mathbf{n}_4|[H_S,\rho(t)]|\mathbf{n}_3\rangle + \frac{1}{2}\sum_{\mathbf{n}_1\mathbf{n}_2}\Big\{\Gamma^{\mathbf{n}_4\mathbf{n}_2}_{\mathbf{n}_3\mathbf{n}_1}\langle \mathbf{n}_2|\rho(t)|\mathbf{n}_1\rangle \\ &+ \left[\Gamma^{\mathbf{n}_3\mathbf{n}_1}_{\mathbf{n}_4\mathbf{n}_2}\langle \mathbf{n}_1|\rho(t)|\mathbf{n}_2\rangle\right]^* - \Gamma^{\mathbf{n}_1\mathbf{n}_2}_{\mathbf{n}_1\mathbf{n}_4}\langle \mathbf{n}_2|\rho(t)|\mathbf{n}_3\rangle - \left[\Gamma^{\mathbf{n}_2\mathbf{n}_1}_{\mathbf{n}_2\mathbf{n}_3}\langle \mathbf{n}_1|\rho(t)|\mathbf{n}_4\rangle\right]^*\Big\}\,. \end{aligned} \tag{6.28}$$

We now have a master equation describing the emission of LO-phonons, but we still need to evaluate the rates themselves.

6.3 Evaluating the emission rates

From Eq. (6.4), we have a general definition for $\Lambda_{\mathbf{n}'\mathbf{n}}(\mathbf{q})$ of [23, 94]

$$\Lambda_{\mathbf{n}'\mathbf{n}}(\mathbf{q}) = M(\mathbf{q})\delta_{q_x,k'_x-k_x}G^{(y)}_{m'k'_x,mk_x}(q_y)G^{(z)}_{n'n}(q_z). \tag{6.29}$$

The overlaps of the wavefunctions are given by

$$G^{(y)}_{m'k'_x,mk_x}(q_y) = \int \mathrm{d}y e^{iq_y y} \chi^*_{m'k'_x}(y)\chi_{mk_x}(y), \tag{6.30}$$

in the y-direction and

$$G^{(z)}_{n'n}(q_z) = \int \mathrm{d}z e^{iq_z z} \phi^*_{n'}(z)\phi_n(z), \tag{6.31}$$

in the z-direction. For simplicity, we will calculate the rates for the lowest subbands, where $m = 0$ and $n = 1$, however the same methods can be used for higher subbands too. This means that the equation for the overlap of wavefunctions in the z-direction becomes

$$G^{(z)}_{11}(q_z) = \int \mathrm{d}e^{iq_z z} \phi^*_1(z')\phi_1(z). \tag{6.32}$$

In order to keep this derivation as general as possible, this equation will kept in this form for now. Specific parameters for the overlap in the z-direction will be introduced when the calculations are performed later. From the Hamiltonian with parabolic confinement and a magnetic field, we have eigenfunctions of [101]

$$\chi_{mk_x}(y) = \sqrt{\frac{1}{l_\Omega}} u_m \left(\frac{y - y_G}{l_\Omega} \right), \tag{6.33}$$

where

$$u_m(s) = \frac{1}{\sqrt{2^m m!}} \frac{1}{\pi^{1/4}} e^{-s^2/2} H_m(s). \tag{6.34}$$

and H_m are the Hermite polynomials, as discussed in Chapter 2. At the lowest Landau level then, we have

$$u_0 = \frac{1}{\pi^{1/4}} \exp\left[-\frac{1}{2} \left(\frac{y - y_G}{l_\Omega} \right)^2 \right], \tag{6.35}$$

which makes the eigenfunctions

$$\chi_{mk_x}(y) = \sqrt{\frac{1}{l_\Omega}} \frac{1}{\pi^{1/4}} \exp\left[-\frac{1}{2} \left(\frac{y - y_G}{l_\Omega} \right)^2 \right]. \tag{6.36}$$

This describes a Gaussian centred on the guide centre, y_G, with a width of the confinement length, l_Ω. To get the overlap in the y-direction, we can combine Eq. (6.30) and Eq. (6.36) to give

$$G^{(y)}_{0k',0k} = \frac{1}{l_\Omega \sqrt{\pi}} \int \mathrm{d}y e^{iq_y y} \exp\left[-\frac{1}{2} \left(\frac{y - y'_G}{l_\Omega} \right)^2 \right] \exp\left[-\frac{1}{2} \left(\frac{y - y_G}{l_\Omega} \right)^2 \right], \tag{6.37}$$

$$= \frac{1}{l_\Omega \sqrt{\pi}} \exp\left[\frac{-(y'^2_G + y^2_G)}{2l^2_\Omega} \right] \int \mathrm{d}y \exp\left[-\frac{y^2}{l^2_\Omega} + \left(\frac{y'_G + y_G}{l^2_\Omega} + iq_y \right) y \right], \tag{6.38}$$

which, when integrated with infinite limits, gives

$$G^{(y)}_{0k',0k}(q_y) = \exp\left[-\frac{(y'_G - y_G)^2}{4l^2_\Omega} \right] \exp\left[-\frac{q^2_y l^2_\Omega}{4} + \frac{iq_y}{2}(y'_G + y_G) \right]. \tag{6.39}$$

It's more natural to consider this equation in terms of wavenumber, k, instead of guide centre y_G. We can recall the definition of guide centre,

$$y_G(k) = \frac{\omega_c}{\Omega^2}\frac{\hbar k}{m_e^*}, \tag{6.40}$$

hence the overlap function is

$$G^{(y)}_{0k',0k}(q_y) = \exp\left[-\frac{\omega_c^2}{\Omega^4}\frac{\hbar^2}{m_e^*}\frac{(k'-k)^2}{4l_\Omega^2}\right]\exp\left[-\frac{q_y^2 l_\Omega^2}{4} + \frac{iq_y}{2}\frac{\omega_c}{\Omega^2}\frac{\hbar}{m_e^*}(k'+k)\right], \tag{6.41}$$

in terms of wavenumber.

We can take these generalised equations, and combine them to calculate the decay rates from Eqs. (6.24), (6.25), (6.26) and (6.27). As these equations are all of the same form, we can look at just Eq. (6.25) and then apply the same method to all four equations for rate. We are considering the case where $m = 0$, so we can write the rate equation out only in terms of k. First, we need to calculate the matrix elements. We have the general matrix element $\Lambda_{\mathbf{n'n}}(\mathbf{q})$ given by Eq. (6.29). We can use Eq. (6.19) to get

$$\Lambda^*_{\mathbf{nn'}} = \Lambda_{\mathbf{n'n}}(-\mathbf{q}) = M(-\mathbf{q})\delta_{-q_x,k'-k}G^{(y)}_{0k',0k}(-q_y)G^{(z)}_{11}(-q_z). \tag{6.42}$$

in the lowest Landau level. The matrix element, M, is dependent on only $|\mathbf{q}|$, so the negative in this term can be ignored.

We can now move from the general case to one specific to our needs. The probability that a phonon will not be emitted is described by the reset terms, and the probability that a phonon will be emitted is given by the jump terms, which we recall from section 6.2 describe a change from one state to another. We have four terms involving the rate in our master equation; two jump and two reset. We will calculate a general case which can be adapted to represent any one of these four cases, i.e.

$$\Gamma^{\mathbf{n}_4\mathbf{n}_2}_{\mathbf{n}_3\mathbf{n}_1} = \frac{2\pi}{\hbar}\sum_{\mathbf{q}}\Lambda^*_{\mathbf{n}_2\mathbf{n}_4}(\mathbf{q})\Lambda_{\mathbf{n}_1\mathbf{n}_3}(\mathbf{q})\delta\left(\hbar\omega_{\mathbf{n}_2} - \hbar\omega_{\mathbf{n}_4} - \hbar\omega_{\mathrm{LO}}\right), \tag{6.43}$$

which gives us matrix elements of

$$\Lambda_{\mathbf{n}_1\mathbf{n}_3}(\mathbf{q}) = M(\mathbf{q})\delta_{q_x,k_1-k_3}G^{(y)}_{0k_1,0k_3}(q_y)G^{(z)}_{11}(q_z), \tag{6.44}$$

$$\Lambda^*_{\mathbf{n}_2\mathbf{n}_4}(\mathbf{q}) = M(\mathbf{q})\delta_{-q_x,k_4-k_2}G^{(y)}_{0k_4,0k_2}(-q_y)G^{(z)}_{11}(-q_z). \tag{6.45}$$

Recalling also Eq. (6.5) and Eq. (6.6), our equation for the rate becomes

$$\Gamma^{\mathbf{n}_4\mathbf{n}_2}_{\mathbf{n}_3\mathbf{n}_1} = \frac{2\pi}{\hbar}\sum_{\mathbf{q}}\frac{M_0^2}{V}\frac{1}{|\mathbf{q}|^2}\delta_{-q_x,k_4-k_2}\delta_{q_x,k_1-k_3}\left|G^{(z)}_{11}(q_z)\right|^2 G^{(y)}_{0k_4,0k_2}(-q_y)G^{(y)}_{0k_1,0k_3}(q_y) \times \delta\left(\hbar\omega_{\mathbf{n}_2} - \hbar\omega_{\mathbf{n}_4} - \hbar\omega_{\mathrm{LO}}\right). \tag{6.46}$$

Splitting the sum over $\mathbf{q}$ into three sums over, q_x, q_y and q_z, we can then perform the sum over q_x, which results in $q_x = k_1 - k_3$. We can also write everything in terms

of k_j because as mentioned above, we are working in the lowest subband. This gives us a rate of

$$\Gamma_{k_3k_1}^{k_4k_2} = \frac{2\pi}{\hbar}\frac{M_0^2}{V}\delta_{-(k_1-k_3),k_4-k_2}\sum_{q_y}\sum_{q_z}\frac{1}{(k_1-k_3)^2+q_y^2+q_z^2}\left|G_{11}^{(z)}(q_z)\right|^2 \times \delta\left(\hbar\omega_{k_2}-\hbar\omega_{k_4}-\hbar\omega_{\mathrm{LO}}\right)\exp\left[-\frac{\omega_c^2}{\Omega^4}\frac{\hbar^2}{m_e^{*2}}\frac{1}{4l_\Omega^2}\left\{(k_4-k_2)^2+(k_1-k_3)^2\right\}\right] \times \exp\left[-\frac{q_y^2 l_\Omega^2}{2}+\frac{iq_y}{2}\frac{\omega_c}{\Omega^2}\frac{\hbar}{m_e^*}\left\{k_1+k_3-k_4-k_2\right\}\right]. \quad (6.47)$$

The notation convention we will use is that for $\Gamma_{k_3k_1}^{k_4k_2}$, the outer indices, in this case k_2 and k_1 are for the initial state and inner indices, here k_3 and k_4, are the final states.

We now change to the integral form. The confinement in the z-direction can be modelled as multiple different shapes. The simplest model is of a square well, however more closely related to the experimental confinement is the triangular well [53]. We can define the width of the confinement well, a and multiply the wavenumbers by this to give a unitless value, such that $Q_y = aq_y$, $Q_z = aq_z$ and $K_j = ak_j$, $(j = 1, 2, 3, 4)$ and the equation for rate becomes

$$\Gamma_{k_3k_1}^{k_4k_2} = \frac{2\pi}{\hbar}\frac{M_0^2}{V}\delta_{k_3-k_1,k_4-k_2}\left(\frac{L}{2\pi}\right)^2\int \mathrm{d}\frac{Q_y}{a}\int \mathrm{d}\frac{Q_z}{a}\frac{a^2}{\left[(K_1-K_3)^2+Q_y^2+Q_z^2\right]} \times\left|G_{11}^{(z)}(Q_z/a)\right|^2\delta\left(\hbar\omega_{k_2}-\hbar\omega_{k_4}-\hbar\omega_{\mathrm{LO}}\right) \times\exp\left[-\frac{\omega_c^2}{\Omega^4}\frac{\hbar^2}{m_e^{*2}}\frac{1}{4l_\Omega^2a^2}\left\{(K_4-K_2)^2+(K_1-K_3)^2\right\}\right] \times\left[-\frac{Q_y^2 l_\Omega^2}{2a^2}+\frac{iQ_y}{2a^2}\frac{\omega_c}{\Omega^2}\frac{\hbar}{m_e^*}\left\{K_1+K_3-K_4-K_2\right\}\right]. \quad (6.48)$$

We can write the integral over Q_z as

$$F_{11}^{(z)}(A) \equiv \int \mathrm{d}Q_z\frac{1}{A^2+Q_z^2}\left|G_{11}^{(z)}(Q_z/a)\right|^2, \quad (6.49)$$

where $A = \sqrt{(K_1-K_3)^2+Q_y^2}$. Evaluating these integrals for different confinements results in different F factors. For a square well, we have

$$F_{11}^{(z)}(A) = \frac{32\pi^5\left[e^{-A}+A-1\right]+20\pi^3A^3+3\pi A^5}{(A^2+4\pi^2)^2A^3}, \quad (6.50)$$

and for a triangular well, we have

$$F_{11}^{(z)}(A) = \frac{\pi(3A^5-10A^3+15A-8)}{8A[(A-1)^3(A+1)^3]}. \quad (6.51)$$

The results displayed later in this section are calculated with the more realistic triangular well. We can also name the part from the y-overlap, such that

$$F^{(y)}(Q_y) = \exp\left[-\frac{\omega_c^2}{\Omega^2}\frac{l_\Omega^2}{4a^2}\left\{(K_4-K_2)^2+(K_1-K_3)^2\right\}\right] \times\exp\left[-\frac{Q_y^2 l_\Omega^2}{2a^2}+\frac{iQ_y l_\Omega^2}{2a^2}\frac{\omega_c}{\Omega}\left\{K_1+K_3-K_4-K_2\right\}\right]. \quad (6.52)$$

Combining all of this gives the equation for the rate to be

$$\Gamma_{k_3k_1}^{k_4k_2} = \frac{M_0^2}{2\pi\hbar L}\delta_{k_3-k_1,k_4-k_2}\delta\left(\hbar\omega_{k_2} - \hbar\omega_{k_4} - \hbar\omega_{\mathrm{LO}}\right)\int \mathrm{d}Q_y F_{11}^{(z)}(A)F^{(y)}(Q_y). \quad (6.53)$$

Using the Kronecker delta we can eliminate k_4, as the non-zero value of $\delta_{k_3-k_1,k_4-k_2}$ results when $k_3 - k_1 = k_4 - k_2$ so that we can replace k_4 with $k_4 = k_3 + k_2 - k_1$. For clarity, we can now refer to the integral in this equation as

$$I(k_3, k_2, k_1) = \int \mathrm{d}Q_y F_{11}^{(z)}(A)F^{(y)}(Q_y), \quad (6.54)$$

such that

$$\Gamma_{k_3k_1}^{k_4k_2} = \frac{M_0^2}{2\pi\hbar L}\delta_{k_3-k_1,k_4-k_2}\delta\left(\hbar\omega_{k_2} - \hbar\omega_{k_4} - \hbar\omega_{\mathrm{LO}}\right) I(k_3, k_2, k_1). \quad (6.55)$$

In order to get the total rate out of our initial k values, we have to integrate over our final k values. As we have eliminated k_4 from the proceedings, we can change to the unitless version and integrate only over K_3,

$$\Gamma_{\mathrm{out}}^{k_1k_2} = \frac{L}{2\pi}\int \mathrm{d}k_3 \Gamma_{k_3k_1}^{k_4k_2}, \quad (6.56)$$

$$\Rightarrow \Gamma_{\mathrm{out}}^{K_1K_2} = \frac{L}{2\pi a}\int \mathrm{d}K_3 \Gamma_{K_3K_1}^{K_4K_2}. \quad (6.57)$$

which gives us an equation for the total rate out of,

$$\Gamma_{\mathrm{out}}^{K_1K_2} = \frac{M_0^2}{(2\pi)^2 a\hbar}\int \mathrm{d}K_3 I(K_3)\delta\left(\hbar\omega_{K_2} - \hbar\omega_{K_4} - \hbar\omega_{\mathrm{LO}}\right), \quad (6.58)$$

$$= \frac{M_0^2}{(2\pi)^2 a\hbar}\frac{I(K_3^0)}{2E_c|K_1 - K_2 - K_3^0|}, \quad (6.59)$$

where

$$K_3^0 = K_1 - K_2 + \sqrt{K_2^2 - \frac{\hbar\omega_{\mathrm{LO}}}{E_c}}, \quad (6.60)$$

and

$$E_c = \frac{\omega_y^2}{\Omega^2}\frac{\hbar^2}{2m_e^* a^2}. \quad (6.61)$$

In order to compare to previous results, we can rearrange this equation using the definitions in Eq. (6.5) and Eq. (6.6) in Eq. (6.59) to give

$$\Gamma_{\mathrm{out}}^{K_1K_2} = \frac{1}{2}\frac{\alpha\Omega\omega_{\mathrm{LO}}}{\pi\omega_y}\sqrt{\hbar\omega_{\mathrm{LO}}}\frac{I(K_3^0)}{\left|\sqrt{E_cK_2^2 - \hbar\omega_{\mathrm{LO}}}\right|}. \quad (6.62)$$

Now as

$$E = \frac{1}{2}\hbar\Omega + \frac{\omega_y^2}{\Omega^2}\frac{\hbar^2 k_x^2}{2m}, \quad (6.63)$$

our equation for the rate becomes

$$\Gamma_{\mathrm{out}}^{K_1K_2} = \frac{\alpha\Omega\omega_{\mathrm{LO}}}{2\pi\omega_y}\sqrt{\frac{\hbar\omega_{\mathrm{LO}}}{\Delta_0}}I(K_3^0), \quad (6.64)$$

where $\Delta_0 \equiv E - \frac{1}{2}\hbar\Omega - \hbar\omega_{\mathrm{LO}}$ and E is calculated with $k_x = K_2/a$. This is the general equation for the rate out of K_1 and K_2, where $I(K_3^0)$ is the integral over the y- and z-overlaps. We can now find an analytical expression for the rates with these integrals evaluated using the complex saddle point approximation,

$$I(C) = \int_\Gamma \mathrm{d}z f(z) \exp\left[Cg(z)\right] \tag{6.65}$$

$$= \sqrt{\frac{2\pi}{C}} \exp\left[Cg(z_0)\right] \frac{\eta f(z_0)}{\sqrt{-\eta^2 g''(z_0)}}(1 + O(1/C)), \tag{6.66}$$

where

$$z = z_0 + \frac{\eta y}{\sqrt{C}}. \tag{6.67}$$

Applying this to $I(K_3^0)$, and using $C = l_\Omega^2/2a^2$, we have

$$g(Q_y) = \left(Q_y - i\frac{\omega_c}{\Omega}(K_1 - K_2)\right)^2, \tag{6.68}$$

and defining the zero of this function as Q_0, we find

$$Q_0 = i\frac{\omega_c}{\Omega}(K_1 - K_2). \tag{6.69}$$

So Eq. (6.66) becomes

$$I\left(C = \frac{l_\Omega^2}{2a^2}\right) = \sqrt{2\pi} \exp\left[0\right] \frac{\eta F_{11}^{(z)}(A_0)}{\sqrt{-\eta^2 g''(Q)}}(1 + O(\frac{2a^2}{l_\Omega^2})), \tag{6.70}$$

where A_0 is A evaluated at Q_0. We also have

$$\begin{aligned} g(Q_y) &= -\left[Q_y^2 - 2i\frac{\omega_c}{\Omega}(K_1 - K_2)Q_y - \frac{\omega_c^2}{\Omega^2}(K_1 - K_2)^2\right], \\ g'(Q_y) &= -2\left[Q_y - i\frac{\omega_c}{\Omega}(K_1 - K_2)\right] (= 0 \text{ at the turning point}), \\ g''(Q_y) &= -2. \end{aligned} \tag{6.71}$$

This gives us a result for the integral of

$$I\left(C = \frac{l_\Omega^2}{2a^2}\right) = \sqrt{\frac{2\pi a^2}{l_\Omega^2}} F_{11}^{(z)}(A_0), \tag{6.72}$$

as $O(1/C)$ is small when $C = l_\Omega^2/2a^2$. This means that our equation for the rate is now

$$\Gamma_{\mathrm{out}}^{K_1 K_2} = \frac{\alpha\Omega\omega_{\mathrm{LO}} a}{\sqrt{2\pi}\omega_y l_\Omega} \sqrt{\frac{\hbar\omega_{\mathrm{LO}}}{\Delta_0}} \exp\left[-\frac{\omega_c^2}{\Omega^2}\frac{l_\Omega^2}{2a^2}\left(K_2 - \sqrt{K_2^2 - \frac{\hbar\omega_{\mathrm{LO}}}{E_c}}\right)^2\right] F_{11}^{(z)}(A_0), \tag{6.73}$$

where

$$A_0 = \sqrt{\left(K_2 - \sqrt{K_2^2 - \frac{\hbar\omega_{\mathrm{LO}}}{E_c}}\right)^2 - \frac{\omega_c^2}{\Omega^2}(K_1 - K_2)^2}. \tag{6.74}$$

We now would like to make substitutions for the wavenumbers K_1 and K_2, in terms of a mean wavenumber, $\bar{K} = (K_1 + K_2)/2$, and the separation between them, $\kappa_{12} = K_2 - K_1$,

$$K_1 = \bar{K} - \frac{\kappa_{12}}{2}, \tag{6.75}$$

$$K_2 = \bar{K} + \frac{\kappa_{12}}{2}. \tag{6.76}$$

Using these substitutions gives a total rate out of

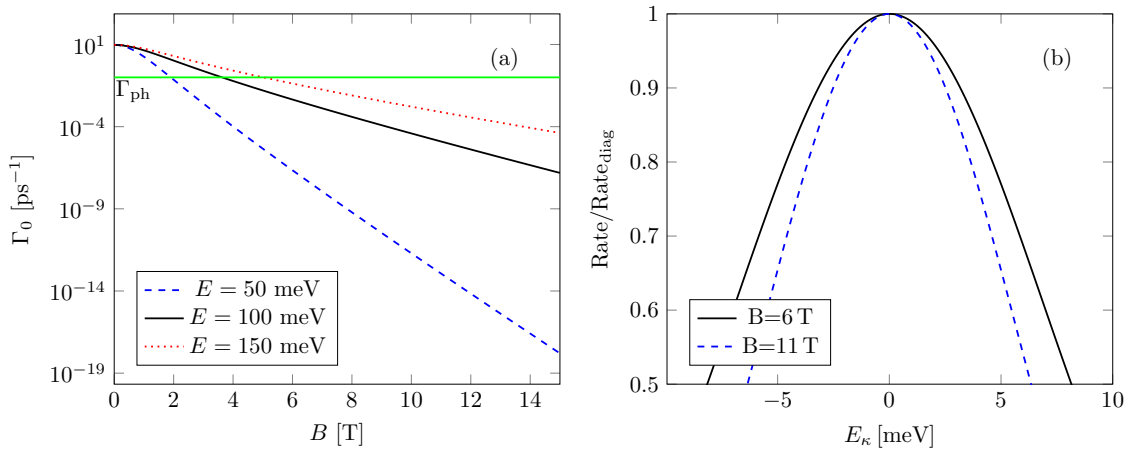

Figure 6.1: Panel (a) shows rates at $\kappa_{12} = 0$ against magnetic field for three different injection energies, which match up with the diagonal rates shown in Ref. [23], with the exception that we look here only at the lowest Landau level $n = 1$, such that we don't see the behaviour attributed to different Landau levels for low magnetic fields. The green horizontal line at $\Gamma_0 = 0.1\,\mathrm{ps}^{-1}$ is the rate of damping of LO-phonons in GaAs, $\Gamma_{\rm ph}$, and gives the cut off for the validity of the Markov approximation. Panel (b) shows the weighted average of our rates with the off diagonal terms taken into account with the rates of emission of LO phonons in the diagonal case. There is a contribution to the rate from the transitions in both the positive and negative direction, and the sum of these contributions gives the total weight, which is shown here. This is plotted against $E_\kappa = (\omega_y^2\hbar^2/\Omega^2 m_e^*)\kappa_{12}^2$, which is the energy range proportional to the difference in K values shown by κ_{12}. This is shown for two different magnetic fields, $B = 6\,\mathrm{T}$ and $B = 11\,\mathrm{T}$. Other parameters for these simulations were wavepacket width $\sigma_E = 1\,\mathrm{meV}$, confinement in the y-direction $\hbar\omega_y = 2.7\,\mathrm{meV}$ and $a = 3\,\mathrm{nm}$

$$\Gamma_{\rm out}^{\bar{K}\kappa_{12}} = \frac{\alpha\Omega\omega_{\rm LO}a}{\sqrt{2\pi}\omega_y l_\Omega}\sqrt{\frac{\hbar\omega_{\rm LO}}{\Delta_0}}F_{11}^{(z)}(A_0) \times \exp\left[-\frac{\omega_c^2}{\Omega^2}\frac{l_\Omega^2}{2a^2}\left(\bar{K} + \frac{\kappa_{12}}{2} - \sqrt{\left(\bar{K} + \frac{\kappa_{12}}{2}\right)^2 - \frac{\hbar\omega_{\rm LO}}{E_c}}\right)^2\right], \tag{6.77}$$

where

$$A_0 = \sqrt{\left\{\left(\bar{K} + \frac{\kappa_{12}}{2}\right) - \sqrt{\left(\bar{K} + \frac{\kappa_{12}}{2}\right)^2 - \frac{\hbar\omega_{\rm LO}}{E_c}}\right\}^2 - \frac{\omega_c^2}{\Omega^2}(\kappa_{12})^2}. \tag{6.78}$$

This equation can be compared to the equation for the rate in Ref. [23], which is

$$\Gamma_{n'n}(E) = \frac{\alpha\Omega\omega_{\mathrm{LO}}}{2\pi\omega_y}\sqrt{\frac{\hbar\omega_{\mathrm{LO}}}{\Delta_{n'}}}\Theta(\Delta_{n'})I_{n'n}(\delta_G), \tag{6.79}$$

where $I_{n'n}$ is the diagonal equivalent to our term $I(K_3^0)$, and $\Theta(x)$ is the Heaviside function, $\Theta = \int_{-\infty}^{x}\delta(s)\,\mathrm{d}s$.

The rate relative to the rate at $\bar{K}$ is shown in Fig. 6.1. It is clear here that for small values of ΔE and therefore κ_{12}, the diagonal rates match well with the full rates, as when $\kappa = 0$, $k = k'$, the behaviour includes only diagonal terms. As we move away from $\Delta E = 0$, and therefore $\kappa = 0$, we see a very steep drop off in the ratio, which means that the previous approach, which considered only the population terms, begins to differ significantly from our full equation with the off-diagonal coherence terms. At this point, therefore, we can no longer ignore these coherence terms. Theoretically, we consider wavepackets where ΔE is around 1 meV, and we can see from this plot that in this case, the diagonal rates are a good approximation, however, it is not unreasonable to expect wavepackets still on the order of 1 meV, but creeping up towards 4 meV [102]. In this case, there is a much more obvious difference between the diagonal and off-diagonal rates, the ratio being 0.7 and 0.8. As the full quantum approach becomes important quite quickly, it is also useful to develop an equation of motion for electrons undergoing phonon emission which also takes into account the coherence terms.

This is now a fully quantum master equation, which can be solved to show the fully quantum dynamics of the system under LO-phonon emission. The next step, then, is to investigate how this affects the electron, and compare this to the results using the semi-classical description of previous works [23]. In the next section, we will consider the evolution of the conditional dynamics of this system.

6.4 Validity of the Markov approximation

The Markov approximation in the case of LO-phonons in GaAs is discussed in Ref. [103], and found to be valid under certain conditions. LO-phonon modes in GaAs are damped with a rate of $\Gamma_{\mathrm{ph}} = 0.1\,\mathrm{ps}^{-1}$ [104, 105]. As long as the LO-phonon rates calculated in this thesis are sufficiently small compared to Γ_{ph}, the Markov approximation is valid. We can now take into account the results shown in Fig. 6.1a. This shows that for sufficiently high values of magnetic field, the Markov approximation is indeed valid. The green horizontal line in Fig. 6.1a shows Γ_{ph} for GaAs. Comparing our rates to this, we can see that for the Markov approximation to be valid for all energies considered, we must consider magnetic fields of at least 6 T.

Qualitatively, we can also consider the time scales for the lifetime and reabsorption of an LO-phonon with the distance travelled by an electron in this period. In the case of LO-phonons in GaAs, an electron will have travelled around 1 nm during the lifetime of the LO-phonon, meaning that the scope for reabsorption of an electron is extremely low.

It is worth noting that there are other approaches to this problem that can be considered, which were also explored in Ref. [105]. These approaches do not make the Markov approximation, which treats the LO-phonons as a bath that can be

safely ignored, but instead explicitly consider the LO-phonons as a system in their own right. In regimes where the coupling between the electron system and the LO-phonons is high, this becomes an important consideration. We do not consider such strong couplings in this thesis and as such make use of the Markov approximation.

6.5 Equation of motion

When considering the quantum world, decoherence is something that we wish to avoid at all costs; the more decoherence something experiences, the more classical it gets. Naturally, this is not ideal for investigating a quantum system. The most important case to consider, then, is the subensemble that hasn't emitted a phonon, and therefore is coherent. This is lucky for us as this subensemble is slightly easier to calculate because it only undergoes loss, and not jumps and therefore remains pure and can be modelled through a non-Hermitian Schrödinger equation. The subensemble that undergoes phonon emission is a much more complicated calculation, and is beyond the scope of this thesis. In this section we will split the dynamics into these two subensembles, and consider the evolution of the one which undergoes no phonon emission. As well as numerically modelling the behaviour, we will also derive an analytic approximation of the dynamics to ascertain a rough understanding of the behaviour.

Returning now to Eq. (6.28), we can see that due to the localisation in energy space of the wavepacket, we can split density matrix up into sectors labelled $M = 0, 1, ...$ depending on how many phonons have been emitted. We can split these such that the equation for the density matrix with no phonons depends only on the reset terms in the master equation,

$$\frac{d}{dt}\langle \mathbf{n}_4|\rho^{(0)}(t)|\mathbf{n}_3\rangle = -\frac{i}{\hbar}\langle \mathbf{n}_4|[H_S, \rho^{(0)}(t)]|\mathbf{n}_3\rangle - \frac{1}{2}\sum_{\mathbf{n}_1\mathbf{n}_2}\left\{\Gamma^{\mathbf{n}_1\mathbf{n}_2}_{\mathbf{n}_1\mathbf{n}_4}\langle \mathbf{n}_2|\rho^{(0)}(t)|\mathbf{n}_3\rangle + \left[\Gamma^{\mathbf{n}_2\mathbf{n}_1}_{\mathbf{n}_2\mathbf{n}_3}\langle \mathbf{n}_1|\rho^{(0)}(t)|\mathbf{n}_4\rangle\right]^*\right\}, \quad (6.80)$$

and the equation for the case where we have emission of phonons depends on both the reset terms and the jump terms which describe the probability of emission. The expectation value here of $\langle \mathbf{n}_4|[H_S, \rho^{(M)}](t)|\mathbf{n}_3\rangle$ describes the behaviour of an electron after phonon emission, such that the master equation for the case where phonons are emitted becomes

$$\frac{d}{dt}\langle \mathbf{n}_4|\rho^{(M)}(t)|\mathbf{n}_3\rangle = -\frac{i}{\hbar}\langle \mathbf{n}_4|[H_S, \rho^{(M)}(t)]|\mathbf{n}_3\rangle - \frac{1}{2}\sum_{\mathbf{n}_1\mathbf{n}_2}\left\{\Gamma^{\mathbf{n}_1\mathbf{n}_2}_{\mathbf{n}_1\mathbf{n}_4}\langle \mathbf{n}_2|\rho^{(M)}(t)|\mathbf{n}_3\rangle + \left[\Gamma^{\mathbf{n}_2\mathbf{n}_1}_{\mathbf{n}_2\mathbf{n}_3}\langle \mathbf{n}_1|\rho^{(M)}(t)|\mathbf{n}_4\rangle\right]^*\right\} + \frac{1}{2}\sum_{\mathbf{n}_1\mathbf{n}_2}\left\{\Gamma^{\mathbf{n}_4\mathbf{n}_2}_{\mathbf{n}_3\mathbf{n}_1} + \left[\Gamma^{\mathbf{n}_3\mathbf{n}_1}_{\mathbf{n}_4\mathbf{n}_2}\right]^*\right\}\langle \mathbf{n}_2|\rho^{(M-1)}(t)|\mathbf{n}_1\rangle. \quad (6.81)$$

As we approach the band bottom, there is no longer enough energy in the electron to emit an LO-phonon, which sets a maximum to the number of phonons emitted.

We can therefore write the emission part as

$$\frac{d}{dt}\langle \mathbf{n}_4|\rho^{(M_{\max})}(t)|\mathbf{n}_3\rangle = -\frac{i}{\hbar}\langle \mathbf{n}_4|[H_S,\rho^{(M_{\max})}(t)]|\mathbf{n}_3\rangle + \frac{1}{2}\sum_{\mathbf{n}_1\mathbf{n}_2}\left\{\Gamma^{\mathbf{n}_4\mathbf{n}_2}_{\mathbf{n}_3\mathbf{n}_1} + \left[\Gamma^{\mathbf{n}_3\mathbf{n}_1}_{\mathbf{n}_4\mathbf{n}_2}\right]^*\right\}\langle \mathbf{n}_2|\rho^{(M_{\max}-1)}(t)|\mathbf{n}_1\rangle\,, \quad (6.82)$$

where $M \leq M_{\max}$. At any value lower than $M_{\max} = 1$, there is no emission of a phonon and the electron passes straight through the system, as far as LO-phonons are concerned; they are not necessarily unaffected by other incoherent effects which we do not consider here. In this case we have

$$\frac{d}{dt}\langle \mathbf{n}_4|\rho^{(0)}(t)|\mathbf{n}_3\rangle = -\frac{i}{\hbar}\langle \mathbf{n}_4|[H_S,\rho^{(0)}(t)]|\mathbf{n}_3\rangle - \frac{1}{2}\sum_{\mathbf{n}_1\mathbf{n}_2}\left\{\Gamma^{\mathbf{n}_1\mathbf{n}_2}_{\mathbf{n}_1\mathbf{n}_4}\langle \mathbf{n}_2|\rho^{(0)}(t)|\mathbf{n}_3\rangle + \left[\Gamma^{\mathbf{n}_2\mathbf{n}_1}_{\mathbf{n}_2\mathbf{n}_3}\langle \mathbf{n}_1|\rho^{(0)}(t)|\mathbf{n}_4\rangle\right]^*\right\}, \quad (6.83)$$

$$\frac{d}{dt}\langle \mathbf{n}_4|\rho^{(1)}(t)|\mathbf{n}_3\rangle = -\frac{i}{\hbar}\langle \mathbf{n}_4|[H_S,\rho^{(1)}(t)]|\mathbf{n}_3\rangle + \frac{1}{2}\sum_{\mathbf{n}_1\mathbf{n}_2}\left\{\Gamma^{\mathbf{n}_4\mathbf{n}_2}_{\mathbf{n}_3\mathbf{n}_1} + \left[\Gamma^{\mathbf{n}_3\mathbf{n}_1}_{\mathbf{n}_4\mathbf{n}_2}\right]^*\right\}\langle \mathbf{n}_2|\rho^{(0)}(t)|\mathbf{n}_1\rangle\,. \quad (6.84)$$

Here is where we shall leave the case of a system which emits at least one phonon, as the calculation of these dynamics is beyond the scope of this thesis. In reality, any quantum experiment is the most useful when it does not undergo decoherence, so we will now examine the behaviour of an electron moving through the system without emitting a phonon.

These are general equations for the rate, but we are interested only in the lowest subband, so $\mathbf{n}_i = \{0, k_i\}$. We know that the rate $\Gamma^{k_c k_d}_{k_a k_b}$ depends on $\delta_{k_a-k_b,k_c-k_d}$, and also in general we have $\Gamma^{k_a k_b}_{k_a k_b} = \Gamma^{k_a k_b *}_{k_a k_b}$. We can also now evaluate $\langle \mathbf{n}_4|[H_S,\rho(t)]|\mathbf{n}_3\rangle$, where $H_S = \sum_{\mathbf{n}} E_{\mathbf{n}} c^\dagger_{\mathbf{n}} c_{\mathbf{n}}$, and $\mathbf{n} = \{0, n\}$.

$$\begin{aligned}\langle k_4|[H_S,\rho(t)]|k_3\rangle &= \langle k_4|H_S\rho(t) - \rho(t)H_S|k_3\rangle\,,\\ &= \langle k_4|\sum_k E_k c^\dagger_k c_k \rho(t) - \rho(t)\sum_k E_k c^\dagger_k c_k|k_3\rangle\,,\\ &= (E_{k_4} - E_{k_3})\,\langle k_4|\rho(t)|k_3\rangle\,. \end{aligned} \quad (6.85)$$

Combining all of this means that we can rewrite Eq. (6.83) as

$$\begin{aligned}\frac{d}{dt}\langle k_4|\rho^{(0)}(t)|k_3\rangle &= -\frac{i}{\hbar}\langle k_4|[H_S,\rho^{(0)}(t)]|k_3\rangle - \frac{1}{2}\sum_{k_1k_2}\left\{\Gamma^{k_1k_4}_{k_1k_4}\langle k_4|\rho^{(0)}(t)|k_3\rangle + \Gamma^{k_2k_3}_{k_2k_3}\langle k_4|\rho^{(0)}(t)|k_3\rangle\right\},\\ &= \left\{-\frac{i}{\hbar}(E_{k_4} - E_{k_3}) - \frac{1}{2}\sum_{k_1k_2}\left(\Gamma^{k_1k_4}_{k_1k_4} + \Gamma^{k_2k_3}_{k_2k_3}\right)\right\}\langle k_4|\rho^{(0)}(t)|k_3\rangle\,. \end{aligned} \quad (6.86)$$

Integrating with respect to t, we get

$$\langle k_4|\rho^{(0)}(t)|k_3\rangle = \langle k_4|\rho^{(0)}(t=0)|k_3\rangle \times \exp\left[\left\{-\frac{i}{\hbar}(E_{k_4}-E_{k_3}) - \frac{1}{2}\sum_{k_1k_2}\left(\Gamma^{k_1k_4}_{k_1k_4}+\Gamma^{k_2k_3}_{k_2k_3}\right)\right\}t\right], \quad (6.87)$$

which we can write as

$$\langle k_4|\rho^{(0)}(t)|k_3\rangle = \exp\left[-\frac{1}{2}\sum_{k_1k_2}\left(\Gamma^{k_1k_4}_{k_1k_4}+\Gamma^{k_2k_3}_{k_2k_3}\right)t\right]\varrho^{(0)}_{k_4k_3}(t), \quad (6.88)$$

where $\varrho^{(0)}_{k_4k_3}(t)$ is the solution of the problem without phonons.

If we define the $k_4 = k_0 + \Delta k_4$ and $k_3 = k_0 - \Delta k_3$, and change the notation such that $\sum_a \Gamma^{ab}_{ac} = \Gamma^{cb}_{\text{out}}$, and $\Gamma^{dd}_{\text{out}} = \Gamma^{d}_{\text{out}}$, we can rewrite the contents of the exponential as

$$\frac{1}{2}\sum_{k_1k_2}\left(\Gamma^{k_1k_4}_{k_1k_4}+\Gamma^{k_2k_3}_{k_2k_3}\right) = \frac{1}{2}\left(\Gamma^{k_4}_{\text{out}}+\Gamma^{k_3}_{\text{out}}\right) = \frac{1}{2}\left(\Gamma^{k_0+\Delta k_4}_{\text{out}}+\Gamma^{k_0+\Delta k_3}_{\text{out}}\right). \quad (6.89)$$

Using the Taylor expansion gives an expression for these rates of

$$\frac{1}{2}\sum_{k_1k_2}\left(\Gamma^{k_1k_4}_{k_1k_4}+\Gamma^{k_2k_3}_{k_2k_3}\right) \approx \Gamma^{k_0}_{\text{out}} + \frac{1}{2}\left(\Delta k_3+\Delta k_4\right)\left.\frac{\mathrm{d}\Gamma^{k}_{\text{out}}}{\mathrm{d}k}\right|_{k=k_0} + \frac{1}{4}\left(\Delta k_3^2+\Delta k_4^2\right)\left.\frac{\mathrm{d}^2\Gamma^{k}_{\text{out}}}{\mathrm{d}k^2}\right|_{k=k_0}. \quad (6.90)$$

So we can rewrite Eq. (6.88) as

$$\langle k_4|\rho^{(0)}(t)|k_3\rangle = \exp\left[-\Gamma^{k_0}_{\text{out}}t\right]\exp\left[-\left\{\frac{1}{2}\left(\Delta k_3+\Delta k_4\right)\left.\frac{\mathrm{d}\Gamma^{k}_{\text{out}}}{\mathrm{d}k}\right|_{k=k_0} + \frac{1}{4}\left(\Delta k_3^2+\Delta k_4^2\right)\left.\frac{\mathrm{d}^2\Gamma^{k}_{\text{out}}}{\mathrm{d}k^2}\right|_{k=k_0}\right\}t\right]\varrho^{(0)}_{k_4k_3}(t). \quad (6.91)$$

In order to examine the behaviour of the electron in position space, we need to look at the wavepacket properties. In Section 3.2 we introduced the starting state for an electron wavepacket in the lowest Landau level with momentum distributed according to a Gaussian, as [23]

$$|\psi(0)\rangle = \sum_k N_\alpha e^{-\alpha(k-k_0)^2}|k\rangle \quad (6.92)$$

where N_α is the normalisation constant

$$N_\alpha = \frac{(8\alpha\pi)^{1/4}}{\sqrt{L}}. \quad (6.93)$$

and $\alpha = (2\sigma)^{-2}$. The density matrix as a function of time is given as

$$\rho(t) \equiv |\psi(t)\rangle\langle\psi(t)|, \quad (6.94)$$

so we have

$$\rho(0) = |\psi\rangle\langle\psi| = \sum_{kk'} N_\alpha e^{-\alpha(k-k_0)^2} |k\rangle\langle k'| N_\alpha e^{-\alpha(k'-k_0)^2}. \tag{6.95}$$

Density operators evolve according to the Liouville-von Neumann equation, which states that [106]

$$i\hbar\frac{\partial\rho}{\partial t} = [H, \rho] \tag{6.96}$$

the time evolution for a time-independent Hamiltonian is then

$$\rho(t) = e^{-iHt/\hbar}\rho(0)e^{iHt/\hbar}. \tag{6.97}$$

If we input our Hamiltonian and combine Eq. (6.95) and Eq. (6.97), then we get

$$\langle 0k'|\rho(t)|0k\rangle = \frac{(8\beta\pi)^{1/2}}{L}\exp\left[-\frac{1}{4}\frac{(E_k - E_0)^2}{\sigma_E^2} - \frac{1}{4}\frac{(E_{k'} - E_0)^2}{\sigma_E^2}\right] \times \exp\left[-\frac{i}{\hbar}(E_{k'} - E_k)t\right], \tag{6.98}$$

where

$$\beta = \left(\frac{\hbar v_0}{2\sigma_E}\right)^2, \tag{6.99}$$

as $\Delta E = \hbar v_0 \Delta k$ move from in terms of k to E. We can then introduce the quantum Hall energy, as mentioned in chapter 5,

$$\langle x'y'|0k'\rangle = \frac{1}{\sqrt{L}}e^{ik'x'}\frac{1}{\pi^{1/4}\sqrt{l_\Omega}}\exp\left[-\frac{1}{2}\left(\frac{y' - y_G(k')}{l_\Omega}\right)^2\right], \tag{6.100}$$

$$\langle 0k|xy\rangle = \frac{1}{\sqrt{L}}e^{-ikx}\frac{1}{\pi^{1/4}\sqrt{l_\Omega}}\exp\left[-\frac{1}{2}\left(\frac{y - y_G(k)}{l_\Omega}\right)^2\right], \tag{6.101}$$

where $y_G(k) = \frac{\omega_c}{\Omega^2}\frac{\hbar k}{m_e^*} = \frac{\omega_c}{\Omega}l_\Omega^2 k$ is the guide centre as introduced in Part I. We can also include the damping from Eq. (6.91) by multiplying by the exponential containing the damping term and moving into the same notation, i.e. where $k' = k_4$ and $k = k_3$. If we combine all of the constituents so far and sum over k, k' we can write this in integral form as

$$\begin{aligned}\sum_{k_3k_4}\langle x'y'|0k_4\rangle\,\langle 0k_4|\rho(t)|0k_3\rangle\,\langle 0k_3|xy\rangle = \int \mathrm{d}k_3 \int \mathrm{d}k_4 \frac{\sqrt{2}}{l_\Omega(2\pi)^2}\frac{\hbar v_0}{\sigma_E}\exp\left[-\Gamma_{\text{out}}^{k_0}t\right] \\ \times e^{ik_4x'}e^{-ik_3x}\exp\left[-\frac{1}{4}\frac{(E_{k_3} - E_0)^2}{\sigma_E^2} - \frac{1}{4}\frac{(E_{k_4} - E_0)^2}{\sigma_E^2}\right] \\ \times \exp\left[\left\{-\frac{i}{\hbar}(E_{k_4} - E_{k_3}) - \left(\frac{1}{2}\left(\Delta k_3 + \Delta k_4\right)\left.\frac{\mathrm{d}\Gamma_{\text{out}}^k}{\mathrm{d}k}\right|_{k=k_0}\right.\right.\right. \\ \left.\left.\left. + \frac{1}{4}\left(\Delta k_3^2 + \Delta k_4^2\right)\left.\frac{\mathrm{d}^2\Gamma_{\text{out}}^k}{\mathrm{d}k^2}\right|_{k=k_0}\right)\right\}t\right] \\ \times \exp\left[-\frac{1}{2}\left(\frac{y - y_G(k_3)}{l_\Omega}\right)^2\right]\exp\left[-\frac{1}{2}\left(\frac{y' - y_G(k_4)}{l_\Omega}\right)^2\right].\end{aligned} \tag{6.102}$$

Due to the transport being solely in the x-direction, we shall trace over the y-component as it offers little physical insight into the dynamics. Recalling the confinement length, $l_\Omega = \sqrt{\hbar/m_e^*\Omega}$, we can define

$$\mu = \left(\frac{\omega_c}{\Omega}\right) l_\Omega, \tag{6.103}$$

and take the trace by integrating over $y = y'$ to give,

$$\begin{aligned}\sum_{k_3k_4} \langle x'y|0k_4\rangle \, \langle 0k_4|\rho(t)|0k_3\rangle \, \langle 0k_3|xy\rangle = \int \mathrm{d}k_3 \int \mathrm{d}k_4 \frac{\sqrt{2\pi}}{(2\pi)^2}\frac{\hbar v_0}{\sigma_E} \exp\left[-\Gamma_{\text{out}}^{k_0} t\right] \\ \times e^{ik_4x'}e^{-ik_3x} \exp\left[-\frac{1}{4}\frac{(E_{k_3}-E_0)^2}{\sigma_E^2} - \frac{1}{4}\frac{(E_{k_4}-E_0)^2}{\sigma_E^2}\right] \\ \times \exp\left[\left\{-\frac{i}{\hbar}(E_{k_4}-E_{k_3}) - \left(\frac{1}{2}\left(\Delta k_3 + \Delta k_4\right)\left.\frac{\mathrm{d}\Gamma_{\text{out}}^k}{\mathrm{d}k}\right|_{k=k_0}\right.\right.\right. \\ \left.\left.\left. + \frac{1}{4}\left(\Delta k_3^2 + \Delta k_4^2\right)\left.\frac{\mathrm{d}^2\Gamma_{\text{out}}^k}{\mathrm{d}k^2}\right|_{k=k_0}\right)\right\} t\right] \\ \times \exp\left[-\frac{\mu^2}{2}(k_3^2+k_4^2)\right] \exp\left[\frac{\mu^2}{4}(k_3+k_4)^2\right]\end{aligned} \tag{6.104}$$

Using the dispersion relation for the wavepacket shown in Part I, the expansion $k = k_0 + \Delta k$ and linearising in k, we have

$$\begin{aligned}E_k =& \frac{1}{2}\hbar\Omega + \left(\frac{\omega_y}{\Omega}\right)^2 \frac{\hbar^2}{2m_e^*}(k_0+\Delta k)^2, \\ =& \frac{1}{2}\hbar\Omega + \left(\frac{\omega_y}{\Omega}\right)^2 \frac{\hbar^2 k_0^2}{2m_e^*} + \left(\frac{\omega_y}{\Omega}\right)^2 \frac{\hbar^2 k_0 \Delta k}{m_e^*}, \\ =& E_0 + \Delta E,\end{aligned} \tag{6.105}$$

where

$$E_0 = \frac{1}{2}\hbar\Omega + \left(\frac{\omega_y}{\Omega}\right)^2 \frac{\hbar^2}{m_e^*}k_0^2; \qquad \Delta E = \left(\frac{\omega_y}{\Omega}\right)^2 \frac{\hbar^2}{m_e^*}k_0\Delta k. \tag{6.106}$$

We have the definition of velocity also from Section 2.6,

$$v_0 = \frac{1}{\hbar}\frac{\partial E}{\partial k} = \frac{1}{\hbar}\frac{\Delta E}{\Delta k} = \left(\frac{\omega_y}{\Omega}\right)^2 \frac{\hbar}{m_e^*}k_0. \tag{6.107}$$

We therefore have

$$E_{k_3} = E_0 + \hbar v_0 \Delta k_3, \tag{6.108}$$

$$E_{k_4} = E_0 + \hbar v_0 \Delta k_4. \tag{6.109}$$

which we can put into into Eq. (6.104). After expanding using $k = k_0 + \Delta k$, we

linearise with respect to Δk, to give

$$\sum_{k_3 k_4} \langle x'y|0k_4\rangle \, \langle 0k_4|\rho(t)|0k_3\rangle \, \langle 0k_3|xy\rangle = \int \mathrm{d}k_3 \int \mathrm{d}k_4 \frac{\sqrt{2\pi}}{(2\pi)^2} \frac{\hbar v_0}{\sigma_E} \exp\left[-\Gamma^{k_0}_{\mathrm{out}} t\right] \times e^{i(k_0+\Delta k_4)x'} e^{-i(k_0+\Delta k_3)x} \exp\left[-\frac{\hbar^2 v_0^2}{4\sigma_E^2}\left\{\Delta k_3^2 + \Delta k_4^2\right\}\right] \times \exp\left[\left\{-iv_0(\Delta k_4 - \Delta k_3) - \left(\frac{1}{2}\left(\Delta k_3 + \Delta k_4\right) \left.\frac{\mathrm{d}\Gamma^k_{\mathrm{out}}}{\mathrm{d}k}\right|_{k=k_0} + \frac{1}{4}\left(\Delta k_3^2 + \Delta k_4^2\right) \left.\frac{\mathrm{d}^2\Gamma^k_{\mathrm{out}}}{\mathrm{d}k^2}\right|_{k=k_0}\right)\right\} t\right]. \quad (6.110)$$

Performing this integration gives a result of

$$\rho(x, x', t) = \sqrt{\frac{2}{\pi}} \frac{\hbar v_0 \sigma_E}{\hbar^2 v_0^2 + \sigma_E^2 \Gamma'' t} \exp\left[-\Gamma^{k_0}_{\mathrm{out}} t\right] \times \exp\left[i(x'-x)\left\{k_0 - \frac{\sigma_E^2}{\hbar^2 v_0^2 + \sigma_E^2 \Gamma'' t}\Gamma' t\right\}\right] \times \exp\left[-\frac{\sigma_E^2}{\hbar^2 v_0^2 + \sigma_E^2 \Gamma'' t}\left\{\left[(x - v_0 t)^2 + (x' - v_0 t)^2\right] + \frac{1}{2}\left(\Gamma' t\right)^2\right\}\right], \quad (6.111)$$

where for clarity, we have written

$$\Gamma'' = \left.\frac{\mathrm{d}^2\Gamma^k_{\mathrm{out}}}{\mathrm{d}k^2}\right|_{k=k_0}; \qquad \Gamma' = \left.\frac{\mathrm{d}\Gamma^k_{\mathrm{out}}}{\mathrm{d}k}\right|_{k=k_0}. \quad (6.112)$$

We can use this equation to investigate the motion of the electron. Including coherences means that we should get a travelling wavepacket, and the $-\Gamma_{\mathrm{out}}$ exponential suggests that there will be a dissipation over time. We also have dispersion from the Γ'' term in the denominator. The natural dispersion from the wavepackets initial width in k-space has been removed by the linearisation of the energy dispersion relation, such that what we see here is from the Γ'' term alone. The density matrix does not preserve the trace, due to the conditional evolution, and accordingly the trace now gives the probability of such a non-Hermition evolution occurring.

In Fig. 6.2 we can see that Eq. (6.111) describes a moving wavepacket. Parts (a - f) show the wavepacket over time as it moves through space at a velocity v_0. This equation also describes a dissipation of the wavepacket, given by the term $\exp\left[-\Gamma^{k_0}_{\mathrm{out}} t\right]$ which can be seen in the fading of the wavepacket over time. The fact that these changes occur in the case of Eq. (6.83) gives credence to the results of the semiclassical only case in Ref. [23], as this is the case where there is no emission of phonons, so there is no effect from the spread κ involved.

There is clearly a dependence on the energy of the electron for derivatives of the emission rate terms. Looking at Fig. 6.3 we see how (a) Γ'/v_0 and (b) $\sigma_E^2\Gamma''/\hbar^2 v_0^2$ vary with injection energy and for different values of magnetic field B. At lower energies these values are close to 0 so the terms involving them are of little importance in the equation, however as the energy increases these terms become larger and therefore their effects cannot be ignored. Perhaps a more intuitive view of the importance of the Γ'' term can be seen in Fig. 6.4. Panel (a) shows the time in microseconds

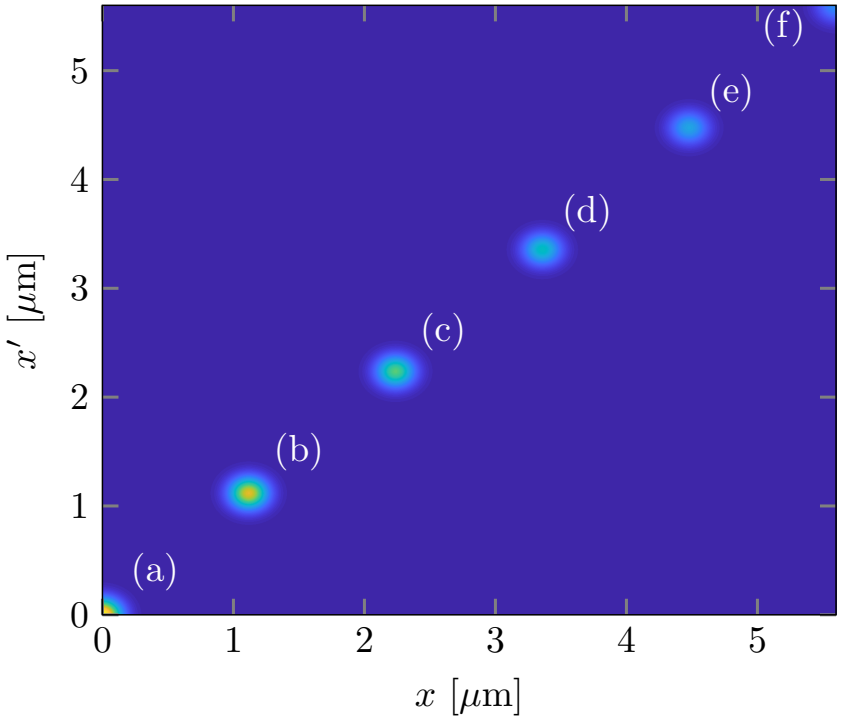

Figure 6.2: Each of the parts (a-f) show the wavepacket at time intervals of 25 ps each, normalised with respect to the initial state. We can see then that we do indeed have a wavepacket which moves over time, and dissipates as well which can be seen due to the fading. The parameters used for this simulation were magnetic field, $B = 5$ T, central energy, $E_0 = 150\,\text{meV}$, wavepacket width, $\sigma_E = 1\,\text{meV}$ and confinement in the y-direction, $\hbar\omega_y = 2.7\,\text{meV}$ and $a = 3\,\text{nm}$.

at which the second derivative of the emission rate becomes the dominant term and the wavepacket has dispersed significantly and panel (b) shows the maximum distance an electron can travel before complete dispersion. We can see that for higher magnetic fields and low energies, these times and distances are outside the realms of realistic experimental values, however as the magnetic field drops and the energy increases the time and distance reduce significantly such that the rate with the off-diagonal coherence terms need to be taken into account.

The next step for this analysis is to further develop equation Eq. (6.84), which gives the probability of the emission of a phonon, as opposed to the probability that a phonon is not emitted in equation Eq. (6.83). The first step in developing Eq. (6.84) is the same as for Eq. (6.83), i.e.

$$\langle k_4|[H_S, \rho^{(1)}(t)]|k_3\rangle = (E_{k_4} - E_{k_3})\ \langle k_4|\rho^{(1)}(t)|k_3\rangle \tag{6.113}$$

We also have the term $\langle k_2|\rho^{(0)}(t)|k_1\rangle$, which we have just calculated in Eq. (6.91), albeit with different wavenumbers. This shows that the equation with phonon emission occuring is some perturbation multiplied by the no-phonon case.

This is where we stop for this thesis, however, future research could develop this equation further, to investigate how it varies with $\kappa_{34} = k_4 - k_3$. If there is change in the motion of the wavepacket with increasing κ, then we can use the semiclassical case without issue, however, if over time this causes a great deal of spreading of the wavepacket, then we will see that the semiclassical model no longer accurately predicts to motion of an electron undergoing phonon emission.

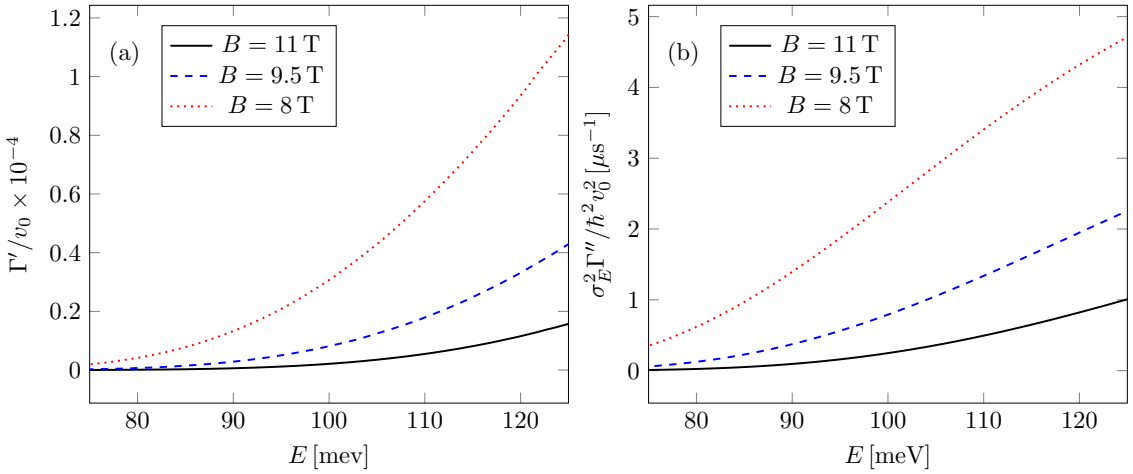

Figure 6.3: The terms Γ'/v_0 and $\sigma_E^2/(\hbar^2 v_0^2)\Gamma''$ from Eq. (6.111) are shown here. We can see from these plots that the values of these terms increase to the point that we are unable to ignore their effects, within the scope of the energy and magnetic field ranges that we consider in experiments. The parameters used for these plots are $\sigma_E = 1\,\mathrm{meV}$, y-confinement, $\hbar\omega_y = 2.7\,\mathrm{meV}$ and central energy $E_0 = 100\,\mathrm{meV}$.

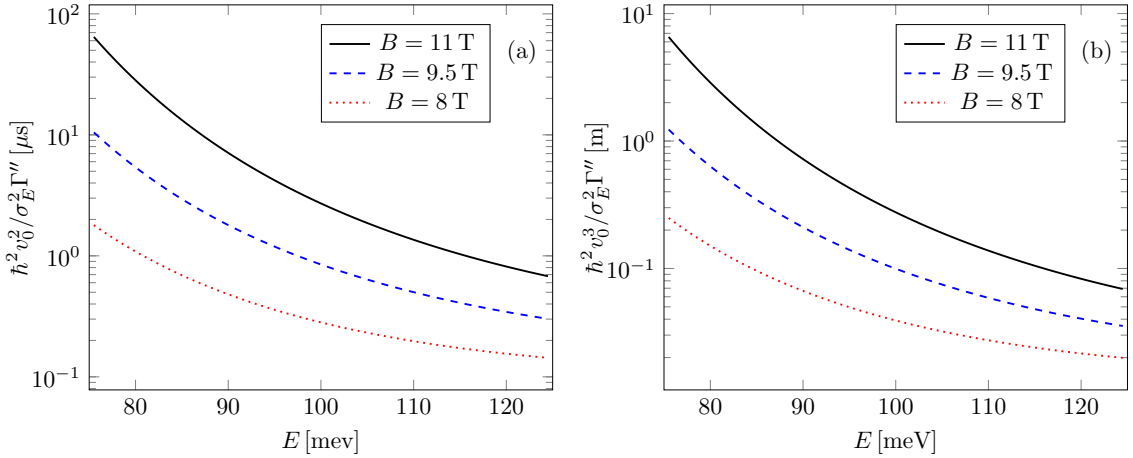

Figure 6.4: Panel (a) shows the mean time in microseconds until an electron undergoes significant decoherence for a range of energies and magnetic fields. Panel (b) shows the mean path length for the same values of energy and magnetic field. As magnetic field decreases, the life time and mean free path of the electron decreases significantly, such that the semiclassical view of the system is no longer a good approximation for the behaviour of an electron.

6.6 Chapter summary

In this chapter we have derived a master equation describing the emission rate of LO-phonons and the behaviour of electrons undergoing this emission. First, we derived an equation for the rate which takes into account the off-diagonal terms of the density matrix which describe the coherence of the electron whereas previous works [23] have treated only the diagonal elements. We show that for small differences in the starting state wavenumbers, (i.e. wavepacket widths) this diagonal only equation for the emission rate can be used as a good approximation to the full rates with the coherences, however as the wavepacket widths increase, the off diagonal terms

become increasingly important such that they can no longer be ignored.

We have then derived an equation of motion to describe the motion of electrons with these full equations for the emission rate included. We have concentrated here on the case where phonons are not emitted, and have found that including the full emission rates we see a moving wavepacket which also has a dissipation related to the diagonal rate, which validates the previous approach, but also dispersion over time related to the second derivative of the rate, which in the off diagonal case becomes important at energies and magnetic fields within the ranges that we consider here.

Part IV

Conclusions, outlook and appendices

Chapter 7

Conclusions and future work

THROUGHOUT this thesis, we have explored the world of hot-electron quantum-optics, and its uses in modern technology. The ability to use electrons with tunable energies opens up opportunities to perform experiments with these hot-electrons, which can mitigate the issues of electrons interacting with their surroundings. Raising the energy of these electrons is not without its issues however, and effects that are negligible for cold-electrons become more important at these higher energies.

7.1 Conclusions

In Part II, we considered an electronic MZI, which was attached to a quantum-dot-based SES. There is an uncertainty in the energy of electrons injected from these sources, which can lead to a change in the path followed by the electron. Given their dependence on the path lengths of the interferometer, the phases can be very much affected by this shift. When the electron wavepacket splits at the quantum point contact beamsplitters, the phase picked up may be random due to the uncertainty in the injected electron's energy, leading to interference. In extreme cases the electrons arrive at different times entirely. The interference leads to amplitude reduction, which in turn reduces the visibility of the system. In this thesis we have investigated the effect that these small uncertainties in energy have on the visibility.

We have found that for a given MZI build, the effect of this phase averaging can be removed entirely with correct choice of parameters. Specifically, we have found that unlike classical optics, where paths of equal length would give optimal interference, for an electron system there needs to be an offset to the path lengths l_{offset} in order to eradicate the effect of phase averaging. Typical sizes for the required offset for hot electrons is on the order of $1\,\mu$m in length, which is an unexpectedly large offset in comparison with predictions from previous works. This l_{offset} is then of vital importance to experiments and has a large effect on the visibility if ignored.

While the visibility can be maximised for any choice of magnetic field and energy, there is always the chance of experimental error. For higher energies and lower magnetic field the range of energies and offsets for which the visibility is maximised is broader, so there is more room for error. In Ref. [22] an MZI of similar path lengths was investigated and the same combination of magnetic field and energy was found to optimally reduce the effects of decoherence due to phonon scattering, with the caveat that this requires reduced signal strength due to filtering out the

LO-phonon replicas discussed in Chapter 5.

The results in this thesis are directly relevant to current experiments [37, 24]. In these experiments electrons are transported over paths of between 5 and 28 μm. With QPC beamsplitters already in use for time of flight experiments [37] all of the components to build a hot-electron MZI exist and building one is completely feasible in the near future. Due to the substantial offset length previously not accounted for the results from this thesis are crucial for the successful implementation of this type of experiment.

Moreover, previous works [56, 58, 60] have assumed that beamsplitters used in experiments reflect and transmit wavepackets at a 50 : 50 ratio, however we show in Chapter 3 that with the Fertig-Halperin saddle point model of the beamsplitters, there is an energy dependence on both the transmission and reflection coefficients, and the phase induced by the beamsplitters. Comparing the visibility when using the full energy dependent transmission and reflection coefficients with the visibility when they are assumed to be 50 : 50, we have found that the range at which the visibility is maximised is significantly over estimated depending on the energetic width of the beamsplitters, as shown in Fig. 3.9, thus highlighting the importance of these calculations. In Chapter 4 we investigated arrival time distributions of electrons taking into account the energy dependence on the beamsplitter phases and examined how this is affected by the energy uncertainty. We also introduced the concept of asymmetric beamsplitters, where each side of the beamsplitter is a different width. We again calculated the arrival time distributions and investigated how this asymmetry affects the arrival time of the electron, and the energy at which any interference takes place.

We have found that for wide beamsplitters, the energy profile has little effect on the transmission and reflection coefficients or the phase of the electron, as the electron only sees a small portion of it and therefore experiences only a tiny difference in potential across its width. This means that the central energy of the beamsplitter has no impact on where the interference will take place. For narrower beamsplitters however, the electron will experience different effects from the potential profile, such that the central position now predicts the energy at which the interference takes place. When looking at the visibility as calculated from these simulations, we see that the phase averaging contribution provides an envelope for the maximum visibilities possible as the central energy of the beamsplitter varies from the energy for which the path lengths have been optimised, E_{peak}. As visibility is maximised when the beamsplitters are 50 : 50, we have found that wider beamsplitters in comparison to the width of the wavepacket will yield a higher visibility of the system over a larger energy range.

Up until now, the beamsplitters have always been modelled as symmetric. We then introduced the concept of asymmetry, and investigate the effect that this has on ATDs of the electrons. We found that for small asymmetry there is a slight shift in the position at which the interference occurs, however when the asymmetry is larger the interference pattern itself is modified by the asymmetry of the beamsplitters. This is another example of how a thorough theoretical investigation can benefit experimental design. Asymmetry in the beamsplitters can shift the energy at which interference occurs, thereby changing the required offset length to maximise visibility, which we know from Chapter 3 is of vital importance in the building of hot-electron interferometers.

The combination of these effects with the results from Ref. [22] gives unprecedented insight into the successful design of electronic MZI experiments for future quantum technology applications.

The phase averaging affects investigated in Part II are not the only incoherent effect that we have considered. At the higher energies of the hot-electrons, the effect of LO-phonon emission becomes dominant, as there is now enough energy in the electrons (at least 36 meV is required in GaAs systems, while we consider electrons with energies around 100 meV and up) to emit LO-phonons, which we considered in Part III.

For this part we considered only electrons emitted from a single-electron source and then detected a short distance later, without attachment to a MZI. Previous theoretical models of the emission rates of LO-phonons and the behaviour of electrons undergoing this emission have been semiclassical. They assumed a narrow wavepacket such that there is no difference between either side of the wavepacket, k and k', meaning that only the diagonal elements of the density matrix describing the electron are included. To get a complete quantum picture of electron behaviour, these coherence terms must also be taken into account. To this end, we have derived the rates and master equation for a hot-electron, keeping the off diagonal rates in. We found that for small wavepackets, the diagonal-terms-only model in Ref. [23] is acceptable, however once the wavepackets are approximately 1 meV in width the off-diagonal terms become important. We also obtain an equation of motion to investigate the behaviour of an electron after a phonon has been emitted. This we have split into two parts, the first of which we investigated in this thesis, and the second of which we consider as part of the future work.

We have found that for the subensemble with no LO-phonon emission, additional terms for the dispersion and dissipation of an electron are introduced that depend on the rates which take into account the coherence terms of the density matrix. The contributions to the equation of motion of these terms were found to be small for high magnetic fields and lower energies, however decreasing the magnetic field down by as little as 3T increases dispersion significantly over the course of 1 μs, and over much shorter times for energies over 100 meV. Dissipation is also built into this model, and depends only on the central wave number k_0, and not the width, which is also predicted by the semiclassical model. Dispersion times on the order of 1 μs are insignificant on the scale of single-electron experiments, thereby justifying the use of the semiclassical model, at least in the case of the no-phonon ensemble, where we find that the wavepacket maintains complete quantum coherence over time. We have also found the maximum distance that an electron can travel before the dispersion due to phonons is significant, which for higher magnetic fields and low energies is much larger than typical experiments; however, as the magnetic field decreases and the energy increases these mean free paths decrease such that the coherence terms become important in modelling electrons.

7.2 Future work

While the findings in this thesis offer significant enhancements to future hot-electron physics, there is still much more to be explored.

The next stage for the investigation into LO-phonon emission will be to consider the second half of the equation of motion in Eq. (6.84), which gives the probabil-

ity that a phonon will be emitted. When we consider this second term, a loss of coherence of the electron due to phonon emission should appear as phonon replicas trailing behind the wavepackets, because after emission of a phonon these wavepackets have lower energy and therefore move with a lower velocity. This would be seen as phonon replicas trailing behind wavepackets such as those seen in Fig. 6.2. Investigating this term would lead to one of two conclusions: if the effect from this difference is minimal, we can conclude that the semiclassical description is appropriate in most cases for small electron widths, however if there is a large contribution from this term over time, the coherence terms become much more important in modelling single-electron systems.

The same model for the LO-phonons derived here could be applied with acoustic phonons [54]. This could then be further incorporated into the model of inter-arm coherence in an MZI studied in [22] for a complete quantum description of an electron travelling in an MZI. This complete picture of the electron behaviour in an MZI could then be combined with the complete microscopic model of the device itself described by the findings in Part II of this thesis.

Combining the results from Parts II and III gives further insight into how we can reduce the incoherent effects in hot-electron quantum-optics experiments. We have found that the optimal conditions for the different effects do not necessarily coincide with each other, such that some trade off between the effects must be made. These results can be used as inputs into future experimental design such that the results from any experiments performed in the same systems can be as clear as possible and any potential future uses for these experiments can be made a reality with fewer obstacles.

There is also currently ongoing work towards creating dynamic simulations of MZI experiments [89, 107, 108]. Our work could be used as an input to these simulations giving a more complete view of the action of the beamsplitters in these works, as they are currently based on a simplified model. We could also introduce the full description of the behaviour of electrons undergoing LO-phonon emission to these simulations to visualise this effect within an MZI.

There is also the potential for future investigations into the behaviour of electrons in an MZI when two single-electrons are injected, one from each potential source. This would require building in the Coulomb interaction and incorporating the phase averaging foundations for one electron experiments derived in this work. As well as increasing the number of electrons in these experiments, the MZI setups themselves could increase in complexity. Bigger networks of MZIs will show increasingly complex effects and open up the possibility of observing more signatures of quantum behaviour. The work in this thesis has laid the foundations of these calculations giving a starting point for modelling more complicated systems.

The findings in this thesis combine to give an overall view of two significant incoherent effects in hot-electron quantum optics: phase averaging and LO-phonon emission. Future experiments and dynamic simulations can use these results to optimise their outcomes.

Appendix A

Calculation of the Aharonov-Bohm phase

Consider the Mach-Zehnder Interferometer in Fig. A.1. We choose coordinate system and a Landau gauge such that the vector potential reads

$$\mathbf{A} = (-By, 0, 0). \tag{A.1}$$

The important thing to note is that for $y > 0$, $\mathbf{A}$ points in the $-x$ direction; for

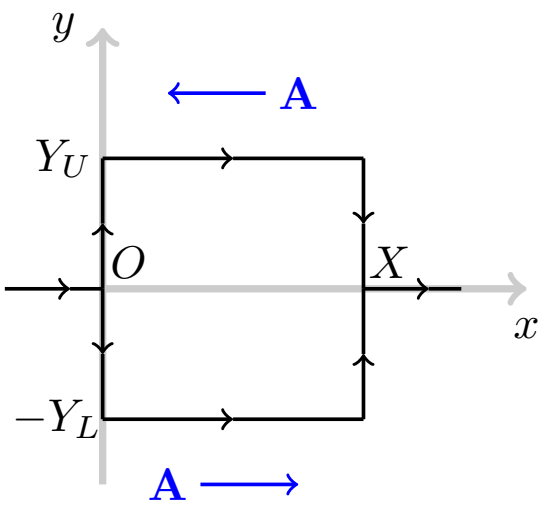

Figure A.1: Regular AB loop with coordinate system chosen for ease of use.

$y < 0$, it points in the opposite, $+x$ direction.

In general, the AB phase picked up along a path S is [34]

$$\phi_{\mathrm{AB}}^{(S)} = \frac{q}{\hbar} \oint_S \mathbf{A}.\,\mathrm{d}\mathbf{x}. \tag{A.2}$$

With the above gauge choice, the contributions on the vertical parts of the interferometer paths are exactly zero, leaving only contributions from the horizontal parts. Along the upper path for an electron ($q = -e$, with $e > 0$) we have

$$\phi_{\mathrm{AB}}^{(U)} = \frac{-e}{\hbar} \int_0^X (-BY_U)\,\mathrm{d}x = cBY_U X; \tag{A.3}$$

along the lower

$$\phi_{\mathrm{AB}}^{(L)} = \frac{-e}{\hbar}\int_0^X (-BY_L)\,\mathrm{d}x = -cBY_LX;. \tag{A.4}$$

These two have different signs due to the different direction of $\mathbf{A}$ along the two paths.

Taking into account only the AB phase, the wave function just before the second beamsplitter is

$$|\Psi\rangle = \frac{1}{\sqrt{2}}\left(e^{i\phi_{\mathrm{AB}}^{(U)}}\left|\Phi^{(U)}\right\rangle + e^{i\phi_{\mathrm{AB}}^{(L)}}\left|\Phi^{(L)}\right\rangle\right) \tag{A.5}$$

and therefore the interference term will be proportional to

$$\cos\left(\phi_{\mathrm{AB}}^{(U)} - \phi_{\mathrm{AB}}^{(L)}\right) \tag{A.6}$$

The total phase difference between upper and lower is thus

$$\phi_{\mathrm{AB}} = \phi_{\mathrm{AB}}^{(U)} - \phi_{\mathrm{AB}}^{(L)} = \frac{e}{\hbar}BY_UX + \frac{e}{\hbar}BY_LX = \frac{e}{\hbar}BX(Y_U + Y_L) = \frac{e}{\hbar}Ba \tag{A.7}$$

where a is the interferometer area (and $e > 0$).

Appendix B

Linearisation of dispersion relation

To calculate the energy with an additional small change in energy the guide centre was chosen to be $y = y_0 + \Delta y$, that is, the original guide centre of the black path in Fig. 3.3 plus a small change in the guide centre, Δy, which corresponds to the blue dashed path in Fig 3.3. Using this guide centre, Eq. (3.21) becomes,

$$E_0 + \Delta E = \epsilon_n + \hbar\Omega\left(n + \frac{1}{2}\right) + \frac{1}{2}m\omega_y^2\left(\frac{\Omega}{\omega_c}\right)^2 (y_0 + \Delta y)^2, \tag{B.1}$$

$$\begin{aligned} E_0 + \Delta E = \epsilon_n + \hbar\Omega\left(m + \frac{1}{2}\right) + \frac{1}{2}m\omega_y^2\left(\frac{\Omega}{\omega_c}\right)^2 y_0^2 \\ + m\omega_y^2\left(\frac{\Omega}{\omega_c}\right)^2 (y_0\Delta y) + \frac{1}{2}m\omega_y^2\left(\frac{\Omega}{\omega_c}\right)^2 \Delta y^2. \end{aligned} \tag{B.2}$$

The following is a justification for the linearisation to first order of this equation. In order to show this, the total phase, $\phi_{\text{tot}} = \phi_{\text{AB}} + \phi_{\text{dyn}}$ was calculated including the Δy^2 term and compared to the total phase without this term.

If, instead of linearising the dispersion relation to get Eq. (3.25), we keep the full equation, we can see that

$$\Delta E = m\omega_y^2\left(\frac{\Omega}{\omega_c}\right)^2 (y_0\Delta y) + \frac{1}{2}m\omega_y^2\left(\frac{\Omega}{\omega_c}\right)^2 \Delta y^2. \tag{B.3}$$

We need to solve this for Δy in order to use this as an input into our equations for ϕ_{AB} and ϕ_{dyn}.

$$m\omega_y^2\left(\frac{\Omega}{\omega_c}\right)^2 \Delta y^2 + 2m\omega_y^2\left(\frac{\Omega}{\omega_c}\right)^2 (y_0\Delta y) - 2\Delta E = 0 \tag{B.4}$$

Using the quadratic equation and simplifying gives

$$\Delta y = \pm\sqrt{y_0^2 + \frac{2\Delta E\omega_c^2}{\Omega^2 m\omega_y^2}} - y_0 \tag{B.5}$$

We can then substitute for y_0 in terms of k_0 and introduce the velocity v_0 to simplify further, which gives

$$\Delta y = \frac{\omega_c}{\omega_y}\left[-\frac{v_0}{\omega_y} \pm \sqrt{\frac{v^2}{\omega_y^2} + \frac{2\Delta E}{m\Omega^2}}\right], \tag{B.6}$$

and

$$\Delta y^2 = \left(\frac{\omega_c}{\omega_y}\right)^2 \left[\frac{2v^2}{\omega_y^2} + \frac{2\Delta E}{m\Omega^2} \mp \frac{2v}{\omega_y}\sqrt{\frac{v^2}{\omega_y^2} + \frac{2\Delta E}{m\Omega^2}}\right]. \tag{B.7}$$

These can now be used in Eq. (3.38) and Eq. (3.42) to give new equations for the two phases including the higher order term.

$$\phi_{\mathrm{AB}} = \frac{m_e^*\omega_c}{\hbar}\left\{A_0 + l_0\frac{\omega_c}{\omega_y}\left[-\frac{v_0}{\omega_y} \pm \sqrt{\frac{v_0^2}{\omega_y^2} + \frac{2\Delta E}{m_e^*\Omega^2}}\right] + 4\left(\frac{\omega_c}{\omega_y}\right)^2\left[\frac{2v_0^2}{\omega_y^2} + \frac{2\Delta E}{m_e^*\Omega^2} \mp \frac{2v_0}{\omega_y}\sqrt{\frac{v_0^2}{\omega_y^2} + \frac{2\Delta E}{m_e^*\Omega^2}}\right]\right\} \tag{B.8}$$

$$\phi_{\mathrm{dyn}} = \frac{2l_0E_0}{\hbar v_0} + \frac{16E_0}{\hbar v_0}\frac{\omega_c}{\omega_y}\left[-\frac{v_0}{\omega_y} \pm \sqrt{\frac{v_0^2}{\omega_y^2} + \frac{2\Delta E}{m_e^*\Omega^2}}\right] + \frac{l_0\Omega^2 m_e^*}{\hbar\omega_y}\left[-\frac{v_0}{\omega_y} \pm \sqrt{\frac{v_0^2}{\omega_y^2} + \frac{2\Delta E}{m_e^*\Omega^2}}\right] + \frac{8m_e^*\omega_c}{\hbar}\left(\frac{\Omega}{\omega_y}\right)^2\left[\frac{2v_0^2}{\omega_y^2} + \frac{2\Delta E}{m_e^*\Omega^2} \mp \frac{2v_0}{\omega_y}\sqrt{\frac{v_0^2}{\omega_y^2} + \frac{2\Delta E}{m_e^*\Omega^2}}\right]. \tag{B.9}$$

Whether to choose the positive or negative form of the quadratic is decided by looking at the coefficient a_0. As this coefficient depends only on the original equation for E_0, it should remain unchanged. The positive sign of the quadratic gives this result, so this is the one we choose. It corresponds to an electron travelling along the edges defined in Fig. 3.3, whereas the negative sign corresponds to an electron travelling along the opposite edge. This gives an equation of ϕ_{tot} of

$$\begin{aligned}\phi_{\mathrm{tot}} = {} & \frac{m_e^*\omega_c}{\hbar}\left\{A_0 + l_0\frac{\omega_c}{\omega_y}\left[-\frac{v_0}{\omega_y} + \sqrt{\frac{v_0^2}{\omega_y^2} + \frac{2\Delta E}{m_e^*\Omega^2}}\right] + 4\left(\frac{\omega_c}{\omega_y}\right)^2\left[\frac{2v_0^2}{\omega_y^2} + \frac{2\Delta E}{m_e^*\Omega^2} - \frac{2v_0}{\omega_y}\sqrt{\frac{v_0^2}{\omega_y^2} + \frac{2\Delta E}{m_e^*\Omega^2}}\right]\right\} + \frac{2l_0E_0}{\hbar v_0} \\ & + \frac{16E_0}{\hbar v_0}\frac{\omega_c}{\omega_y}\left[-\frac{v_0}{\omega_y} + \sqrt{\frac{v_0^2}{\omega_y^2} + \frac{2\Delta E}{m_e^*\Omega^2}}\right] + \frac{l_0\Omega^2 m_e^*}{\hbar\omega_y}\left[-\frac{v_0}{\omega_y} + \sqrt{\frac{v_0^2}{\omega_y^2} + \frac{2\Delta E}{m_e^*\Omega^2}}\right] \\ & + \frac{8m_e^*\omega_c}{\hbar}\left(\frac{\Omega}{\omega_y}\right)^2\left[\frac{2v_0^2}{\omega_y^2} + \frac{2\Delta E}{m_e^*\Omega^2} - \frac{2v_0}{\omega_y}\sqrt{\frac{v_0^2}{\omega_y^2} + \frac{2\Delta E}{m_e^*\Omega^2}}\right].\end{aligned} \tag{B.10}$$

Previously we have split ϕ_{tot} into three terms based on their dependencies on ΔE, and then named the coefficents of ΔE^2 and ΔE, a_2 and a_1 respectively, and terms with no dependence on the change in energy were grouped into a term called a_0.

It is necessary to find these coefficients for our new equation of ϕ_{tot}. We must perform Taylor series expansions on the square root terms in order to write them in the same way as before.

$$\left[1 + \frac{2\Delta E}{m_e^* v_0^2}\left(\frac{\omega_y}{\Omega}\right)^2\right]^{1/2} = 1 + \frac{\Delta E}{m_e^* v_0^2}\left(\frac{\omega_y}{\Omega}\right)^2 - \frac{\Delta E^2}{2m_e^{*2}v_0^4}\left(\frac{\omega_y}{\Omega}\right)^4 \tag{B.11}$$

Substituting Eq. (B.11) into Eq. (B.10) gives

$$\phi_{\text{tot}} = \frac{2l_0E_0}{\hbar v_0} + \frac{m_e^*\omega_c}{\hbar}A_0 + \left(\frac{16E_0}{\hbar\omega_c m_e^* v_0^2}\frac{\omega_c^2}{\Omega^2} + \frac{l_0}{\hbar v_0} + \frac{\omega_c^2}{\Omega^2}\frac{l_0}{\hbar v_0}\right)\Delta E + \left(\frac{8}{\hbar\omega_c m_e^* v_0^2}\frac{\omega_c^2}{\Omega^2} + \frac{4}{\hbar\omega_c m_e^* v_0^2}\frac{\omega_c^4}{\Omega^4} - l_0\frac{1}{2\hbar m_e^* v_0^3}\frac{\omega_y^2\omega_c^2}{\Omega^4} - \frac{8E_0}{\hbar\omega_c}\frac{1}{m_e^{*2}v_0^4}\frac{\omega_y^2\omega_c^2}{\Omega^4} - \frac{l_0}{2m_e^*\hbar v_0^3}\frac{\omega_y^2}{\Omega^2}\right)\Delta E^2 \quad \text{(B.12)}$$

The coefficients a_2^{new}, a_1^{new} and a_0^{new} are therefore

$$a_2^{new} = \frac{4}{\hbar\omega_c m_e^* v_0^2}\frac{\omega_c^2}{\Omega^2}\left[2 + \frac{\omega_c^2}{\Omega^2}\right] - \frac{l_0}{2\hbar m_e^* v_0^3}\frac{\omega_y^2}{\Omega^2}\left[1 + \frac{\omega_c^2}{\Omega^2}\right] - \frac{8E_0}{\hbar\omega_c m_e^{*2} v_0^4}\frac{\omega_y^2\omega_c^2}{\Omega^4} \quad \text{(B.13)}$$

$$a_1^{new} = \frac{16E_0}{\hbar\omega_c m_e^* v_0^2}\frac{\omega_c^2}{\Omega^2} + \frac{l_0}{\hbar v_0} + \frac{\omega_c^2}{\Omega^2}\frac{l_0}{\hbar v_0} \quad \text{(B.14)}$$

$$a_0^{new} = \frac{2l_0E_0}{\hbar v_0} + \frac{m_e^*\omega_c}{\hbar}A_0 \quad \text{(B.15)}$$

If we compare Eqs. (B.13), (B.14) and (B.15) with Eq. (3.45a), (3.45b) and (3.45c) respectively we see that the only equation which has changed is a_2^{new}(Eq. (B.13)) from a_2 (Eq. (3.45a)).

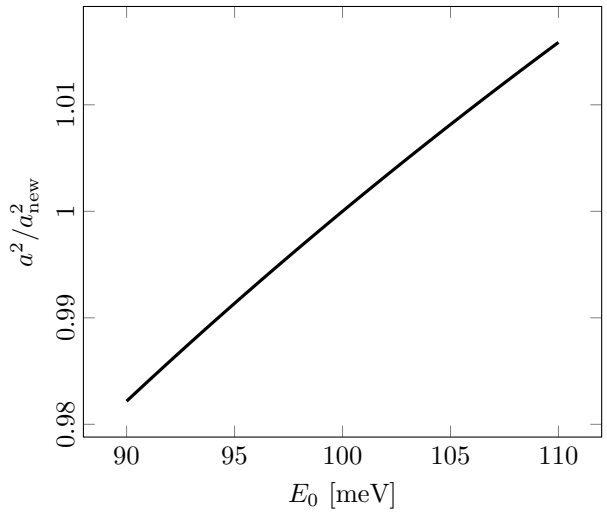

Figure B.1: The ratio of the total phase with and without the Δy^2 is always within a few percent of 1 for the energies that we are interested in. We can therefore say that the exclusion of the Δy^2 term does not affect the outcome significantly.

To confirm whether or not we can disregard the Δy^2 dependent term in Eq. (B.2) we can look at the the ratio of a_2/a_2^{new}. If this is ≈ 1 we can say the two coefficients are the same, and therefore the inclusion of the Δy^2 term does not have a significant contribution. Figure B.1 shows this ratio of a_2/a_2^{new}. It is ~ 1, so we can say that the two coefficients are approximately equal. Considering this result, we can confirm that the linearisation to first order of Eq. (B.2) is an acceptable approximation.

Appendix C

Calculating additional phase shift

The extra phase shift from Section 3.6.3 is found by rearranging the terms containing F in Eq. (3.50), and looking at the real and imaginary parts separately,

$$\begin{aligned}\sqrt{1+F^2} =&(1-iF)(\cos(2\theta)+i\sin(2\theta)) \\ &=\cos(2\theta)+F\sin(2\theta)+i(\sin(2\theta)-F\cos()2\theta)).\end{aligned} \tag{C.1}$$

The imaginary part gives,

$$\begin{aligned}\sin(2\theta)-F\cos(2\theta)&=0 \\ \Rightarrow\tan 2\theta&=F\end{aligned} \tag{C.2}$$

and if we look at the real part we have

$$\sqrt{1+F^2}=\cos(2\theta)+F\sin(2\theta). \tag{C.3}$$

We can use the fact that $\sin(2\theta)=F\cos(2\theta)$ from the imaginary part, to give

$$\begin{aligned}\sqrt{1+F^2}&=\cos(2\theta)+F^2\cos(2\theta) \\ \Rightarrow&\frac{1}{\sqrt{1+F^2}}=\cos(2\theta) \\ \Rightarrow&\sin^2(2\theta)+\cos^2(2\theta)=(1+F^2)\cos^2(2\theta) \\ \Rightarrow&\tan(2\theta)=F.\end{aligned} \tag{C.4}$$

Both parts of the equation have given us the same value of θ of

$$\theta=\frac{1}{2}\arctan(F). \tag{C.5}$$

This phase shift can be absorbed into the E-independent part of the phase in the equation for current, as it is just a shift.

References

[1] B. Pullman and A.R. Reisinger. *The atom in the history of human thought*. Oxford University Press, 2001.

[2] J. Al-Khalili. The birth of the electric machines: a commentary on faraday (1832) 'experimental researches in electricity'. *Philos. Trans. Royal Soc. A*, 373(2039):20140208, 2015.

[3] G. E. Moore. Cramming more components onto integrated circuits, 1965.

[4] G. Fève, A. Mahé, J.-M. Berroir, T. Kontos, B. Plaçais, D. C. Glattli, A. Cavanna, B. Etienne, and Y. Jin. An on-demand coherent single-electron source. *Science*, 316(5828):1169–1172, 2007.

[5] W. P. Schleich *et al.* Quantum technology: from research to application. *Appl. Phys. B: Lasers Opt.*, 122(5), 2016.

[6] S. P. Giblin, M. Kataoka, J. D. Fletcher, P. See, Janssen T. J. B. M., J. P. Griffiths, G. A. C. Jones, I. Farrer, and D. A. Ritchie. Towards a quantum representation of the ampere using single electron pumps. *Nat. Commun.*, 3, 2012.

[7] Bureau International des Poids et Mesures. The international system of units (si): Unit definitions, 2018.

[8] M. D. Eisaman, J. Fan, A. Migdall, and S. V. Polyakov. Invited review article: Single-photon sources and detectors. *Rev. Sci. Instrum.*, 82(7):071101, 2011.

[9] P. Senellart, G. Solomon, and A. White. High-performance semiconductor quantum-dot single-photon sources. *Nat. Nanotechnol.*, 12(11):1026–1039, 2017.

[10] Y. Zhao, B. Qi, X. Ma, H.-K. Lo, and L. Qian. Experimental quantum key distribution with decoy states. *Phys. Rev. Lett.*, 96:070502, 2006.

[11] J. Gabelli. Violation of kirchhoff's laws for a coherent RC circuit. *Science*, 313(5786):499–502, 2006.

[12] J. P. Pekola, O-P. Saira, V. F. Maisi, A. Kemppinen, M. Möttönen, Y. A. Pashkin, and D. V. Averin. Single-electron current sources: Toward a refined definition of the ampere. *Rev. Mod. Phys.*, 85:1421–1472, 2013.

[13] M. A. Kastner. The single-electron transistor. *Rev. Mod. Phys.*, 64:849–858, 1992.

[14] L. Fricke, M. Wulf, B. Kaestner, F. Hohls, P. Mirovsky, B. Mackrodt, R. Dolata, T. Weimann, K. Pierz, U. Siegner, and H. W. Schumacher. Self-referenced single-electron quantized current source. *Phys. Rev. Lett.*, 112:226803, 2014.

[15] L. J. Geerligs, V. F. Anderegg, P. A. M. Holweg, J. E. Mooij, H. Pothier, D. Esteve, C. Urbina, and M. H. Devoret. Frequency-locked turnstile device for single electrons. *Phys. Rev. Lett.*, 64:2691–2694, 1990.

[16] L. P. Kouwenhoven, A. T. Johnson, N. C. van der Vaart, A. van der Enden, C. J. P. M. Harmans, and C. T. Foxon. Quantized current in a quantum dot turnstile. *Z. Phys., B Condens. matter*, 85(3):381–388, 1991.

[17] Y. Nagamune, H. Sakaki, L. P. Kouwenhoven, L. C. Mur, C. J. P. M. Harmans, J. Motohisa, and H. Noge. Single electron transport and current quantization in a novel quantum dot structure. *Appl. Phys. Lett.*, 64(18):2379–2381, 1994.

[18] Y. Ono and Y. Takahashi. Electron pump by a combined single-electron/field-effect- transistor structure. *Appl. Phys. Lett.*, 82(8):1221–1223, 2003.

[19] B. Kaestner and V. Kashcheyevs. Non-adiabatic quantized charge pumping with tunable-barrier quantum dots: a review of current progress. *Rep. Prog. Phys.*, 78(10):103901, 2015.

[20] A. Fujiwara, K. Nishiguchi, and Y. Ono. Nanoampere charge pump by single-electron ratchet using silicon nanowire metal-oxide-semiconductor field-effect transistor. *Appl. Phys. Lett.*, 92(4):042102, 2008.

[21] B. Kaestner, V. Kashcheyevs, S. Amakawa, M. D. Blumenthal, L. Li, T. J. B. M. Janssen, G. Hein, K. Pierz, T. Weimann, U. Siegner, and H. W. Schumacher. Single-parameter nonadiabatic quantized charge pumping. *Phys. Rev. B*, 77:153301, 2008.

[22] L. A. Clark, M. Kataoka, and C. Emary. Mitigating decoherence in hot electron interferometry. *New J. Phys.*, 22(10):103031, 2020.

[23] C. Emary, A. Dyson, Sungguen Ryu, H.-S. Sim, and M. Kataoka. Phonon emission and arrival times of electrons from a single-electron source. *Phys. Rev. B*, 93:035436, 2016.

[24] N. Johnson, C. Emary, S. Ryu, H.-S. Sim, P. See, J. D. Fletcher, J. P. Griffiths, G. A. C. Jones, I. Farrer, D. A. Ritchie, M. Pepper, T. J. B. M. Janssen, and M. Kataoka. Lo-phonon emission rate of hot electrons from an on-demand single-electron source in a GaAs/AlGaAs heterostructure. *Phys. Rev. Lett.*, 121:137703, 2018.

[25] T. Ota, S. Akiyama, M. Hashisaka, K. Muraki, and T. Fujisawa. Spectroscopic study on hot-electron transport in a quantum hall edge channel. *Phys. Rev. B*, 99:085310, 2019.

[26] H. Zbinden, J. D. Gautier, N. Gisin, B. Huttner, A. Mueller, and W. Tittel. Interferometry with faraday mirrors for quantum cryptography. *Electron. Lett.*, 33:586 – 588, 1997.

[27] R. Gelles and T. Mor. *On the security of interferometric quantum key distribution.* Springer Berlin Heidelberg, 2012.

[28] J. P. Dowling and K. P. Seshadreesan. Quantum optical technologies for metrology, sensing, and imaging. *J. Light. Technol.*, 33(12):2359–2370, 2015.

[29] A. A. Michelson and E. W. Morley. On the relative motion of the earth and the luminiferous ether. *Am. J. Sci. (1880)*, s3-34(203):333–345, 1887.

[30] B. P. Abbott *et al.* Observation of gravitational waves from a binary black hole merger. *Phys. Rev. Lett.*, 116(6):061102, 2016.

[31] R. Ladenburg, J. Winckler, and C. C. Van Voorhis. Interferometric studies of faster than sound phenomena. part i. the gas flow around various objects in a free, homogeneous, supersonic air stream. *Phys. Rev.*, 73(11):1359–1377, 1948.

[32] Y. Yamamoto. Optically controlled semiconductor spin qubits and indistinguishable single photons for quantum information processing. In P. Bhattacharya, R. Fornari, and H. Kamimura, editors, *Semicond. Sci. Technol.*, pages 400 – 431. Elsevier, Amsterdam, 2011.

[33] Y. Ji, Y. Chung, M. Sprinzak, D. Heiblum, D. Mahalu, and H. Shtrikman. An electronic mach-zehnder interferometer. *Nature*, 422:415–418, 2003.

[34] Y. Aharonov and D. Bohm. Significance of electromagnetic potentials in the quantum theory. *Phys. Rev.*, 115:485–491, 1959.

[35] M. Alietti, C. Canali, A. Castaldini, A. Cavallini, A. Cetronio, C. Chiossi, S. D'Auria, C. del Papa, C. Lanzieri, F. Nava, and P. Vanni. Performance of a new ohmic contact for GaAs particle detectors. *Nucl. Instrum. Methods. Phys. Res. B*, 362(2):344–348, 1995.

[36] H. M. Wiseman and G. J. Milburn. *Quantum measurement and control.* Cambridge University Press, 2010.

[37] M. Kataoka, N. Johnson, C. Emary, P. See, J. P. Griffiths, G. A. C. Jones, I. Farrer, D. A. Ritchie, M. Pepper, and T. J. B. M. Janssen. Time-of-flight measurements of single-electron wave packets in quantum hall edge states. *Phys. Rev. Lett.*, 116:126803, 2016.

[38] S. Ryu, M. Kataoka, and H.-S. Sim. Ultrafast emission and detection of a single-electron gaussian wave packet: A theoretical study. *Phys. Rev. Lett.*, 117:146802, 2016.

[39] C. J. Barratt, S. Ryu, A. Clark, L, H.-S. Sim, M. Kataoka, and C. Emary. Asymmetric arms maximize visibility in hot-electron interferometers. *Phys. Rev. B*, 104:035436, 2021.

[40] S. Datta. *Electronic transport in mesoscopic systems.* Cambridge studies in semiconductor physics and microelectronic engineering 3. Cambridge University Press, Cambridge, 1997.

[41] L. de Broglie. Xxxv. a tentative theory of light quanta. *Lond. Edinb. Dubl. Phil. Mag.*, 47(278):446–458, 1924.

[42] T. Mimura. The early history of the high electron mobility transistor (hemt). *IEEE Trans. Microw. Theory Tech.*, 50(3):780–782, 2002.

[43] W. T. Sommer. Liquid helium as a barrier to electrons. *Phys. Rev. Lett.*, 12:271–273, 1964.

[44] C. Berger, Z. Song, T. Li, X. Li, A. Y. Ogbazghi, R. Feng, Z. Dai, A. N. Marchenkov, E. H. Conrad, P. N. First, and W. A. de Heer. Ultrathin epitaxial graphite: 2d electron gas properties and a route toward graphene-based nanoelectronics. *J. Phys. Chem. B*, 108(52):19912–19916, 2004.

[45] T. Schäpers. Fabrication of superconductor/two-dimensional-electron-gas structures. In *Springer Tracts in Modern Physics*, pages 21–30. Springer Berlin Heidelberg, 2001.

[46] K. v. Klitzing, G. Dorda, and M. Pepper. New method for high-accuracy determination of the fine-structure constant based on quantized hall resistance. *Phys. Rev. Lett.*, 45:494–497, 1980.

[47] D. C. Tsui, H. L. Stormer, and A. C. Gossard. Two-dimensional magnetotransport in the extreme quantum limit. *Phys. Rev. Lett.*, 48:1559–1562, 1982.

[48] R. B. Laughlin. Anomalous quantum hall effect: An incompressible quantum fluid with fractionally charged excitations. *Phys. Rev. Lett.*, 50:1395–1398, 1983.

[49] K. v. Klitzing, T. Chakraborty, P. Kim, V. Madhavan, X. Dai, J. McIver, Y. Tokura, L. Savary, D. Smirnova, A. M. Rey, C. Felser, J. Gooth, and X. Qi. 40 years of the quantum hall effect. *Nat. Rev. Phys.*, 2(8):397–401, 2020.

[50] B. Jeckelmann and B. Jeanneret. The quantum hall effect as an electrical resistance standard. *Rep. Prog. Phys.*, 64(12):1603–1655, 2001.

[51] R. G. Chambers. Shift of an electron interference pattern by enclosed magnetic flux. *Phys. Rev. Lett.*, 5:3–5, 1960.

[52] A. Tonomura, N. Osakabe, T. Matsuda, T. Kawasaki, J. Endo, S. Yano, and H. Yamada. Evidence for aharonov-bohm effect with magnetic field completely shielded from electron wave. *Phys. Rev. Lett.*, 56:792–795, 1986.

[53] T. Ando, A. B. Fowler, and F. Stern. Electronic properties of two-dimensional systems. *Rev. Mod. Phys.*, 54:437–672, 1982.

[54] C. Emary, L. A. Clark, M. Kataoka, and N. Johnson. Energy relaxation in hot electron quantum optics via acoustic and optical phonon emission. *Phys. Rev. B*, 99:045306, 2019.

[55] I. Neder, M. Heiblum, Y. Levinson, D. Mahalu, and V. Umansky. Unexpected behavior in a two-path electron interferometer. *Phys. Rev. Lett.*, 96:016804, 2006.

[56] L. V. Litvin, H.-P. Tranitz, W. Wegscheider, and C. Strunk. Decoherence and single electron charging in an electronic mach-zehnder interferometer. *Phys. Rev. B*, 75:033315, 2007.

[57] V. S.-W. Chung, P. Samuelsson, and M. Büttiker. Visibility of current and shot noise in electrical mach-zehnder and hanbury brown twiss interferometers. *Phys. Rev. B*, 72:125320, 2005.

[58] P. Roulleau, F. Portier, D. C. Glattli, P. Roche, A. Cavanna, G. Faini, U. Gennser, and D. Mailly. Finite bias visibility of the electronic mach-zehnder interferometer. *Phys. Rev. B*, 76:161309, 2007.

[59] P. Roulleau, F. Portier, P. Roche, A. Cavanna, G. Faini, U. Gennser, and D. Mailly. Direct measurement of the coherence length of edge states in the integer quantum hall regime. *Phys. Rev. Lett.*, 100:126802, 2008.

[60] P. Roulleau, F. Portier, P. Roche, A. Cavanna, G. Faini, U. Gennser, and D. Mailly. Noise dephasing in edge states of the integer quantum hall regime. *Phys. Rev. Lett.*, 101:186803, 2008.

[61] N. B. Zhitenev, R. J. Haug, K. v. Klitzing, and K. Eberl. Time-resolved measurements of transport in edge channels. *Phys. Rev. Lett.*, 71:2292–2295, 1993.

[62] P. Roulleau, F. Portier, P. Roche, A. Cavanna, G. Faini, U. Gennser, and D. Mailly. Tuning decoherence with a voltage probe. *Phys. Rev. Lett.*, 102:236802, 2009.

[63] E. Bieri, M. Weiss, O. Göktas, M. Hauser, C. Schönenberger, and S. Oberholzer. Finite-bias visibility dependence in an electronic mach-zehnder interferometer. *Phys. Rev. B*, 79:245324, 2009.

[64] S. Tewari, P. Roulleau, C. Grenier, F. Portier, A. Cavanna, U. Gennser, D. Mailly, and P. Roche. Robust quantum coherence above the fermi sea. *Phys. Rev. B*, 93:035420, 2016.

[65] F. Marquardt and C. Bruder. Effects of dephasing on shot noise in an electronic mach-zehnder interferometer. *Phys. Rev. B*, 70:125305, 2004.

[66] Géraldine Haack, Michael Moskalets, Janine Splettstoesser, and Markus Büttiker. Coherence of single-electron sources from mach-zehnder interferometry. *Phys. Rev. B*, 84:081303, 2011.

[67] C. Neuenhahn and F. Marquardt. Dephasing by electron–electron interactions in a ballistic mach–zehnder interferometer. *New J. Phys.*, 10(11):115018, 2008.

[68] I. Neder and E. Ginossar. Behavior of electronic interferometers in the nonlinear regime. *Phys. Rev. Lett.*, 100:196806, 2008.

[69] I. P. Levkivskyi and E. V. Sukhorukov. Dephasing in the electronic mach-zehnder interferometer at filling factor $\nu = 2$. *Phys. Rev. B*, 78:045322, 2008.

[70] M. D. Blumenthal, B. Kaestner, L. Li, S. Giblin, T. J. B. M. Janssen, M. Pepper, D. Anderson, G. Jones, and D. A. Ritchie. Gigahertz quantized charge pumping. *Nat. Phys.*, 3, 2007.

[71] C. Leicht, P. Mirovsky, B. Kaestner, F. Hohls, V. Kashcheyevs, E. V. Kurganova, U. Zeitler, T. Weimann, K. Pierz, and H. W. Schumacher. Generation of energy selective excitations in quantum hall edge states. *Semicond. Sci. Technol.*, 26(5):055010, 2011.

[72] M. Kataoka, J. D. Fletcher, P. See, S. P. Giblin, T. J. B. M. Janssen, J. P. Griffiths, G. A. C. Jones, I. Farrer, and D. A. Ritchie. Tunable nonadiabatic excitation in a single-electron quantum dot. *Phys. Rev. Lett.*, 106:126801, 2011.

[73] J. D. Fletcher, M. Kataoka, S. P. Giblin, Sunghun Park, H.-S. Sim, P. See, D. A. Ritchie, J. P. Griffiths, G. A. C. Jones, H. E. Beere, and T. J. B. M. Janssen. Stabilization of single-electron pumps by high magnetic fields. *Phys. Rev. B*, 86:155311, 2012.

[74] J. D. Fletcher, P. See, H. Howe, M. Pepper, S. P. Giblin, J. P. Griffiths, G. A. C. Jones, I. Farrer, D. A. Ritchie, T. J. B. M. Janssen, and M. Kataoka. Clock-controlled emission of single-electron wave packets in a solid-state circuit. *Phys. Rev. Lett.*, 111:216807, 2013.

[75] J. Waldie, P. See, V. Kashcheyevs, J. P. Griffiths, I. Farrer, G. A. C. Jones, D. A. Ritchie, T. J. B. M. Janssen, and M. Kataoka. Measurement and control of electron wave packets from a single-electron source. *Phys. Rev. B*, 92:125305, 2015.

[76] S. P. Giblin, M-H. Bae, N. Kim, Y-H. Ahn, and M. Kataoka. Robust operation of a GaAs tunable barrier electron pump. *Metrologia*, 54(3):299–306, 2017.

[77] M. Büttiker and R. Landauer. Traversal time for tunneling. *Phys. Rev. Lett.*, 49:1739–1742, 1982.

[78] R. Landauer and Th. Martin. Barrier interaction time in tunneling. *Rev. Mod. Phys.*, 66:217–228, 1994.

[79] L. Mandelstam and I. Tamm. The uncertainty relation between energy and time in non-relativistic quantum mechanics. *J. Phys. USSR*, 9:249–254, 1945.

[80] L. Mandelstam and I. Tamm. The uncertainty relation between energy and time in non-relativistic quantum mechanics. In *Selected Papers*, pages 115–123. Springer Berlin Heidelberg, 1991.

[81] S. Das Sarma and J. J. Quinn. Collective excitations in semiconductor superlattices. *Phys. Rev. B*, 25:7603–7618, 1982.

[82] W. Gasser and U.C. Täuber. Collective excitations of a layered electron gas in a strong magnetic field. *Z. Physik B - Condensed Matter*, 69:87–96, 1987.

[83] B. Y. Hu and S. Das Sarma. Many-body exchange-correlation effects in the lowest subband of semiconductor quantum wires. *Phys. Rev. B*, 48:5469–5504, 1993.

[84] G. Giuliani and G. Vignale. *Quantum theory of the electron liquid*. Cambridge University Press, Cambridge, UK ; New York, 2005.

[85] Ya.M. Blanter and M. Büttiker. Shot noise in mesoscopic conductors. *Phys. Rep.*, 336(1–2):1–166, 2000.

[86] H. A. Fertig and B. I. Halperin. Transmission coefficient of an electron through a saddle-point potential in a magnetic field. *Phys. Rev. B*, 36:7969–7976, 1987.

[87] J. J. Moré and D. C. Sorensen. Computing a trust region step. *SIAM J. Sci. Comput.*, 4(3):553–572, 1983.

[88] E. Weisz, H. K. Choi, I. Sivan, M. Heiblum, Y. Gefen, D. Mahalu, and V. Umansky. An electronic quantum eraser. *Science*, 344(6190):1363–1366, 2014.

[89] A. Beggi, P. Bordone, Buscemi F., and A. Bertoni. Time-dependent simulation and analytical modelling of electronic mach–zehnder interferometry with edge-states wave packets. *J. Phys.: Condens. Matter*, 27(47):475301, 2015.

[90] G. N. Lewis. The conservation of photons. *Nature*, 118(2981):874–875, 1926.

[91] M. Cardona. Phonons: The second type of quantum excitations discovered. *Ann. Phys. (Berl.)*, 9(11-12):865–870, 2000.

[92] D. Taubert, C. Tomaras, G. J. Schinner, H. P. Tranitz, W. Wegscheider, S. Kehrein, and S. Ludwig. Relaxation of hot electrons in a degenerate two-dimensional electron system: Transition to one-dimensional scattering. *Phys. Rev. B*, 83:235404, 2011.

[93] H. Fröhlich. Electrons in lattice fields. *Adv. Phys.*, 3(11):325–361, 1954.

[94] G. D. Mahan. *Many-particle physics*. Springer US, 3 edition, 2000.

[95] E. Pavarini, E. Koch, R. Scalettar, and R. Martin, editors. *The physics of correlated insulators, metals, and superconductors*, volume 7 of *Schriften des Forschungszentrums Jülich. Reihe Modeling and Simulation*. Forschungszentrum Jülich GmbH Zentralbibliothek, Verlag, Jülich, 2017.

[96] L.J. Sham and J.M. Ziman. *The electron-phonon interaction*, volume 15 of *Solid State Physics*. Academic Press, 1963.

[97] S. K. Sinha. Electron-phonon interaction and phonon dispersion relations using the augmented-plane-wave method. *Phys. Rev.*, 169:477–495, 1968.

[98] T. Brandes. Lectures on background to quantum infromation: Quantum dissipation, 2004.

[99] C. A. Brasil, F. F. Fanchini, and R. d. J. Napolitano. A simple derivation of the Lindblad equation. *Rev. Bras. de Ensino de Fis.*, 35:01 – 09, 2013.

[100] P. A. M. Dirac. The quantum theory of the emission and absorption of radiation. *Proc. R. Soc. Lond. A*, 114(767):243–265, 1927.

[101] A. Bhuiyan and F. Marsiglio. Landau levels, edge states, and gauge choice in 2d quantum dots. *Am. J. Phys.*, 88(11):986–1005, 2020.

[102] N. Johnson, J. D. Fletcher, D. A. Humphreys, P. See, J. P. Griffiths, G. A. C. Jones, I. Farrer, D. A. Ritchie, M. Pepper, T. J. B. M. Janssen, and M. Kataoka. Ultrafast voltage sampling using single-electron wavepackets. *Appl. Phys. Lett.*, 110(10):102105, 2017.

[103] H. T. Duc, Q. T. Vu, T. Meier, H. Haug, and S. W. Koch. Temporal decay of coherently optically injected charge and spin currents due to carrier–lo-phonon and carrier-carrier scattering. *Phys. Rev. B*, 74:165328, 2006.

[104] F. Vallée. Time-resolved investigation of coherent lo-phonon relaxation in iii-v semiconductors. *Phys. Rev. B*, 49:2460–2468, 1994.

[105] R Okuyama, M Eto, and T Brandes. Lasing and antibunching of optical phonons in semiconductor double quantum dots. *New J. Phys.*, 15(8):083032, 2013.

[106] H.-P. Breuer and F. Petruccione. *The theory of open quantum systems*. Oxford University Press, 2002.

[107] J. H. Davies. Electronic states in narrow semiconducting wires near threshold. *Semicond. Sci. Technol.*, 3(10):995–1009, 1988.

[108] J. H. Davies, Larkin. I. A., and E. V. Sukhorukov. Modeling the patterned two-dimensional electron gas: Electrostatics. *J. of Appl. Phys.*, 77(9):4504–4512, 1995.